Passive Q-switching of 1 micron Nd:YAG lasers for military target designator applications

Marc Walker Smillie

A thesis submitted for the degree of Doctor of Engineering

Industrial Doctorate Centre in Optics and Photonics

Department of Physics

University of Strathclyde

2018

Marc Walker Smillie

May 2018

Acknowledgements

I would like to begin by gratefully acknowledging EPSRC who funded this work.

The first person I would like to thank is my industrial supervisor Mark Silver for his guidance, patience and encouragement throughout the project. My time at Thales would have been considerably more difficult without him. Secondly, I thank my academic supervisor Alan Kemp for his continued support throughout the process. Only with the help of both supervisors have I achieved my goal of becoming a competent researcher.

I would also like to thank everyone at Thales Glasgow who have supported my research, particularly Stephen Lee who I have always considered as my third (if unofficial) supervisor. A special thanks goes to Adam Sroka, whose Matlab tutoring has helped me on countless occasions.

In addition I would like to thank the University of Strathclyde for managing my studentship, with a particular thanks to Lorraine and Sharon who looked after me during my time at the Institute of Photonics.

Without the Industrial Doctorate Centre at Heriot-Watt University there would be no EngD, so I give thanks for the opportunities that have been extended to me as a result of their hard work. With this I give a special thanks to the head of the IDC Derryck Reid, and the IDC administrators Linda Bruce and Alison Low for keeping me on track throughout the process.

Importantly, I would like to thank my family for their support in everything I do in life. Finally, a very special thanks goes to my partner Kerri with whom I share my whole life, including the trials and tribulations of an engineering doctorate.

Research outcomes

Oral Presentation:
M. W. Smillie, M. Silver and S. T. Lee, “Passive Q-switch materials for Nd:YAG laser systems”, Thales Electro-optics and Algorithms symposium, Glasgow, 2012

Poster Presentation:
M. W. Smillie, M. Silver and S. T. Lee, "Passive Q-switch materials for diode pumped Nd:YAG laser systems", 2013 High Power Diode Lasers and Systems Conference (HPD), Coventry, pp. 26-27, 2013

Oral Presentation
M. Smillie, M.Silver, S. T. Lee, “High single-pulse energy, passively Q-switched Nd:YAG laser for defence applications”, presented at the annual IDC photonics conference, Heriot-Watt University, Edinburgh, 2014

Oral Presentation:
M. Smillie, M. Silver, S. T. Lee, T. J. Cook, “High single-pulse energy, passively Q-switched Nd:YAG laser for defence applications”, Proc. SPIE, 8959, Solid state lasers XXIII, 2014

Oral Presentation:
M. Smillie, M. Silver, S. T. Lee, T. J. Cook, “Passively Q-switched Nd:YAG laser for application in military designators”, 6th International Symposium on OPTRONICS IN DEFENCE AND SECURITY, OPTRO, Paris, 2014

Abstract

In this research project we assess the potential for a passively Q-switched, diode end pumped 1064 nm Nd:YAG system to be implemented in future generations of military target designators. The main challenges were to achieve a pulse energy above 50 mJ, timing jitter below ± 5 μs, and ensuring operation over a temperature range of -40 to +70 °C. We have addressed these challenges and established a framework for future research into passively Q-switched designators.

We found that the limited pulse energy was due largely to a non-uniform pump beam, which was corrected with an engineered diffuser. This enabled us to achieve a single pulse energy of 53.4 mJ, which is the highest reported energy for a diode end pumped, passively Q-switched 1064 nm Nd:YAG laser.

Secondly, we identified, through experiment and modelling, that the main causes of timing jitter in our system were mechanical vibrations and pump power fluctuations. We also investigated the presence of satellite pulses, which we experimentally attribute to longitudinal mode competition.

We also provide a summary of the Q-switching performance of V:YAG, Cr:YAG and BDN (bis[4-dimethylaminodithiobenzil] nickel) dye saturable absorbers, through experiment and rate equation modelling. From this we can confirm that Cr:YAG is the only commercially viable material suitable for high energy passive Q-switching at 1064 nm.

Finally we evaluated the thermal performance of a mechanically robust Nd:YAG laser passively Q-switched with Cr:YAG. The pulse energy, duration, jitter and threshold were measured over the temperature range -40 to +70 °C. Through modelling we propose that the experimentally observed changes in the laser parameters are driven by the temperature dependence of the effective emission cross section (Nd:YAG), pump power and laser mode size.

Table of figures

Table of contents

Chapter 1 Introduction to Passive Q-switching for applications in military target designators

1.1 Military lasers

The defence industry has been using laser technology virtually since the invention of the first laser in the 1960s. There are a number of technologies which are based around laser systems, including laser radar [1] and laser rangefinding [2]. The research in this thesis is focused entirely on the application of lasers in military target designators. This technology is used to perform accurate tactical strikes on enemy targets, whilst minimising any collateral damage or civilian casualties. The illustration below is taken from a report [3] by the Center for New American Security in Washington. This report outlines the progression of military technology over the past decades, with Figure 1.1 highlighting how laser technology has improved accuracy and safety in targeted military strikes.

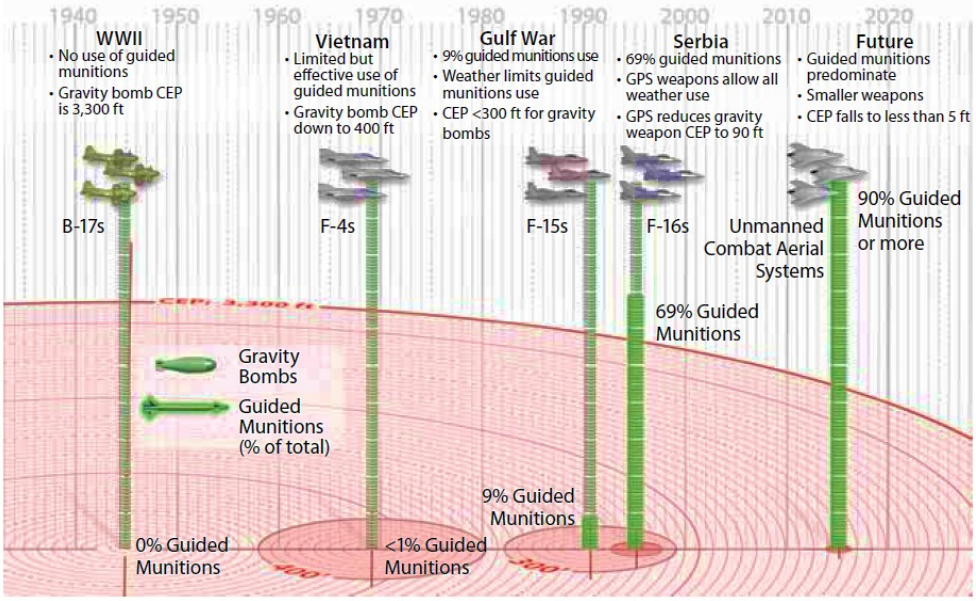

Figure 1.1: Illustration of the improvements in the accuracy of aerial munitions throughout the last century [3]. The pink circles (CEP) define the radius in which 50% of munitions fall.

The metric of accuracy used in Figure 1.1 is the CEP (circular error probable), which defines the circular radius (shown in pink in the above figure) within which 50 % of munitions will land. Here we can see between the 1940s (World War 2) and late 1990s (during the war in Serbia) the impact radius of aerial munitions has decreased dramatically, falling from 3300 ft to 90 ft, respectively. This has in part been due to the emergence of guided munitions, which include laser target designation. The forecast is that the CEP will be as low as 5 ft, which represents considerable improvements in missile safety.

1.2 Laser target designation

Laser designation is the technology for which this research project is based. We will now outline the process of laser target designation, as presented in the figure below.

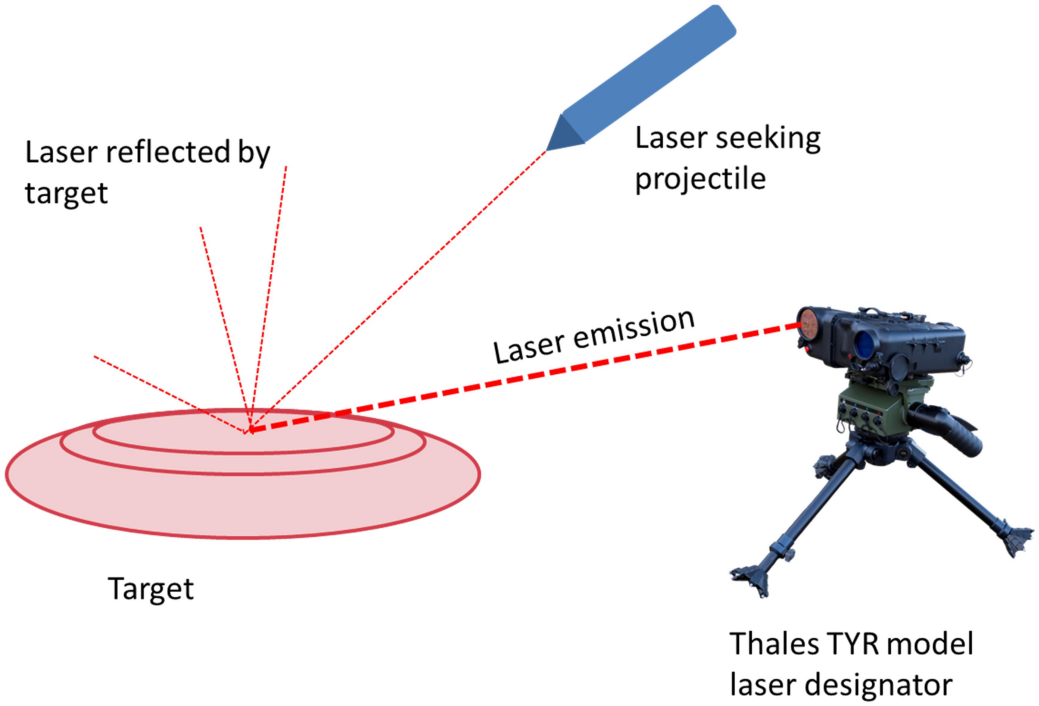

Figure 1.2: Illustration of the process of laser designation.

The laser designator operator directs the laser emission at the target, whilst the projectile is launched from the air in the general direction of the target. There is a laser seeker inside the nose cone of the missile, which is a multisegment detector array that is sensitive to the scattered laser light from the target. Depending on the

amount of collected signal from each segment of the array, the munitions control system will steer it towards the target. The laser source uses an encoded pulse repetition frequency to ensure that the seeker travels towards the correct designated target, and prevent interference from other laser sources. For this reason, a pulsed laser source is required with the system being able to select from a standard code set. A laser transmitter suitable for designation is required to have the following properties:

- High energy pulses (>50 mJ) – for detection at long ranges
- High peak power – for increased signal above seeker detection limit
- Wavelength to correspond with detectors in missile seeker (1064 nm)
- Repetition frequency of 10 – 20 Hz
- Compact design and low power consumption– to be man portable or to fit into sensor gimbal
- Well defined pulse modulation and timing – to encode the seeker reference signal
- Low beam divergence for increased range performance (up to 10 km) and to minimize scattering from adjacent objects around the target

In the following sections we will describe the design choices which ensure a laser system fulfils these criteria. Firstly we consider the methods of generating a laser pulse.

1.3 Short Pulse Generation

There are many ways of operating a solid-state laser system in pulsed mode, with some of the techniques having entire fields of research dedicated to them. Of the main laser configuration, there are three types of particular interest for our application. They are modelocking, Q-switching and gain switching. The method that can produce the shortest pulses is modelocking. Here the longitudinal modes of the laser are locked in phase, and the Fourier transform of this phase locked comb of modes is a short pulse [4]. Durations as short as 10 ps have been achieved by modelocked Nd lasers [5] [6]. A major drawback is the relatively large number of components required for this type of system, making compactness a challenge [7].

A slightly longer pulse can be achieved using gain switching. Here pulsed pump source is used to switch the population inversion in the gain material from low to high in quick succession. The resulting pulses are generally much longer, of the order of 100 ns. The pulse energy is also extremely limited, as the energy stored in the gain material is relatively low [4].

As a result, the industry standard method of short pulse generation is Q-switching. This technique involves rapidly switching the cavity losses from high to low after energy has been stored in the laser gain medium. The achievable peak power and pulse energy are suitably high (> 50 mJ) for designation. The pulse durations are typically in the range of 10 ns and the systems can be made compact and rugged. It is for these reasons that the research project is based entirely on Q-switching. We will now describe the mechanism of Q-switching.

1.4 Q-switching

1.4.1 What is Q-switching?

A method of producing high energy, nanosecond pulses is Q-switching. This technique involves altering the cavity Q-factor, which is related to the ratio of the stored energy in the cavity to the losses per round trip. The basic principle is the Q of the cavity starts off low (i.e. a high absorbing cavity), whilst the gain medium is being pumped, preventing laser emission. The losses in the cavity are therefore higher than in CW operation, hence the level of inversion (i.e. gain), and therefore stored energy, reached is greater. When the cavity Q is suddenly ‘switched’ to high (i.e. low absorbing cavity), the losses immediately become lower than the round-trip gain and laser emission can occur. Laser action continues until the excited ions within the gain medium are depleted. Effectively, energy is stored in the gain medium, by creating high inversion, which is released extremely quickly when the cavity losses are lowered by the Q-switch.

The following diagram (Figure 1.3) from Koechner [7] illustrates how the pump power (represented by flashlamp current), resonator losses, inversion and photon flux progress throughout the production of a Q-switched pulse.

As seen in Figure 1.3, the inversion builds at a rate relative to the pump power (in this case depicted as flash lamp current). During this initial phase the cavity losses are held high by the Q-switch, until at point t=0, when the cavity losses are rapidly switched to low. During this phase the inversion rapidly depletes, which results in a surge in the emitted photon flux proportional to the change in inversion.

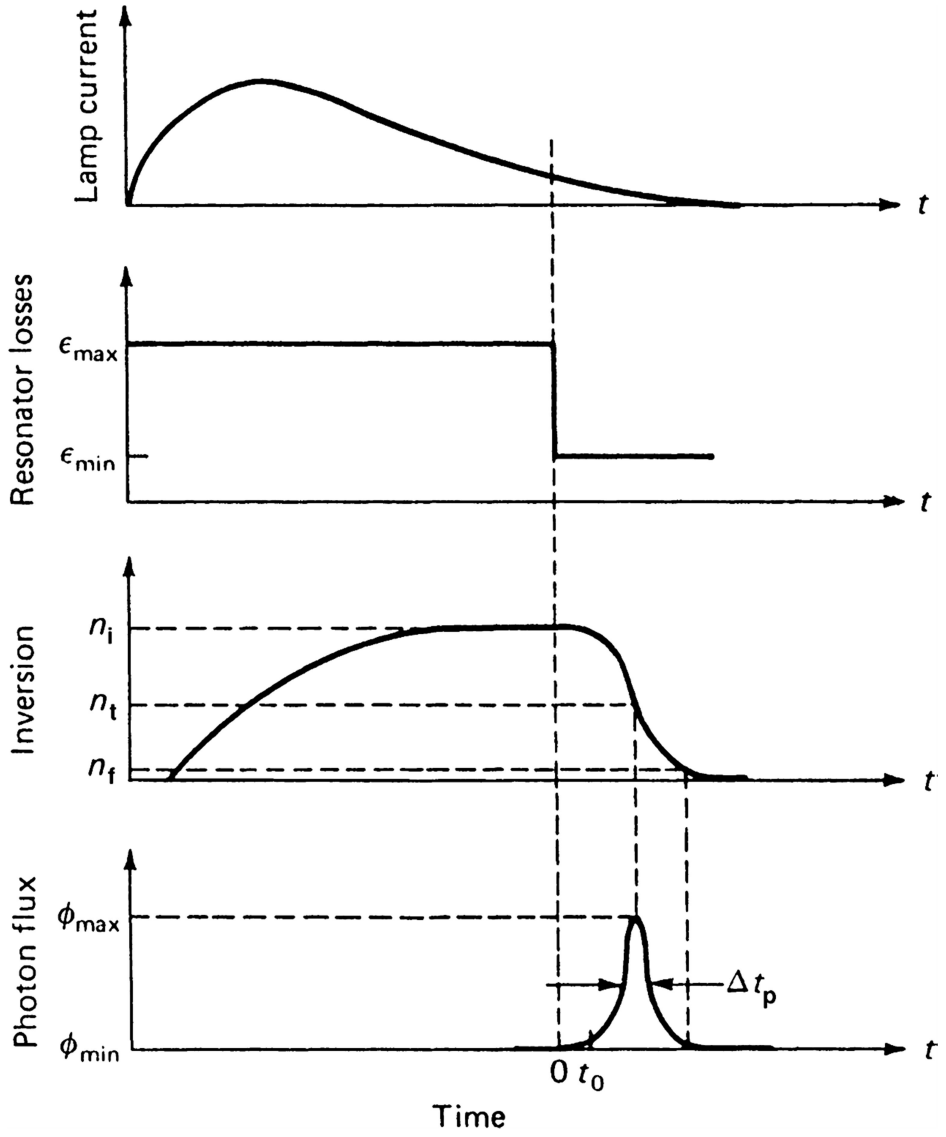

Figure 1.3: Diagram of flash lamp current, resonator losses, inversion and photon flux against time during the production of a Q-switched pulse [7].

There are a variety of methods for Q-switching the cavity of a laser, but they can all be set into two categories: active or passive Q-switching.

1.4.2 Active Q-switching (AQS)

The active regime involves the introduction of a component into the laser resonator which has an externally controllable loss mechanism. Examples of such elements are: a Pockels cell acting as a fast shutter; a rotating mirror, which induces a relatively gradual change in cavity losses; or an acousto-optic Q-switch, in which the refractive index of a material is altered by an applied acoustic wave. These methods are all currently in widespread use for Q-switching, although they do have one common flaw. They all require some form of driving circuit to operate them, which limits the compactness of the system and puts additional strain on power sources, which is relevant in portable applications such as designators. A Pockels cell, for instance, is small compared to the overall cavity but usually needs a high voltage driver that can be quite bulky and electrically noisy. In another instance, a rotating mirror is slightly larger, but also requires additional power to drive a motor which rotates the mirror and hence add complexity and moving parts. To overcome these obstacles, the solution comes in the form of passive Q-switching.

1.4.3 Passive Q-switching (PQS)

This technique involves the addition of an intra-cavity saturable absorber. The saturable absorber comprises of a material that has an intensity dependent transmission at the laser wavelength. When the intra-cavity fluence is low, the transmission of the saturable absorber, and therefore the cavity Q, is low. This prevents laser emission and the gain increases until the intra-cavity fluence reaches a level sufficient to bleach the saturable absorber. This level is governed by the material properties of the saturable absorber. At this moment the saturable absorber becomes sufficiently transparent (i.e. saturated), that lasing occurs and a short pulse is produced. Since the material requires no external driver, the strain on the power supply is lowered and the compactness increased, relative to active Q-switched systems. Another advantage is the increased durability, owing to the absence of moving parts in the laser system. These are all especially important issues in systems such as portable laser designators, where space and power are limited and the rugged environments stress mechanical systems to the limit. The most prominent challenges

of using a passive Q-switch over an active one are the following: the precision of its transmission modulation is poor, resulting in higher levels of output pulse timing jitter; the residual losses of the saturated material are generally greater which reduces the maximum pulse energy. Overcoming these shortcomings would result in the efficient production of high energy, short Q-switched pulses, which would be an attractive option for military applications. The specific requirements for the military application are outlined in the next section.

1.4.4 System requirements for laser designators

Laser designators are employed in some extremely hostile environments and therefore, the physical demands on the unit are high. The device has to be capable of withstanding both extreme heat and cold, on top of the general physical stresses associated with field use (e.g. shock, vibration). For this reason, the laser design has many constraints, including thermal stability of the pump source and lifetime of the components.

The requirement for low power consumption (e.g. batteries) of the laser also places limitations on the design; for example, active cooling becomes impractical where power is limited. In terms of the function of the laser itself, there are six parameters associated with Q-switched pulses that have to be considered. The wavelength, energy, repetition rate and timing jitter are directly specified in NATO STANAG 3733 [8], which makes them the most significant requirements. The pulse duration and beam quality are less defined requirements, but are important engineering considerations none the less. They define the energy incident on the target, and hence, the available scattered light that can be picked up by the seekers. The first specification is that the emission wavelength has to be 1064 nm, and is set by the detection wavelength of the seekers. The next specification is the energy of the generated pulse, which has to be above 50 mJ, to ensure an adequate signal is scattered on reflection for the seeker's detector(s) to distinguish it above noise levels. Thirdly, the repetition rate of the laser is required to be set to 20 Hz, and is modulated according to the pulse frequency security codes provided in the STANAG document. The next key parameter is the pulse duration, which is dictated by several factors such as resonator length and the fluorescence lifetime of the laser gain

medium. Whilst there are no specific criteria for pulse duration in the specifications, it is important when considering peak power as the seekers are threshold detection devices. It is generally accepted that the pulse duration should be of the order of 10 ns to allow a sufficiently high peak power. Another notable parameter is the beam quality, conveyed by the FWHM beam parameter product (BPP). This value is the FWHM far-field beam divergence angle multiplied by the far-field beam diameter. A general rule of thumb is for the BPP to be less than 15 mm mrad in all directions, to prevent radiation spilling beyond the target and creating false targets. The final parameter of note is the pulse-to-pulse timing jitter. This has to be within $\pm$ 5 µs to allow accurate detection of the frequency encoded signal. Jitter will be handled in detail in chapter 3. A summary of the required laser parameters is presented below.

Table 1.1: Table of laser pulse parameters required for laser designators. Parameters denoted with * are criteria specified by NATO STANAG 3733.

Wavelength	1064 nm *
Timing jitter	$\pm$ 5 µs *
Single pulse energy	> 50 mJ *
Pulse duration	$\approx$ 10 ns
Repetition rate	20 Hz *
Beam quality (FWHM BPP)	< 15 mm mRad

Another notable restriction on performance is that only one pulse per cycle is produced, rather than dual or multiple pulses. This can occur if the Q-switch opens too slowly compared to the cavity round trip time [9]. With these design rules in place, the constituents of the laser cavity can be conceived, starting with the laser gain material.

1.5 Laser Gain Medium

When designing a laser system, selecting a suitable laser gain medium is essential. A doped dielectric material (often described as a solid-state material) will be used as the laser gain medium in our system, but there are other types, including gas, dye and semiconductor mediums. A solid-state laser gain medium consists of an activator ion embedded or doped within a host material. Careful selection of these elements and the choice of pump source can tailor the laser system to a specific application. If the original activator ions have a very narrow absorption bandwidth the addition of a sensitiser ion to the gain medium broadens the pump absorption bandwidth of the laser medium [10]. This permits a drift in pump wavelength, which is typical of semiconductor pump sources when operated at different temperatures, while maintaining good absorption of the pump. The lanthanides, or rare earth metals, have proven extremely popular as activation ions due to their sharp fluorescence lines and strong absorption bands corresponding to the emission bandwidths of commercially available laser diodes. If a flash lamp were to be used to pump the laser, the medium would require a broad absorption spectrum as the lamp emits over a wide wavelength range, of around 1000 nm [7]. In our case, the system is diode pumped, therefore a relatively narrow absorption bandwidth is preferable [3] of the order of a few nanometres. There are many materials available when selecting a host for the active ions, glasses and crystals being the two broad categories. The host material contributes mostly to the physical and macroscopic optical properties of the medium. The physical properties of the material are also important. The thermal properties have to be such that temperature changes do not distort the optical properties of the medium, and thermal conductivity has to be sufficient to allow proper thermal management. Whether thermally induced birefringence in the medium is an issue, also needs consideration during the laser design process. By far the most crucial aspect in terms of designation is that the output wavelength is 1064 nm, as dictated by STANAG 3733. This unfortunately severely limits the number of available gain crystals to Nd:YAG and Nd:YVO_4. It is for this reason we will only consider these crystals, with an additional note on the potential for using ceramic materials.

1.5.1 Nd:YAG

By far the most popular solid-state laser gain medium is trivalent neodymium doped yttrium aluminium garnet or Nd^{3+}:YAG, emitting at 1064 nm. Trivalent neodymium ions benefit from long fluorescent lifetimes and narrow emission linewidths, characteristics shared by most rare earth metals. Although many crystals have been explored as neodymium hosts (i.e. vanadate), YAG has remained the standard host for neodymium ions due to its excellent optical, mechanical and thermal properties and was the host used since the inception of target designator back in the late 1960s [11]. Some properties are shown below, for a sample with a doping of 1.0 at. % [7].

Table 1.2: Physical properties of 1.0 at. % doped Nd:YAG at 300 K [7].

Knoop hardness	1320 kg mm^{-2}
Density	4.56 g cm^{-3}
Melting point	1970°C
Tensile strength	200 MPa
Modulus of elasticity	310 GPa
Thermal conductivity	0.14 W cm^{-1} K^{-1}
Specific heat	0.59 J g^{-1} K^{-1}
Thermal diffusivity	0.046 cm^2 s^{-1}
Thermal expansion	7.5 x 10^{-6} K^{-1}
$\partial n/\partial T$	7.3 x 10^{-6} K^{-1}

In terms of the laser properties, Nd:YAG has two important pump absorption bands at 730 nm and 800 nm, which is convenient for diode pumping since there are commercially available laser diodes across this wavelength range. The transitions from the pump bands to the laser level are shown below in Figure 1.4. There is a fast relaxation from these higher pump bands to the $^4F_{3/2}$ level. The 1064 nm laser emission occurs with the transition from this level to the $^4I_{11/2}$ level, with a lifetime of 230 μs. This then terminates with another fast non-radiative transition to $^4I_{9/2}$ level.

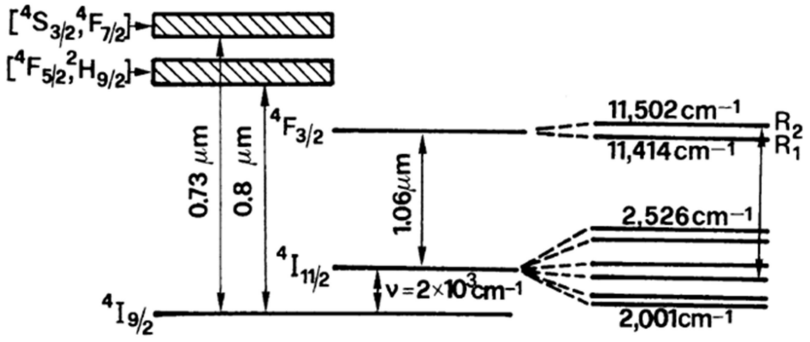

Figure 1.4: Simplified energy level diagram showing the pump bands and laser transitions in Nd:YAG [4]. The 1064 nm laser emission is a result of $^4F_{3/2}$ to $^4I_{11/2}$ transition, which subsequently terminates by non-radiative relaxation into the $^4I_{9/2}$ ground level.

The long lifetime of the upper laser level ($^4F_{3/2}$) allows an appreciable population inversion to be achieved, and therefore high gain, through pumping of the absorption bands. This allows a large stored energy to build up during the high loss phase of Q-switching, leading to efficient, higher energy Q-switched pulses [12]. The Nd^{3+} ions are of a larger radius than the yttrium ions, which they replace. This makes it more difficult to achieve large concentrations of Nd^{3+} ions within the YAG host. Commercially available concentrations of Nd^{3+} have typically been limited to around 1 at.%, above which the optical quality of the crystal starts to diminish [7]. Neodymium concentrations of around 4 at.% have been grown, unfortunately exhibiting higher thresholds and self-quenched fluorescence, typical of high concentrations of Nd^{3+} [13]. Many of the laser systems designed for military applications have historically used Nd:YAG as the gain medium. Specifically for designators, it is the only material used. The only other currently viable material, in terms of the strict 1064 nm requirement, is Nd:YVO_4.

1.5.2 Nd:YVO_4

As the only viable alternative to Nd:YAG, it is important to at least consider some of the properties of Nd:YVO_4. A comparison of some important laser properties is shown below. The most significant improvement over YAG is the more consistent output over temperature in a diode pumped system, as shown below.

Table 1.3: Table of some important laser properties comparing Nd:YAG and Nd:YVO_4 [7]

	Nd:YAG	Nd:YVO_4
Peak absorption coefficient (at ~808.5 nm)	11 cm^{-1}	34 cm^{-1} (π-polarisation)
Fluorescence lifetime	230 µs	100 µs
Stimulated emission cross section	2.8 x 10^{-19} cm^2	15.6 x 10^{-19} cm^2

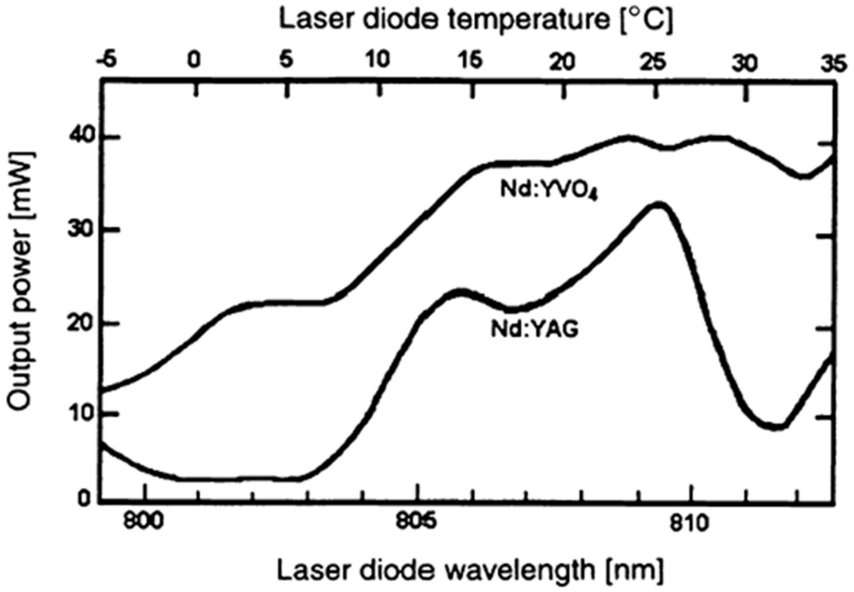

Figure 1.5: Example taken from Koechner [7][14], of CW output power against pump wavelength for Nd:YAG and Nd:YVO_4, illustrating the improved pumping mechanics of Vanadate. Laser diode temperature is also shown on the x-axis, representing the variation of diode emission wavelength with temperature.

It can be seen from Figure 1.5 that the laser output power is consistently higher in the Nd:YVO_4 case. This is in part due to the higher and smoother pump absorption spectrum in vanadate, as the diode pump emission wavelength tunes with temperature. The Stark splitting in the pump absorption levels is less prominent than with YAG, leading to more consistent absorption profile, and a more efficient laser output with varying diode temperature. Although this is especially important for military applications, where large temperature variations (-40 to +70 °C), there are two significant drawbacks which render vanadate unviable. Firstly, the lifetime of the

upper laser level ($^4F_{3/2}$) is much shorter (100 μs) than in Nd:YAG (230 μs). This means that the population inversion will not be retained for as long, as in YAG, before fluorescence decay begins to deplete the stored energy. This will lead to lower energy Q-switched pulses. Secondly, the stimulated emission cross section of the 1064 transition in vanadate (15.6 x 10^{-19} cm^2) is many times greater than in YAG (2.8 x 10^{-19} cm^2). This again reduces the stored energy capacity in an equivalent Nd:YVO_4 system, by reducing the threshold inversion of the system. A lower threshold inversion results in less stored energy being released in the Q-switched pulse. This furthers the challenge of achieving high energy passively Q-switched pulses. It is for this reason that we are not considering Nd:YVO_4 in our research. One interesting material group is ceramics, particularly Nd:YAG ceramic laser rods.

1.5.3 Ceramic gain materials

Ceramics have recently emerged as a potential alternative to single crystal laser gain materials. The ceramic materials are made by sintering pure mixtures of Nd and YAG powders, which is a simpler and less time consuming process than crystal growth. Research in ceramic gain mediums has made available high quality, highly doped Nd:YAG rods, with the advantage of cheaper production methods and the possibility of larger rods. The benefit of a ceramic material over a crystal, particularly with Nd:YAG, is that much higher Nd doping concentrations can be achieved, with a lower incidence of self-quenching [15]. Good quality ceramic gain materials are currently being produced and successfully implemented in passively Q-switched laser systems [16][17]. There are currently not enough commercial suppliers of ceramic Nd:YAG, to even consider it as a viable material for the military market. In future, it would be useful to research these materials when they do become more readily available. We will not be researching ceramic materials as part of this project. The next laser component we will consider is the optical pump.

1.6 Optical Pumping

When designing a laser system the method by which the gain medium is pumped is of vital importance. The pump source in a high-energy passively Q-switched system is required to energise a large gain volume in order to reach a very high threshold inversion and produce a single pulse above 50 mJ. This typically requires kiloWatts of pump power delivered within a pulse duration in the region of 200 μs (for Nd:YAG). Depending on the nature of the gain medium, many different methods of pumping are available. Unfortunately for solid-state mediums, optical pumping remains the only feasible option. When designing an efficient pumping regime both the optical source and the geometry of the system are important. When selecting a pump source important considerations are: how well the absorption band of the laser gain medium overlaps with the emission spectra of the pump source; whether it is able to meet the power requirements of the system; how efficient the source is; and the cost and reliability of the source. For the pump coupling configuration an efficient system requires: correct matching of the inversion volume in the gain medium with the laser mode volume; and proper matching of the absorption length and physical length of the gain medium. For the specific case of Q-switched operation, large pump energies are required to be delivered within a duration of around 200 μs in our system. Whilst considering these design aspects, we will now describe the challenges associated with the pump source itself.

1.6.1 Pump Source

There are two methods of optical pumping, using diode lasers or with a flashlamp. First we will consider the flashlamp method.

1.6.1.1 Flashlamps

Conventionally, military Q-switched solid state lasers have been pumped with a gas discharge ‘flashlamp’. The output light comprises of a continuum of different wavelength components delivered as an intense ‘flash’ of light. The characteristics of the output spectrum depend on the type of gas that fills the lamp and the current density in the lamp. In terms of efficiency, flashlamps are reasonably efficient sources with as high as 60% of the electrical input being converted to light emission.

However, since this radiation is spread over a continuum, the amount of energy absorbed by the laser gain medium is limited, owing to the absorption bands of most solid state materials being narrow compared with the flashlamp spectral bandwidth. This lowers the efficiency of a flashlamp pumped system [7]. Despite this, flashlamps are able to deliver sufficiently high energy pulses to produce high energy Q-switched pulses. One of the major drawbacks of using a flashlamp is the large amounts of heat involved in the process. As much as 50% of the input energy is dissipated through the electrodes and quartz walls of the lamp. In a fully integrated laser system, this can induce a whole host of undesirable thermal effects in the driving electronics and laser components. By far the most significant factor driving the move away from using flashlamps is their high power supply requirements, due to the spectral mismatch and waste heat. Batteries represent a large proportion of the total weight of a man portable designator system, and are therefore a major design consideration. A more desirable alternative to flashlamps are laser diode systems.

1.6.1.2 Laser diodes

Remarkable improvements in the efficiency of solid-state laser systems have resulted from the introduction of laser diode pump sources. From a product design perspective, they have an increased product lifetime compared to that of flashlamps [7]. They also benefit from having much narrower spectral linewidths than flashlamps, which allows greater spectral overlap of the pump emission with the laser gain medium absorption band. As a result, less waste heat is produced, reducing undesirable thermal effects in an integrated laser system. One aspect of thermal management which is more significant for diode pumps is thermal induced wavelength shifts in the output light. This may move the diode emission outside of the absorption band of the laser gain medium, preventing operation of the laser. The resulting change in output efficiency was shown previously in Figure 1.5, which highlights how important this consideration is for an Nd:YAG system.

The immediate advantage of using diode laser pumps is the directionality of the beam, which allows for highly compact geometrical configurations. These will be discussed further in the following section. However, a necessary consideration is the high vertical divergence which requires fast axis collimation (FAC). The limiting

factor in diode pumping, however, has always been their limited power output. A single diode emitter, having a maximum of 7 W CW output, would not be sufficient for high energy Q-switching. Laser diode bars, consisting of a row of devices, are available for higher power requirements, but still do not meet the power requirements. Diode laser stacks, made by stacking up to 16 bars, are compact arrays of diodes capable of producing around 3 kW of output, sufficient for high energy Q-Switched pulse production [9].

An example of the type of diode stack we will be using in our experiments is presented in Figure 1.6. This is taken from a technical drawing of a 3 kW, 12 bar diode stack provided by DILAS [18].

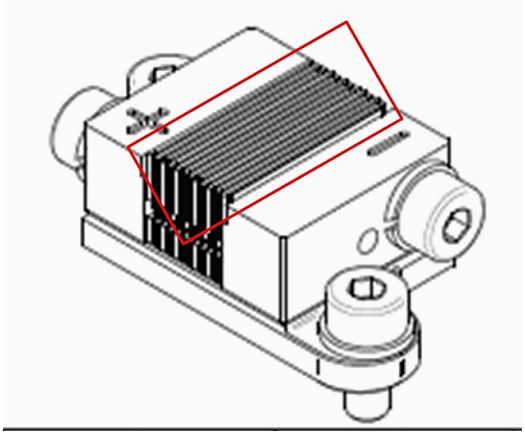

Figure 1.6: Design drawing of 3 kW 808 nm diode stack provided by DILAS [18].

The area highlighted in red in Figure 1.6 shows the *stripy* emitter surface of the diode stack. This presents a challenge as the resulting pump beam profile is very non-uniform and not well suited to passive Q-switching. This challenge will be the central focus of chapter 2. We will now discuss how different geometrical pump configurations affect the laser output.

1.6.2 Pump Geometry

Many methods of transferring pump energy to the laser gain medium exist, each with different merits and applications. Pump configurations can be placed into two categories, either *end* or *side* pumped. The critical factor for efficient pumping is the distribution of pump light throughout the laser gain medium along the axis of laser propagation. Careful design of the cavity focusing, optical coatings and other subtle

adaptations are required to optimise the efficiency of the cavity, depending on the optical properties of the gain material. The following explanations of side and end pumping regimes consider the case of diode pumping of cylindrical rods.

1.6.2.1 End Pumping

When considering flashlamps and diodes, only laser diodes can be used for end pumping, owing to the directionality of the diode output beam. Below is a schematic of an example end-pumped configuration.

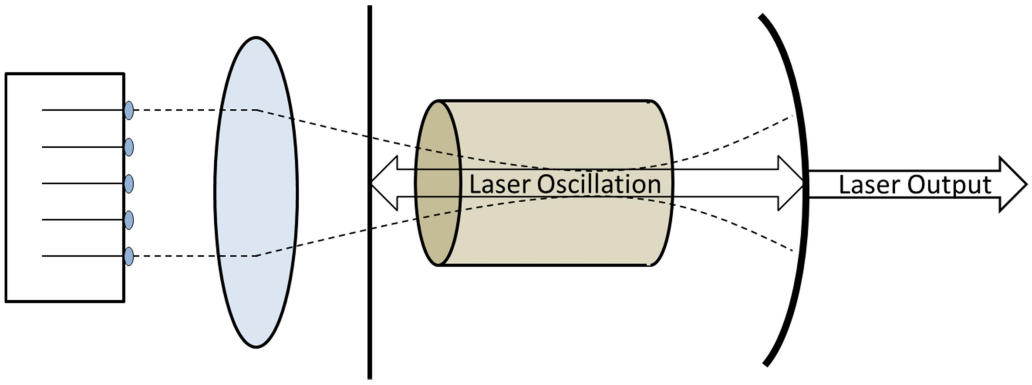

Figure 1.7: Schematic diagram of end-pumping regime, components from left to right are: Diode Laser bar with integrated micro optics, Slow-axis lens, HR cavity mirror, laser gain rod, curved output coupler.

Here the beam is directed onto an open facet and through the rod using some form of coupling optics, as shown in Figure 1.7. The volume of inversion (i.e. gain) is dependent on the distribution of the pump mode transverse to the axis of laser oscillation, which is controlled by the choice of optics employed to focus (or collimate) the diode radiation into the medium. The most important factor when considering the design of the pump system is the spatial uniformity of the pumped gain volume. A non-uniform transverse pump power distribution leads to a lower volume of energised gain material, and therefore reduces the Q-switched pulse energy. This makes it essential to include some pump beam homogenisation, to smooth the transverse beam profile of a laser diode stack. The advantage of using an end pumped system is that, provided the rod is sufficiently long, it can be guaranteed that the pump will be fully absorbed by the gain medium. This is especially important for a diode pumped system, for which the emission wavelength of the

pump varies with temperature (approximately 0.3 nm $°C^{-1}$). Particularly in Nd:YAG (see Figure 1.8), which has a highly variable absorption spectrum.

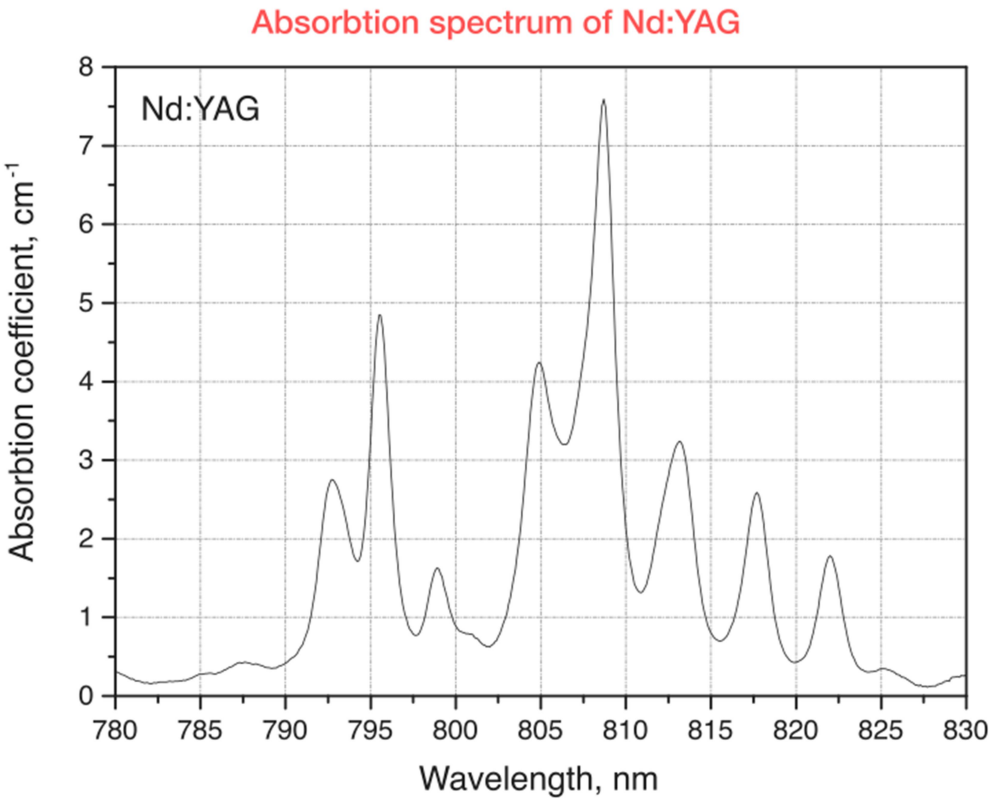

Figure 1.8: Absorption spectrum of 1.1 at. % doped Nd:YAG [19].

In addition, an end-pumped system typically has significantly better pump-laser mode matching compared with side pumping, due to the pump beam being directed along the direction of laser oscillation, leading to higher efficiency. Whilst this is certainly true for a single diode emitter, the poorer beam quality of diode stacks considerably reduces this advantage of end-pumping. It is this challenge which forms the basis of chapter 2, in which pump beam homogenisation will be the focus. The main alternative to end pumping is side pumping, which we will now describe.

1.6.2.2 Side Pumping

A side-pumped laser generally consists of one or more diode bars or stacks surrounding the gain medium. The diodes are placed parallel to the length of the gain medium as depicted in Figure 1.9.

Although this only illustrates the case of two diode stacks, many systems would employ several diode stacks/bars completely surrounding the rod, leading to a potentially more complicated mechanical design. The resonator mirrors are facing the rod end facets, and can take the form of a typical high reflectivity (HR) mirror and output coupler or reflective dielectric coatings on the rod itself. The principal advantage of the side pumped regime over end pumping is that large pump powers can be distributed, with better thermal loading, across the length of the rod, permitting higher powers of laser output. This is especially important for reaching high energy Q-switched pulses. The downside however is that the pump energy may not be fully absorbed since it is being directed at the smallest dimension of the rod (i.e. the diameter is generally less than the length). This can be made worse by the combination of temperature tuning of the diodes and the variable absorption spectrum of Nd:YAG, as described above. This requires additional coatings/reflectors to ensure the pump radiation stays within the rod and is fully absorbed, but with limited success.

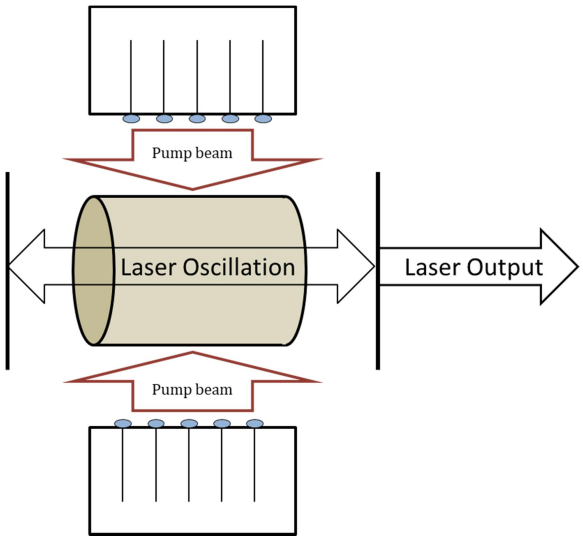

Figure 1.9: Schematic diagram of simplified side-pumping regime. Two diode stacks are placed above and below a central laser crystal, with two cavity mirrors either side.

The medium may be enclosed in a slotted reflecting capsule [20], which allows the pump light though the open slot to then be reflected inside the rod. Even with the additional reflectors, the varying absorption length with temperature is still

problematic. As the absorption length changes so too does the position of the inversion within the gain medium. This can have a detrimental effect on the shape of the transverse mode composition, and therefore the divergence of the emitted beam. It is for this reason, and due to the demanding military temperature specifications (-40 to +70 °C), that we are choosing to base our research on an end pumped system. We will expand more on this throughout the rest of the thesis. Now we will describe the key considerations for choosing a passive Q-switch material, also known as a saturable absorber.

1.7 Q-Switch Materials

In this section we will outline the design considerations of choosing a passive Q-switch material, starting with the physical mechanism responsible for saturable absorption.

1.7.1 Process of saturable absorption

The reason a saturable absorber is useful for Q-switching is that it has the ability to switch rapidly between a high loss and low loss state by the increase in cavity fluence. To explain this mechanism we will first describe the energy levels shown in a figure taken from Koechner [7].

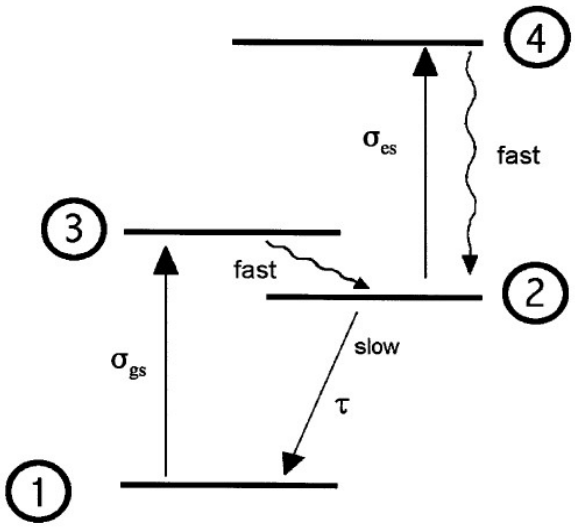

Figure 1.10: 4-level energy diagram illustrating the process of saturable absorption. Diagram is taken from Koechner [7]. Energy levels are labelled 1-4.

When the saturable absorber ions are in the ground state (1), they are in the low transmission phase. At this point they may be excited (and hence absorb photons), at a rate according to the ground state absorption cross section (σ_{gs}), into a higher energy state (3). There is then a very fast, non-radiative, decay into what is known as the excited state (2). This excited state has a long lifetime (4.1 μs in Cr:YAG [21], relative to the other levels, which allows a population inversion (between 1 and 2) to be established, once the resonating cavity fluence reaches a threshold level. Once this population inversion is attained, the saturable absorber is in the high transmission phase. Many absorbers also suffer from excited state absorption, between (2)-(4) in Figure 1.10, at a rate according to the excited state absorption cross section (σ_{es}). This reduces the efficiency of the passively Q-switched system by adding a residual, non-saturable optical loss. To summarise: a viable saturable absorber requires a relatively long excited state lifetime (τ) between states 2 and 1; and a ground state absorption cross section larger than the excited state cross section ($\sigma_{gs}>\sigma_{es}$). An illustration of how the transmission changes with increasing cavity fluence is shown below.

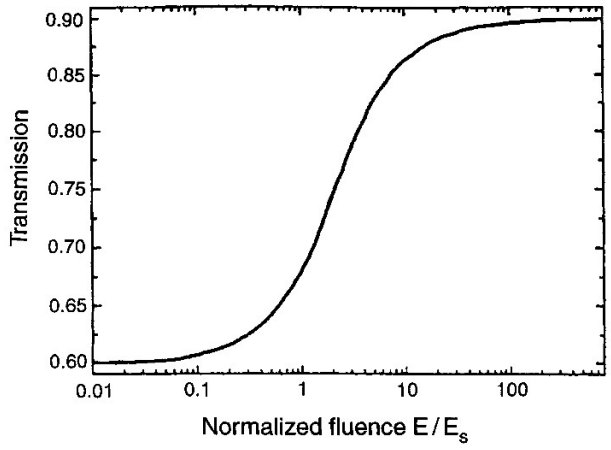

Figure 1.11: Saturable absorber transmission against normalised cavity fluence. Fluence (E) is normalised with the saturation fluence (E_s), which is the fluence required to reduce the absorption to 1/e of its initial value. Illustration is taken from Koechner [7].

It can be seen that, as the cavity fluence increases logarithmically, the saturable absorber transmission increases with a characteristic *S*-shaped curve. The initial (ground state) and saturated (excited state) transmissions are related to the absorption cross sections by the following equations:

$$T_0 = \exp(-n\sigma_{gs}z), \quad \text{Equation 1.1}$$

$$T_{SAT} = \exp(-n\sigma_{es}z), \quad \text{Equation 1.2}$$

where T_0 is the initial transmission and T_{SAT} is the saturated transmission, n is the total density of absorbing states in cm^{-3}, σ_{gs} and σ_{es} are the ground and excited state absorption cross sections, respectively in units of cm^2, and z is the thickness of the saturable absorber in cm. In terms of Q-switched pulse energy, the greater the difference between T_0 and T_{SAT}, the higher the pulse energy. From Equation 1.1 and Equation 1.2, this means that the greater the difference in ground and excited state absorption, the higher the Q-switched pulse energy. An ideal absorber would have no excited state absorption, thus maximising the excited state transmission to unity. Unfortunately the available saturable absorber Q-switches all have some level of excited state absorption. We will now evaluate the requirements of a saturable absorber for use in a military designator system.

1.7.2 Desirable material parameters for efficient high energy Q-switching

The main areas of consideration when selecting a saturable absorber material are the absorption spectrum of the material, the ground and excited state absorption properties, and the decay rate of the excited state. Different saturable absorber materials will have varying properties, dependent on the absorbing ion, host crystal and material preparation (i.e. growth process). In our case, we are mostly reliant on materials that are ready available.

The absorption bandwidth and wavelength of the material varies depending on the combination of the absorbing ion and the host material [22]. A survey of the manufacturer's specifications will quickly identify the materials with the relevant absorbing wavelengths. In our case we are limited to V:YAG and Cr:YAG which are both readily available and have absorption at 1 micron. We consider dye Q-switches in this study as they were used historically for passive Q-switching applications [23]. However, dye Q-switches are increasingly difficult to obtain from manufacturers.

Another important parameter to consider when selecting a saturable absorber is the initial transmission at the required laser wavelength. This value indicates the amount of additional gain required to reach threshold and subsequently dictates the peak power, duration and energy of the resulting Q-switched pulse. The saturated transmission [24] is also a key parameter when considering new materials for Q-switching. It dictates the amount of non-saturable, essentially parasitic, loss that is associated with insertion of the Q-switch. To maximise the pulse energy achieved, the transmission should be as close to 100 % as possible, to reduce any residual absorption. To optimise a passively Q-switched system, therefore, we would like a saturable absorber with the lowest initial transmission possible, that still allows the system to reach threshold consistently; and a high excited state transmission to maximise the resulting pulse energy. It is currently not possible to guarantee absorption values from the manufacturer, and they vary between manufacturers for the same material, and even between growth runs within a single manufacturer [25].

The excited-state decay rate of the material depend on the properties of both the host material and absorbing ion. This parameter is an intrinsic property if the material which does not exhibit significant variation between manufacturers. It is however, extremely variable between different materials. It becomes a crucial parameter when considering Q-switching in the nanosecond range. [26]. Traditional models (i.e. transcendental equations) assume that as long as the excited state decay rate is greater than or equal to the Q-switched pulse duration, the material is acceptable for the laser design [12] [27]. If the decay rate is too short, the Q-switch will essentially close too quickly during the release of the cavity stored energy, cutting the pulse short in duration and energy. We will explore this theory using rate equation modelling later in the thesis.

We can now discuss some of the different types of saturable absorber, categorised by their host materials. It should be noted that Cr:YAG and V:YAG are the only commercially available passive Q-switch materials for 1064 nm generation. We will evaluate BDN dyes which were used historically in military laser systems, but are no longer commercially available.

1.7.3 Cr:YAG, V:YAG and BDN

Cr^{4+}:YAG is the clear market leader for passive Q-switching in the 0.9-1.2 μm range. The doped Chromium (4+) ions within the crystal satisfy the high absorption cross section requirement whilst the YAG crystal provides the physical properties necessary for practical application, such as good thermal and mechanical performance [21].

V:YAG is the only other commercially available saturable absorber that has shown to be effective for Q-switching at 1064 nm, with similarly good thermal and mechanical properties as Cr:YAG [28]. A comparison of some of the properties of Cr:YAG and V:YAG is presented in Table 1.4..

Table 1.4: Table of absorption properties for Cr:YAG [29], V:YAG [29] and BDN dye [30].

	Cr:YAG	V:YAG	BDN
Excited state lifetime	4.1 μs	22 ns	5.7 ns
Ground state absorption cross section σ_{gs}	2.1×10^{-18} cm^2	1.0×10^{-18} cm^2	1.0×10^{-16} cm^2
Excited state absorption cross section σ_{es}	1.7×10^{-19} cm^2	2.2×10^{-19} cm^2	3.0×10^{-17} cm^2
β (σ_{es}/ σ_{gs})	0.081	0.22	0.33

First comparing the excited state lifetimes in Table 1.4, it can be seen that the excited state lifetime of Cr:YAG is orders of magnitude longer than V:YAG. A general guideline is that the excited state lifetime should be at least as long as the Q-switched pulse duration [27]. This is to ensure that the Q-switch does not close during production of the pulse, consequently preventing the full stored energy from being released in a single pulse. In the case of Cr:YAG this is not a problem, when we consider that the pulse duration of relevance in a designator is of the order of 10 ns. It is a concern for a V:YAG system, which may suffer from premature closing of the Q-switch due to the 22 ns lifetime.

The next relevant parameter is the β ratio of the excited state absorption and ground state absorption cross sections, assuming that σ_{gs} is greater than σ_{es}. A lower

β factor translates as a greater modulation of loss between the open and closed state of the absorber, and therefore a higher energy Q-switched pulse. This serves as a reliable way of quickly determining which materials would potentially produce higher energy pulses. Looking at Table 1.4, Cr:YAG has a lower β than V:YAG, and will therefore produce a higher energy pulse. It is for the reasons given here that our experiments will be based on a Cr:YAG system, with the exception of Chapter 4 which evaluates in more depth the suitability of each material. This chapter also considers BDN dye, which we will now summarise.

Historically, passively Q-switched systems have used plastic dyes, either in solution or mounted in thin films. Whilst the absorption wavelength is fixed for each material, the initial and saturated transmission and the excited state lifetime [31] are controllable by varying the concentration of the dyes within the host. This allows tuning of the output pulse width and energy [21][22]. These have been phased out due to poor component lifetime, and consequently they are no longer commercially available, with many systems being replaced with Cr:YAG. The dye we have available is BDN (bis[4-dimethylaminodithiobenzil] nickel) [31], prepared in a transparent acetate. From Table 1.4 we can see that it has a relatively fast decay time of 5.7 ns, which potentially means that it will not be suitable for Q-switching pulses longer than 10 ns. Interestingly, the absorption cross sections are 2 orders of magnitude greater than both crystals. We will investigate how this will affect the Q-switched pulse characteristics in detail in chapter 4. Now we will consider some of the systems described in the literature, which are relevant to our research.

1.8 Current systems employed

Here we will present some passively Q-switched systems found in the literature which use Nd:YAG as the gain material an Cr:YAG as the saturable absorber. When reviewing the literature we were looking for single pulse energies close to 50 mJ. We found that, despite the wealth of research into Cr:YAG and Nd:YAG, high energy systems are not well reported. The first laser we will look at is a flashlamp pumped Nd:YAG system with a Cr:YAG Q-switch.

1.8.1 Flashlamp pumped

This configuration, demonstrated by Jazi et al [34], produced a relatively high energy pulse (41 mJ) with a duration of 15 ns. This was achieved with a 1 at.%, 5 mm diameter cylindrical Nd:YAG rod, an output coupler reflectivity and Cr:YAG initial transmission of 50 % and 40 % , respectively. A corner cube was inserted in to the cavity to act as the high reflectivity mirror, which was reported to have improved laser stability and beam quality. The paper also reports the production of two conjoined (satellite) pulses. The multi-pulse regime was attributed to an increase in pump power allowing the inversion to build back up to threshold in quick succession. This would not be suitable for our application; a single pulse is required for designation because of the encoded repetition frequency. This is another drawback of flashlamp pumping, since the pump duration cannot be as precisely controlled as a laser diode.

1.8.2 Diode side-pumped

The increased availability of high power laser diodes for optical pumping has made high energy diode pumped systems feasible. A diode side pumped system presented by Lee. et. al. [35] illustrates how high the energies can be pushed using Nd:YAG and Cr:YAG. The 103 mm long, 4 mm diameter, 1 at.% doped Nd:YAG rod was placed in a 170 mm plano-concave (ROC = 10 m) cavity. Four pump diodes, with a total peak power of 3880 W, were aligned along the length of the laser rod. The rod was surrounded in a pump reflector cylinder, with a transparent window to allow the pump light to be incident on the rod from a single direction. A 9 % initial transmission intracavity Cr:YAG crystal and an output coupler reflectivity of 30 % were used. This yielded a 53 mJ, 10 ns Q-switched pulse from a 521 mJ, 200 μs pump pulse. It is promising to see that energies above 50 mJ have been achieved from a Nd:YAG/Cr:YAG system with a suitable pulse duration. The Q-switched pulse was seen to have a smaller satellite pulse accompanying the main pulse. This highlights the need to investigate the temporal properties of high energy Q-switched pulses, which will form the basis of chapter 3. Now we know that a diode side

pumped system can achieve energies above 50 mJ, we can look at end pumped configurations which will be the focus of our research.

1.8.3 Diode end-pumped

We were unable to find any research outputs with pulse energies as high as 50 mJ from diode end-pumped Nd:YAG/Cr:YAG laser. We know from work published by Lee and Silver et. al. that an end pumped system can produce pulse energies upwards of 60 mJ using an active Q-switch (Pockels cell) [36]. The system described in this paper has been adapted for our research to be used in thermal testing in chapter 5. Briefly, the design uses a folded resonator with monolithic HR/Output coupler mirror configurations and a retro-reflecting corner cube, for increased alignment stability.

1.9 Conclusion

In conclusion, we have discussed both the general requirements of a laser target designator module, the individual component specifications, and some examples of passively Q-switched systems reported in the literature. From surveying the literature, we conclude that energies above 50 mJ have been achieved with a diode end-pumped actively Q-switched system, and a side-pumped PQS laser. In this research project we combine these concepts and investigate a diode end-pumped, passively Q-switched Nd:YAG laser with reference to application as a laser target designator.

It is the aim of this thesis to evaluate how the laser target designator specifications can be met, and also gain a better understanding of passively Q-switched systems, by combined experimental and computational research. In Table 1.5 we present a summary of each chapter which will follow, with a note on which designator specifications will be the focus of each chapter

Table 1.5: Summary of each chapter contents, which designator requirements are the primary focus, and the corresponding specified value

	Chapter contents	Primary focus	Specified value
Chapter 2	Pump beam homogenisation	Energy	> 50 mJ
Chapter 3	Temporal instabilities	Timing jitter	$< \pm$ 5 μs
Chapter 4	Q-switch materials for 1064 nm	--	--
Chapter 5	Temperature testing	Operational	-40 to +70 °C

In Chapter 2 the focus will be on evaluating the need for pump beam homogenisation, and how this affects the laser output (QCW and Q-switched). The emphasis here will be on achieving single pulse energies above 50 mJ.

In Chapter 3 we investigate two temporal instabilities commonly found in passively Q-switched systems, timing jitter and satellite pulses. Firstly we assess the magnitude and mechanisms responsible for timing jitter in our system. We will first define what the jitter value describes in terms of fluctuations in a pulse train, and how we actually measured it. The mechanisms we will be investigating are, spontaneous emission noise, mechanical perturbations, pump power fluctuations, and mode competition. The second area of research in this chapter consists of identifying whether satellite pulses, as observed in the literature, contribute to the timing jitter; and also what the likely mechanism is for producing these secondary pulses.

Chapter 4 explores the material properties which make an efficient passive Q-switch, by comparing the experimental and computational Q-switching results for three materials, Cr:YAG, V:YAG and BDN dye. This includes firstly measuring the absorption cross sections of Cr:YAG and V:YAG, using a z-scan experimental setup.

Chapter 5 evaluates the function of a passively Q-switched system over the temperature range -40 to +70 °C. This required the construction of a mechanically stable chassis and resonator to house the components for temperature testing. We measured the change in pulse energy, duration, jitter and threshold. We explored some temperature dependent parameters in our rate equation model to describe the measured change in the output parameters of our laser during temperature testing. The modelled parameters we investigated were, pump power, effective stimulated emission cross section of Nd:YAG, Nd:YAG absorption coefficient, and Cr:YAG excited state decay rate.

1.10 References

[1] P. Mcmanamon, G. Kammerman, and M. Huffaker, “A History of Laser Radar in the United States,” *Proc. SPIE*, vol. 7684, pp. 1–11, 2010.

[2] N. Zafrani, “Forty years of lasers at ELOP–Elbit Systems,” *Opt. Eng.*, vol. 49,

no. 9, p. 091004, 2010.

[3] R. O. Work and S. Brimley, “20YY Preparing for War in the Robotic Age,” *Center for a New American Security*. 2014.

[4] O. Svelto, *Principles of lasers*, 5th ed. New York: Springer, 2010.

[5] Z. Zhang, L. Qian, D. Fan, and X. Deng, “Gallium arsenide: A new material to accomplish passively mode-locked Nd:YAG laser,” *Appl. Phys. Lett.*, vol. 60, no. 4, pp. 419–421, 1992.

[6] V. Kubeček, J. Marek, I. Procházka, K. Hamal, and G. C. Reali, “Active-passive mode-locked ND:Glass laser with passive negative feedback,” *Czechoslov. J. Phys.*, vol. 40, no. 8, pp. 937–939, 1990.

[7] W. Koechner, *Solid-State Laser Engineering*. New York: Springer, 2006.

[8] *Standardized Agreement 3733*, 2nd ed. North Atlantic Treaty Organisation, 2005.

[9] A. E. Siegman, *Lasers*. Sausalito: University Science Books, 1986.

[10] C. W. I, W. L. H. P. Weber, P. Rogin, and J. Hulliger, “Energy transfer in Yb 3+: Er3+:YLF,” *Opt. Commun.*, vol. 144, pp. 31–35, 1997.

[11] V. Molebny, P. McManamon, O. Steinvall, T. Kobayashi, and W. Chen, “Laser radar: historical prospective—from the East to the West,” *Opt. Eng.*, vol. 56, no. 3, pp. 031220-24, 2010.

[12] J. J. Degnan, “Optimization of passively Q-switched lasers,” *IEEE J. Quantum Electron.*, vol. 31, no. 11, pp. 1890–1901, 1995.

[13] Y. Urata, S. Wada, H. Tashiro, and P. Deng, “Laser performance of highly neodymium-doped yttrium aluminum garnet crystals.,” *Opt. Lett.*, vol. 26, no. 11, pp. 801–3, 2001.

[14] R. A. Fields, M. Birnbaum, and C. L. Fincher, “Highly efficient Nd:YVO_4 diode-laser end-pumped laser,” *Appl. Phys. Lett.*, vol. 51, no. 23, pp. 1885–1886, 1987.

[15] V. Lupei, a. Lupei, S. Georgescu, T. Taira, Y. Sato, and a. Ikesue, “The effect of Nd concentration on the spectroscopic and emission decay properties of highly doped Nd:YAG ceramics,” *Phys. Rev. B*, vol. 64, no. 9, p. 092102, 2001.

[16] T. Denis, S. Hahn, S. Mebben, R. Wilhelm, C. Kolleck, J. Neumann, and D.

Kracht, “Compact diode stack end pumped Nd:YAG amplifier using core doped ceramics.,” *Appl. Opt.*, vol. 49, no. 5, pp. 811–6, Feb. 2010.

[17] R. Huss, R. Wilhelm, C. Kolleck, J. Neumann, and D. Kracht, “Suppression of parasitic oscillations in a core-doped ceramic Nd:YAG laser by Sm:YAG cladding.,” *Opt. Express*, vol. 18, no. 12, pp. 13094–101, 2010.

[18] “N13N 808 nm 3 kW 12 bar diode laser stack technical drawing.” Gmbh, Dilas Diodenlaser, 2013.

[19] Crytur, “Laser rods - Neodymium doped,” *Nd:YAG laser material properties*, 2017. [Online]. Available: https://www.crytur.cz/products/laser-rods-neodymium-doped/. [Accessed: 08-May-2017].

[20] A. Levoshkin, A. Petrov, and J. E. Montagne, “High-efficiency diode-pumped Q-switched Yb : Er : glass laser,” *Opt. Commun.*, vol. 185, no. 4–6, pp. 399–405, 2000.

[21] Y. Kalisky, “Cr4+-doped crystals: their use as lasers and passive Q-switches,” *Prog. Quantum Electron.*, vol. 28, no. 5, pp. 249–303, 2004.

[22] A. Malyarevich and K. Yumashev, “Saturable absorbers based on tetrahedrally coordinated transition-metal ions in crystals (Review),” *J. Appl. Spectrosc.*, vol. 76, no. 1, pp. 1–43, 2009.

[23] D. Hull, “Combination laser Q-switch using a spinning mirror and saturable dye.,” *Appl. Opt.*, vol. 5, no. 8, pp. 1342–3, 1966.

[24] A. G. Okhrimchuk and A. V Shestakov, “Absorption saturation mechanism for YAG:Cr4+ crystals,” *Phys. Rev. B*, vol. 61, no. 2, pp. 988–995, 2000.

[25] G. Xiao, J. Lim, and S. Yang, “Z-scan measurement of the ground and excited state absorption cross sections of Cr4+ in yttrium aluminum garnet,” *IEEE J. Quantum Electron.*, vol. 35, no. 7, pp. 1086–1091, 1999.

[26] S. Kück, K. Petermann, U. Pohlmann, and G. Huber, “Near-infrared emission of Cr4+-doped garnets: Lifetimes, quantum efficiencies, and emission cross sections,” *Phys. Rev. B*, vol. 51, no. 24, pp. 17323–17331, 1995.

[27] G. J. Spühler, R. Paschotta, R. Fluck, B. Braun, M. Moser, G. Zhang, E. Gini, and U. Keller, “Experimentally confirmed design guidelines for passively Q-switched microchip lasers using semiconductor saturable absorbers: errata,” *J. Opt. Soc. Am. B*, vol. 18, no. 6, p. 886, 2001.

[28] A. M. Malyarevich, I. A. Denisov, K. V Yumashev, V. P. Mikhailov, R. S. Conroy, and B. D. Sinclair, "V:YAG – a new passive Q-switch for diode-pumped solid-state lasers," *Appl. Phys. B*, vol. 67, pp. 555–558, 1998.

[29] J. Šulc and P. Arátor, "Solid state saturable absorbers for Q-switching at 1 and 1.3 μm: investigation and modeling," *Proc. SPIE*, vol. 6871, p. 68712D–68712D–11, 2008.

[30] Y. S. Choi, "Saturation Characteristics of Cr(4)+:YAG Crystals and Dye Films for Passive Q Switches.," *Appl. Opt.*, vol. 40, no. 30, pp. 5417–22, 2001.

[31] Z. F. Zhu and E. M. Garmire, "Papers: Optical Bistability in BDN Dye," *IEEE J. Quantum Electron.*, vol. 19, no. 10, pp. 1495–1498, 1983.

[32] P. Kafalas, J. I. Masters, and E. M. E. Murray, "Photosensitive liquid used as a nondestructive passive Q-switch in a ruby laser," *J. Appl. Phys.*, vol. 35, no. 8, pp. 2349–2350, 1964.

[33] M. L. Spaeth and W. R. Sooy, "Fluorescence and bleaching of organic dyes for a passive Q-switch laser," *J. Chem. Phys.*, vol. 48, no. 5, pp. 2315–2323, 1968.

[34] M. Erfani Jazi, M. Dehghan Baghi, M. Hajimahmodzadeh, and M. Soltanolkotabi, "Pulsed Nd:YAG passive Q-switched laser using Cr4+:YAG crystal," *Opt. Laser Technol.*, vol. 44, no. 3, pp. 522–527, 2012.

[35] K. Lee, H. C. Lee, J. Cho, J. Lee, and J. Yi, "Optics & Laser Technology Passively Q-switched , high peak power Nd : YAG laser pumped by QCW diode laser," *Opt. Laser Technol.*, vol. 44, no. 7, pp. 2053–2057, 2012.

[36] M. Silver, S. T. Lee, A. Borthwick, I. McRae, D. Jackson, and W. Alexander, "Compact, diode-pumped, solid-state lasers for next generation defence and security sensors," *J. Phys. Conf. Ser.*, vol. 619, no. 1, 2015.

Chapter 2 The effects of diode pump homogenisation on QCW and Q-switched Nd:YAG laser output.

2.1 Introduction

One of the difficulties in using a passively Q-switched laser is the limited pulse energy, compared with an actively Q-switched system. As we have discussed previously, this becomes more challenging with an end-pumped design. In this chapter we will outline how we have overcome this by homogenisation of the high power diode stack. We will assess some of the homogenisation methods available and then present how implementing an engineered diffuser affects the QCW (quasi constant wave) and Q-switched output of our system. Firstly we will discuss some of the available methods of improving the pump beam profile.

2.1.1 Methods of beam homogenisation

There are several reported methods of producing a much more uniform beam from a diode laser stack. A relatively straight-forward method of guiding (by total internal reflection) the beam down a glass rod (commonly referred to as a *light pipe*) is presented by Traub et al [1](Figure 2.1).

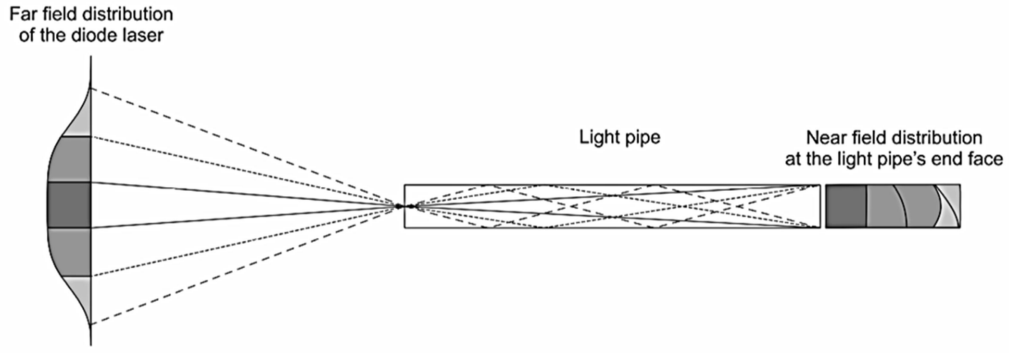

Figure 2.1: Schematic of laser beam homogenisation by a glass rod (light pipe) from Traub et al. [1]. Near field intensity distribution is gaussian at the input (left hand side) and a top hat at the exit (right hand side).

This method encompasses directing a divergent beam down the pipe with many total internal reflections occurring before exiting as a flat-top beam. As each reflection occurs, different spatial components of the beam are folded over each other, creating a slightly more homogeneous profile each time. After approximately 5 reflections, only 15 % of the beam lies outside the top-hat region of the beam profile, i.e. is 85 % homogenised. This system can also involve many more optics to first focus and couple the pump beam into the light-pipe, and then to collimate and couple the resulting homogenised beam into the laser rod. This kind of system can therefore be rather complicated and physically long.

Another possible technique for beam homogenisation involves the use of a micro-lens array (or a pair of arrays), as demonstrated by Homburg [2].

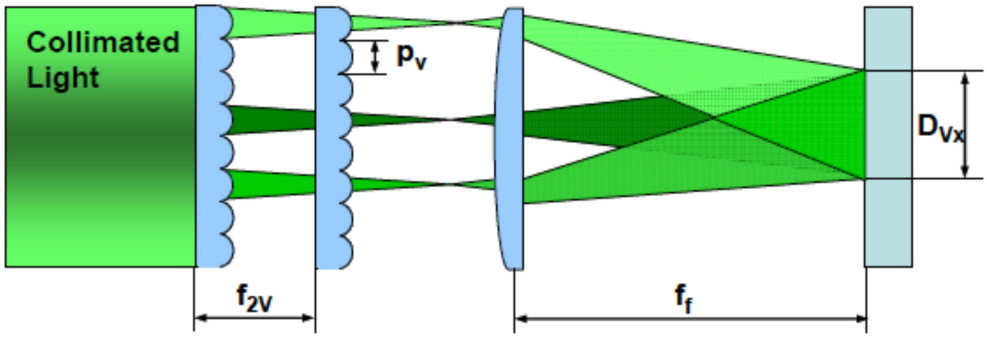

Figure 2.2: Schematic diagram of homogenisation of a laser beam (collimated light) by a pair of microlens arrays, as presented by Homburg [2]. Light blue components from left to right are; microlens array 1; microlens array 2; field lens; target plane.

The array consists of two 50-100 micron diameter (p_v) lenses, with a focal length specified by the divergence and beam size of the source to be homogenised. The lenses are most commonly cylindrical to provide homogenisation in only one axis, which is particularly applicable when dealing with diode stacks. The long axes of the cylindrical microlenses are oriented in parallel with the stripes of the diode stack beam. The first lens array focuses a segment of the beam, breaking the beam into a collection of smaller beamlets. These beamlets are then superimposed by the second imaging lens array to form a top-hat intensity profile. Excellent results have been reported with a top-hat beam profile being achieved using a pair of lens. One of the drawbacks of these systems is that the required parameters of the lens arrays are

specified by the parameters of the diode-array, therefore the lens arrays are not usually off the shelf and are expensive.

A more readily available product is engineered diffusers [3], an example of which is shown in Figure 2.3.

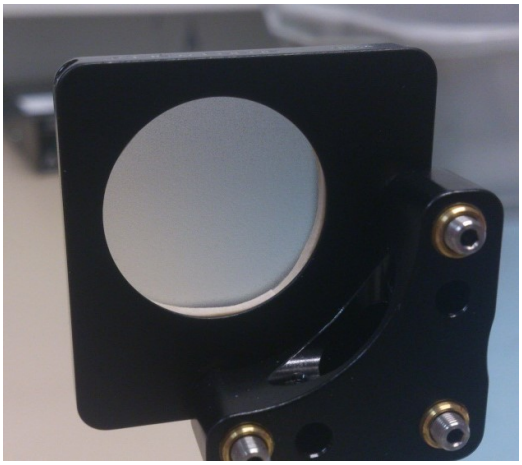

Figure 2.3: Photograph of *engineered* face of an engineered diffuser used in beam homogenisation experiment.

Engineered diffusers consist of a randomised array of microlenses formed on the surface of the optic, which in our case is plastic. This randomly distributes the transverse profile of a transmitted beam. The random nature of the lens array means that these "off-the-shelf" diffusers can be applied to any source, resulting in a top-hat beam profile with a divergence angle predetermined by the diffuser. These diffusers can achieve as high as 90 % transmission of the beam, which is considerably higher than conventional ground glass diffusers. They are primarily for use in solid-state lighting [3], and we have not encountered any literature detailing their use as diode stack homogenisers. This method of beam homogenisation is the one adopted in our experiments.

2.2 Experimental method and results

For this section, we measured the optical losses of the pump source due to the various components in our setup. Firstly, we describe a method of characterising the gain performance of our quasi constant-wave (QCW) laser using a modified Findlay-Clay analysis [4]. Following this, the results of the analysis are presented. The

addition of a diffuser to homogenise the pump beam, and its effects on QCW performance, are then explained.

Next we demonstrate passive Q-switching of our system using Cr:YAG crystals as a saturable absorber. The first set of results is presented, and the performance limitations discussed. Following this, the subsequent change in Q-switching performance, caused by the addition of a diffuser, was evaluated. We then postulate the presence of higher order transverse modes in our resonator, and their consequence to Q-switch performance.

2.2.1 QCW performance of a diode laser stack pumped Q-switched Nd:YAG laser

A schematic diagram and photograph of the resonator design, used in the QCW experiments, is presented below in Figure 2.4 and Figure 2.5, respectively.

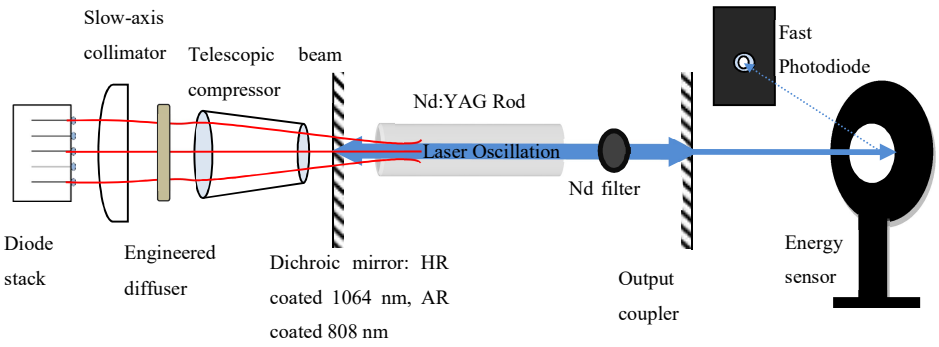

Figure 2.4: Schematic of resonator design. Pump beam in red, 1064 nm laser output in blue.

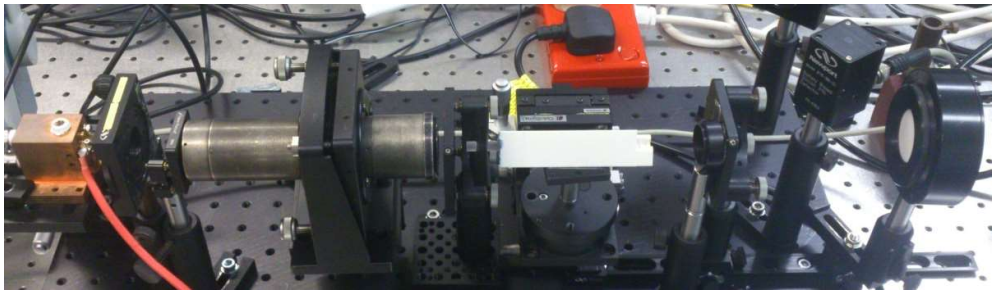

Figure 2.5: Photograph of resonator. The layout is equivalent to that of Figure 2.4.

2.2.1.1 Resonator components

This resonator contains a 6.25 mm diameter, 100 mm long Nd:YAG rod with an Nd concentration of 1.0 atm%. The first cavity mirror (on the left of Figure 2.4) is a high-reflectivity (HR) mirror with dual coatings to provide high-reflectivity at 1064 nm (laser-line), and anti-reflection (AR) at 808 nm to allow high transmission of the pump beam. The second cavity mirror (on the right of Figure 2.4) acts as the output coupler (R=30 to 70), with a coating which partially transmits the oscillating radiation (1064 nm). Also within the cavity is a mount for neutral density (ND) filters, the purpose of which is explained later (in section 2.2.2).

2.2.1.2 Pump delivery system efficiency

The diode pump source consists of 10 diode bars stacked, resulting in an emitter with a width and height of 10mm and 5 mm, respectively. The output power quoted by the manufacturer is 3kW. The stack has integrated fast-axis collimation (FAC) and a slow-axis collimator (SAC) lens spaced approximately 5 mm from the diode's output. The fast-axis remains collimated in the far-field, but the dimensions of the slow-axis comes to a waist within a few centimetres of exiting the SAC lens. In an attempt to homogenise the varying intensity in the fast-axis, an engineered diffuser is inserted before compression of the beam by a telescope. There are two choices of diffuser, defined by the full width divergence angle of the output. These, as quoted by the manufacturer, have either a 20 ° or 50 ° full divergence angle. Due to the beam being uncollimated at the entrance to the telescope, the output of the telescope is convergent. This allows the pump beam to be brought to a waist within the laser rod. The position of the pump beam waist, within the rod, can then be varied by moving the Nd:YAG rod towards or away from the telescope using a Vernier stage, thereby altering the total pumped volume within the laser rod itself.

Firstly, the diode pump source delivery optics were characterised at various intervals along the optical coupling system to assess the losses at each surface. At a fixed driver current, the diode energy transfer function was measured at the output of each optical component. The input energy to the diode was varied by changing the driver current pulse width. Using the forward biased voltage (quoted by the

manufacturer as 21.9 V) and the current (set at 240 A), the electrical energy supplied to the diode stack is calculated for each value of pulse width (Energy = Voltage x Current x Pulse width). The results are presented below.

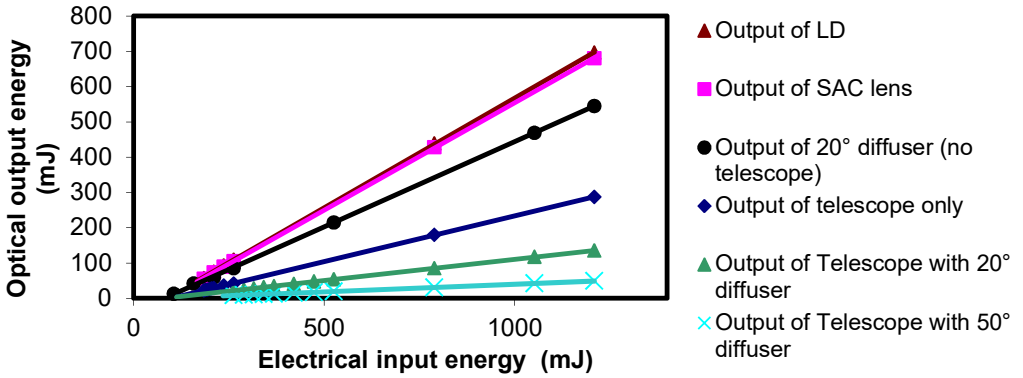

Figure 2.6: Energy transfer function of diode laser with different combinations of pump optics. LD denotes the emission of the laser diode with only integrated fast-axis collimation.

The percentage transmission of each combination of pump optics is presented in Table 2.1. The optical loss of the SAC lens is only 2 %, which is unsurprising due to the lens being AR coated to reduce reflections. The losses of the telescope are considerably higher, at around 58 %. The pump beam is not collimated in the slow-axis, which is required for efficient beam compression within the telescope. This, in addition to the telescope optics being uncoated, creates a large optical loss in the pump system. When used together with the diffuser (with 20° divergence), the energy transmission drops even further, resulting in a pump energy loss of 81 %. This is more pronounced with the 50 degree diffuser due to the divergence being greater, causing greater absorption at the walls of the telescope.

Table 2.1: Percentage transmission of various combinations of pump optics

Point of measurement	Percentage transmission
Output of SAC lens	98
20 degree diffuser only	77
Telescope only	42
Telescope + 20 degree diffuser	19
Telescope + 50 degree diffuser	7

A more efficient pump coupling system is required to increase the energy transferred to the gain medium. Regardless of this, we use this system to evaluate the effectiveness of engineered diffusers as a method of pump beam homogenisation, and how this affects QCW and Q-switched pulse energy.

2.2.2 Determining resonator gain & losses: a modified Findlay-Clay analysis

To analyse the resonator losses and gain values, a modified Findlay-Clay (F.C.) analysis [4] has been developed. This method involves not only changing the output coupler reflectivity, but also by introducing intra-cavity neutral density filters to add a further, known, loss into the cavity. This was needed to introduce sufficient loss to simulate the high cavity loss (low Q) scenario of Q-switching, by reaching higher gain whilst still operating in QCW (i.e. 1064 nm free-running) mode. This could, for example, potentially reveal the presence of any high-gain parasitic effects such as amplified spontaneous emission (ASE) [5] or parasitic lasing [6]. The modified F.C. analysis allows a much greater range of gain values to be measured with minimal re-alignment of the laser cavity. For each output coupler, many gain values can be measured. The theory behind the analysis is as follows [7]:

The conventional F.C. analysis begins by stating at the threshold of operation the laser gain exactly matches the cavity losses. Assuming that the HR mirror is close to 100 per cent reflective, the internal resonator losses are modelled in the following manner:

$$2g_0 l = \delta - \ln R_1, \qquad \text{Equation 2.1}$$

Where R_1 is the reflectivity of the output coupler; g_0 is the small signal gain coefficient of the material in m^{-1}; l is the length of the crystal in m; δ is the round trip internal losses due to, for example, scattering, absorption and reflections at interfaces other than the output coupler (including HR mirror).

To extend the F.C. analysis, we can add further, known, loss by introducing intracavity neutral density filters. Since the filters are inside the cavity, the beam passes through them twice in a round trip. This means that the beam experiences a

transmission coefficient of T^2, where T is the transmission of the neutral density filter. Hence, Equation 2.1 is modified as shown below:

$$2g_0 l = \delta - \ln(R_1 T^2), \qquad \text{Equation 2.2}$$

Experimentally, the value of R (Equation 2.2) is varied by changing the output coupler reflectivity, and T is altered by swapping neutral density filters. To find an equation for the losses in terms of the threshold pump pulse energy we can substitute the relationship $2g_0 l = E_{\text{th}} K$ into Equation 2.2 as follows [7]:

$$-\ln(R_1 T^2) = E_{\text{th}} K - \delta, \qquad \text{Equation 2.3}$$

Where K is a constant that arises from the small signal gain being proportional to the pump energy at threshold. Therefore if $-\ln(R_1 T^2)$ is plotted against E_{th}, the gradient of the line will be equal to $\frac{2g_0 l}{E_{\text{th}}}$. The logarithmic roundtrip small-signal gain ($2g_0 l$) can therefore be calculated for each value of E_{th}. The small-signal gain coefficient (g_0) refers to the gain per unit length of the material at a certain pump energy prior to the gain becoming saturated by stimulated emission. Consequently, the resonating intensity increases by a factor of $\exp(g_0 l)$ after each pass.

To summarise, the natural log of the useful (output coupling plus ND-filters) round-trip loss is plotted against the threshold pump energy. The internal losses (parasitic/non-useful) of the resonator are found by extrapolating the line to the point where it meets the y-axis (Figure 2.7). We measure the threshold pump energy by increasing the pump pulse duration from zero until the first laser output is detected by a Silicon fast-photodiode.

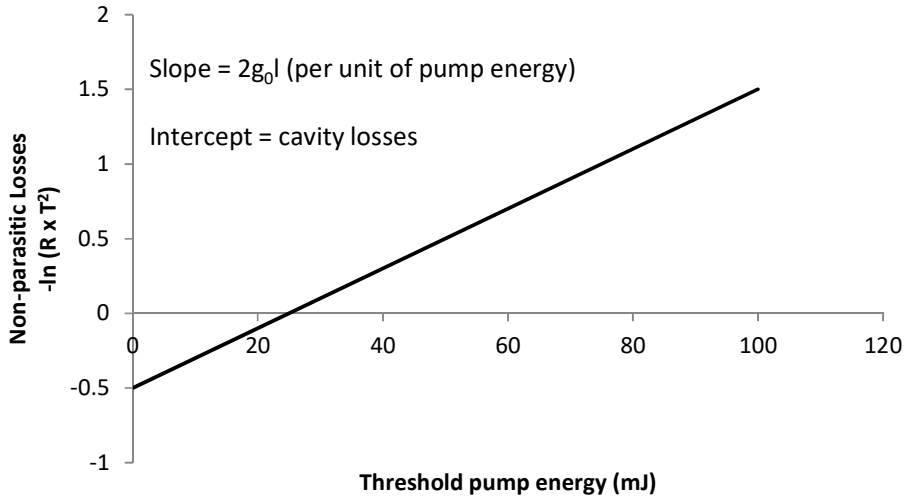

Figure 2.7: Example of graph produced by the modified Findlay-Clay analysis.

2.2.2.1 QCW gain measurements

Firstly, a standard Findlay-Clay analysis was carried out, without the addition of neutral density filters, both with and without the use of a diffuser. The pump pulse duration was varied, rather than diode current, to preserve the shape of the current pulse applied to the diode. When the diode current was adjusted, we observed that the shape of the current pulse became deformed, and therefore the amount of energy supplied to the diode inaccurate, when the current was set low. The pump energy, incident on the rod, is derived from the transmission data in Table 2.1 and the diode energy data used to plot Figure 2.6. The results are presented below in Figure 2.8.

The internal losses extracted from the intercepts of each graph are 1.1 $\pm$ 4.7 % and 1.2 $\pm$ 7.7 % per round trip, with and without a diffuser, respectively. This is consistent with the loss associated with the 6 optical surfaces (per round trip) in the resonator, approximating 0.2 % optical loss per AR/HR coated surface yields a total loss of 1.2 %. The errors in the losses are the standard error of the intercept from the linear regression. We are confident to use these values of internal loss in later analysis due to the values being very similar (1.1 and 1.2 %), even with the relatively large standard errors. The logarithmic small-signal round trip gain ($2g_0l$) per unit of energy, extracted from the graphs (gradient of line), are $0.0479 \pm 3.17\text{x}10^{-3}$ mJ^{-1} and

$0.1287 \pm 1.38\text{x}10^{-2}$ mJ^{-1}, with and without the diffuser, respectively. The error in the gain is the standard error of the gradient in the linear regression. The modified Findlay-Clay analysis (using additional ND filters) was carried out both with and without the use of a diffuser to assess high gain QCW performance.

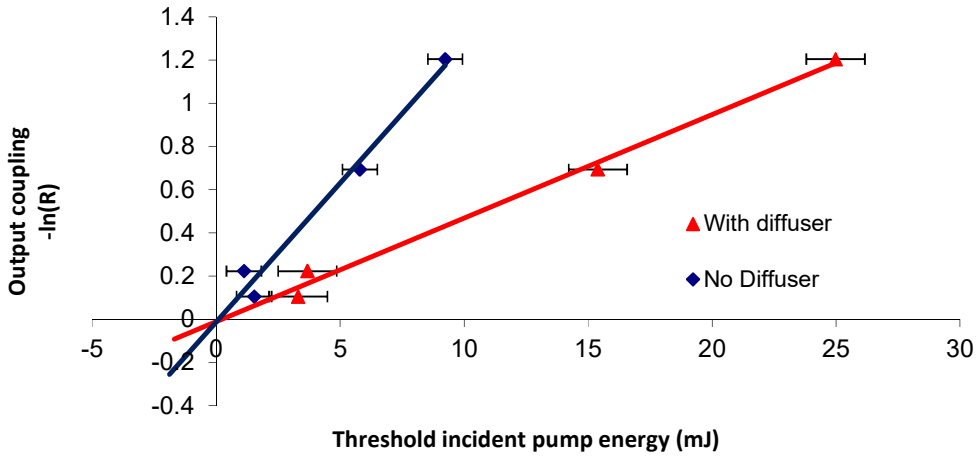

Figure 2.8: Standard Findlay-Clay analysis of resonator with and without homogenised pump beam. A telescope was used in both cases to compress the beam

The transmission of the filters were measured using a separate 1064 nm laser, to provide a comparison with manufacturers quoted values. The intercept values extracted from the standard analysis (1.1% and 1.2%) were used to plot the graphs for the modified analysis (Figure 2.9 shown below), by forcing the intercepts to these values. This was necessary since not doing so resulted in the y-intercept being positive (implying negative losses), due to the larger error in the data points when using the ND filters.

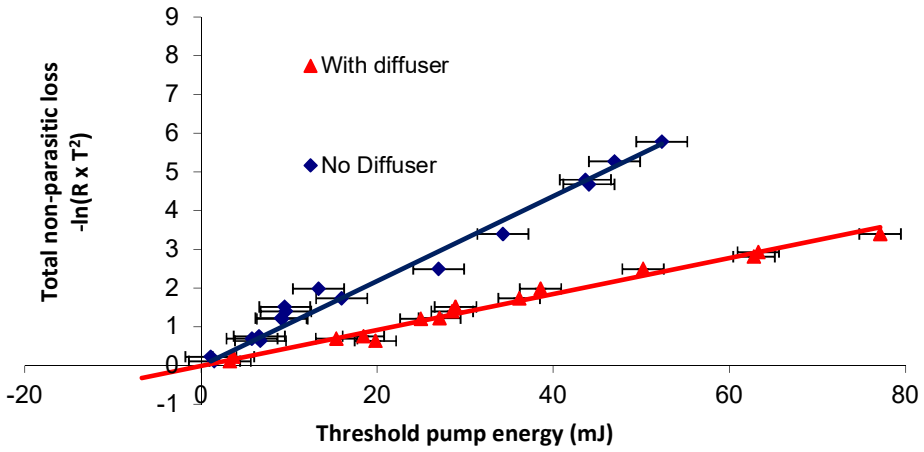

Figure 2.9: Modified Findlay-Clay analysis using ND filters, with and without homogenised pump beam. A telescope was used in both cases to compress the beam

The resulting logarithmic small-signal round-trip gain values (per unit of energy) are $0.0464 \pm 1.68\text{x}10^{-3}$ mJ^{-1} and $0.1095 \pm 3.56\text{x}10^{-3}$ mJ^{-1}, with and without the diffuser, respectively. The relevance of these values is that they allow a prediction of the Q-switch performance, which occurs at much higher gain than normal QCW mode operation (with no ND filters). We can now determine the maximum values of R and T (T now being the initial transmission of the Q-switch) that the system will operate with, according to the available pump energy. The fact that the curves remain linear, suggests that the gain medium is operating reliably (i.e. in the absence of ASE/parasitic lasing effects).

The gain reached without the diffuser is 2.4 times greater than the value obtained using the diffuser. It was expected that the gain (the slope of each graph) would be similar in both cases, since the pump losses had been taken into account during the analysis. The discrepancy can be explained in terms of the difference in pump spatial beam profile. As we will see in the next section, the unhomogenised beam has *hot spots* of very high pump power, and hence gain. As we are only measuring the threshold point, it is the higher gain regions which lase first that will be recorded. The average gain however, (across the whole material) includes low gain regions which do not lase, will be lower. The homogenised pump beam conversely, has no hot spots and therefore the gain will be more uniform. This leads

to a higher threshold point, corresponding to a lower gain value per unit of pump energy, being extracted from the analysis. The result is that the gain value for the homogeneous pump beam is far more representative of the average level of the pump than with the unhomogeneous beam.

2.2.3 Effects of pump beam homogenisation on QCW output

As stated in the previous section, the results of the F.C. analysis suggests a spatially spikey gain profile for the unhomogenised beam. This is confirmed below.

2.2.3.1 Spatial beam profiles

The spatial profiles of the pump and QCW laser output beams, both with and without the diffuser, are presented in Figure 2.10.

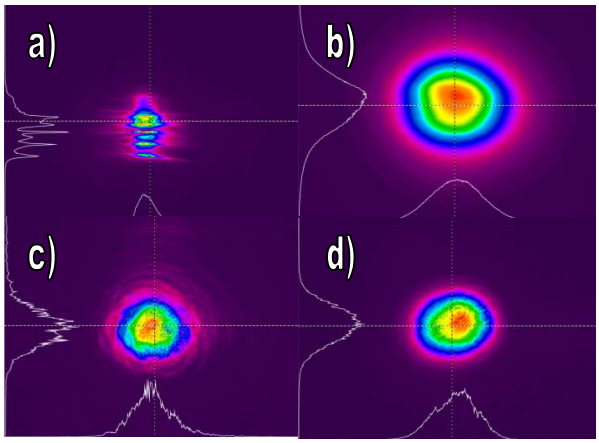

Figure 2.10: Images of transverse profile of a) pump beam without diffuser, b) pump beam with 20° diffuser, c) QCW laser output beam without diffuser, d) QCW laser output beam with diffuser. Note: pump spots appear to be different sizes due to the positioning of the camera, they are approximately equal in size at when entering the laser rod (6 mm diameter). a) and b) were captured at the output of the telescope, c) and d) were captured approximately 10 cm from the output coupler.

The image of the unhomogenised pump (a) shows a smooth Gaussian-type profile in the x-axis, and a spikey profile in the y-axis. When this beam is coupled into the Nd:YAG resonator, the result is a spikey (in the y-axis) QCW beam (c). When the diffuser is inserted in front of the diode-laser beam (as in Figure 2.4), the resulting pump beam (b) has a considerably smoother, more Gaussian-like profile. This translates to a correspondingly smoother QCW output beam that is more Gaussian-

like in both axes, than that obtained without the diffuser. A reasonable explanation for this smoothed Gaussian beam is that the more uniform pump allows a more uniform transverse mode profile in the QCW beam.

2.2.3.2 Energy transfer functions

Figure 2.11 shows the effective energy transfer function (i.e. QCW energy against pump duration) of the laser for QCW mode, with and without a diffuser. The pump energy was varied by changing the pulse duration, and therefore, since only a qualitative analysis is required, the pulse width (at fixed current) is plotted on the x-axis.

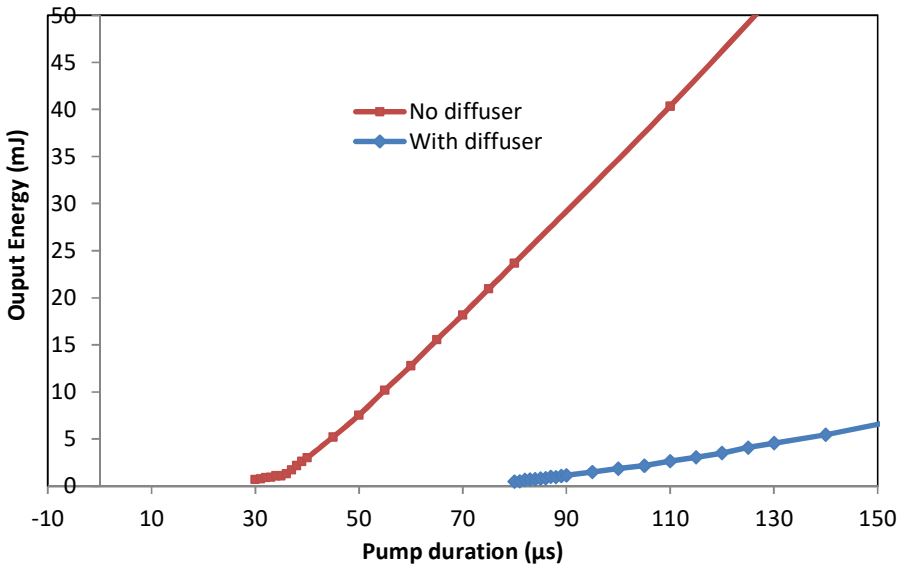

Figure 2.11: Effective energy transfer function of QCW operation, with and without diffuser. 30% reflectivity output coupler was used. The red and blue lines are not linear fits.

Without the use of a diffuser, the line is non-linear close to threshold. However, when the diffuser is inserted, the curve appears to be quasi-linear. This again can be explained by the transverse mode structure of the beam. When the diode pump is operated without the diffuser, the QCW beam is likely to be composed of widely spaced higher order modes, all with similarly widely separated threshold values. This would cause a non-linear increase in output energy as the pump duration is increased. When the diffuser is inserted, the pump beam will be more homogeneous and the resulting QCW mode threshold points of any higher order modes will be closer

together. This ensures that the transfer function curve is linear, even down to low pump durations. The output energy however, is severely diminished by the diffuser, due to the high losses of the pump beam optical system. We can now evaluate how this will affect the Q-switched performance.

2.2.4 Q-switching performance

In this section we describe the Q-switch performance with and without the engineered diffuser. The experimental setup is similar to that used for QCW mode, except that Cr:YAG saturable absorbers are added to the cavity to generate Q-switched pulses.

2.2.4.1 Q-switching with no engineered diffuser

Previous attempts we have made at Q-switching our Nd:YAG laser with Cr:YAG saturable absorbers have resulted in low energy pulses (≈1 mJ). This was due to high intensity pump regions reaching threshold significantly before the rest of the pumped regions, as a result of the stripy pump beam. The apparatus used is presented below Figure 2.12.

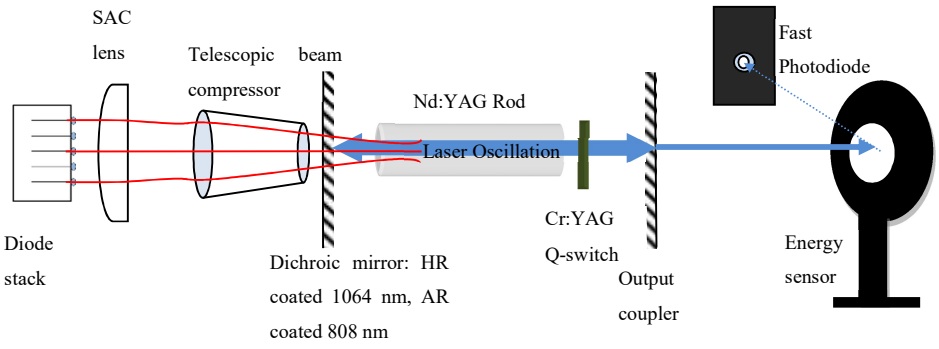

Figure 2.12: Schematic of apparatus used during original, low energy, Q-switching experiments. Setup is equivalent to that of Figure 2.4, but with a Cr:YAG Q-switch replacing the ND filter.

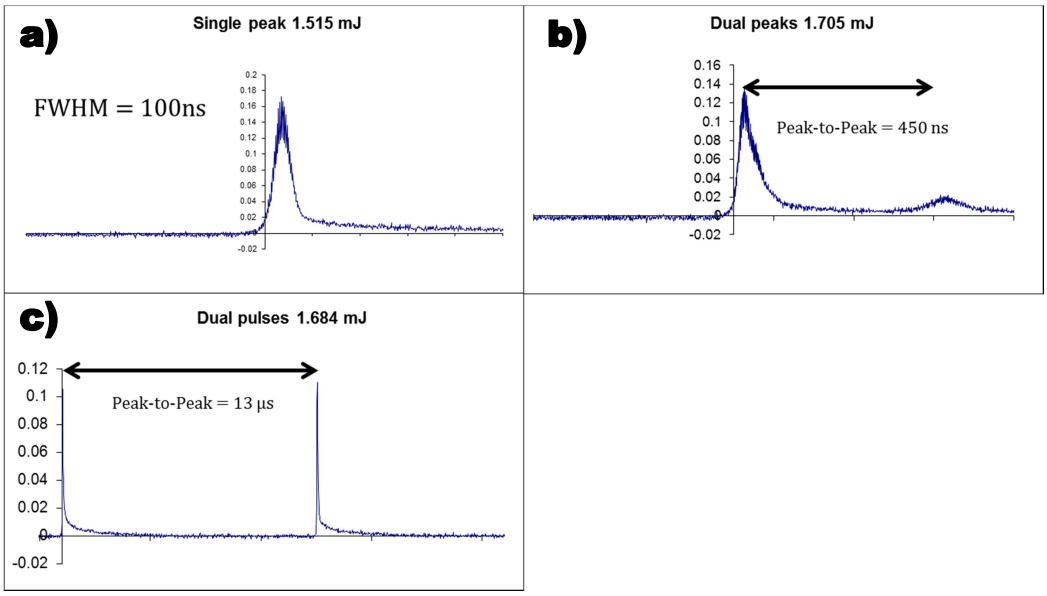

Figure 2.13: Oscilloscope traces of a) a single Q-switched pulse, b) a single pulse with intermittently occurring secondary (closely spaced) peak with varying pulse separation, c) dual pulse production with constant (greater) pulse separation

In the Q-switching experiments, the diode pump duration was adjusted until a single, typical, Q-switched pulse was emitted. An example is presented in Figure 2.13a). This is the ideal scenario. However, it proved difficult to generate a single, high quality Q-switched pulse. More often the pulse was followed by a closely spaced satellite pulse (as seen in Figure 2.13b)), which was observed to move in time relative to the main pulse. We believe that this behaviour is a result of mode competition, which we have postulated previously to explain the shape of the energy transfer function in Figure 2.11. This will be handled in greater depth in chapter 3, where we assess the temporal effects found in Q-switched pulses. A similar Q-switched satellite is also observed by Lee et al [8]. The small, but not insignificant spatial and temporal separation of these pulses would lead to non-ideal performance for designation.

The spatial profile of each pulse was also non-ideal (non-Gaussian) as depicted below in Figure 2.14. This again is evidence for a non-uniform transverse mode profile in the Q-switched beam.

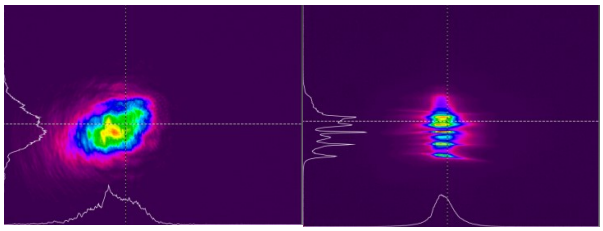

Figure 2.14: Beam images of Q-switched pulse (left) pumped by unhomogenised diode laser (right).

The production of dual pulses, illustrated in Figure 2.13c), is an entirely separate process which was observed when the pump duration was significantly increased. We expect multiple Q-switch pulses to be observed, separated by 10's of μs as presented in Figure 2.13c), which is equivalent to a repetitively Q-switched pulse train [9]. In this circumstance, the Q-switched pulses are spatially equivalent. Here the emission of a pulse depletes the gain, which then requires a certain time to recover (provided the pump duration is long enough). Once the gain recovers, a second pulse is emitted with the same spatial properties as the first.

2.2.4.2 Effects of pump beam homogenisation on Q-switching performance

In this section we will assess how pump beam homogenisation can improve Q-switched performance. We start by looking at the spatial profile of each beam.

Presented below, in Figure 2.15, are the beam images captured under different pumping and cavity configurations with and without diffusers. The first thing to notice is the poor spatial profile of the unhomogenised pump beam (Figure a)), and the effect it has on the spatial profiles of both the QCW beam (Figure b)) and the Q-switched beam (Figure c)). In the case of the Q-switched beam, the inhomogeneous pump beam excites only a small strip (or stripes) of the rod with sufficient gain to initiate Q-switching. This results in a non-Gaussian beam profile. The QCW beam appears more Gaussian in shape, but with several sharp peaks, consistent with the striped pump beam.

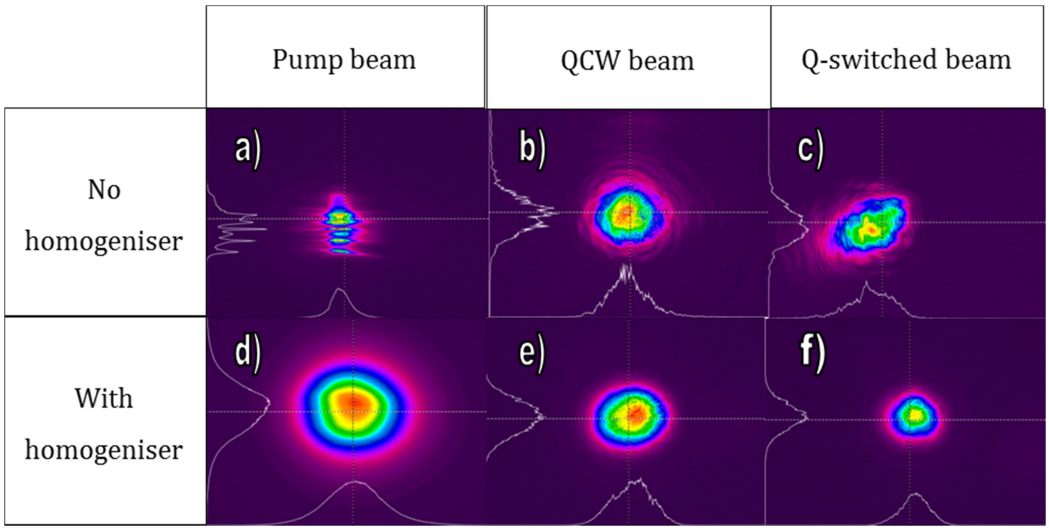

Figure 2.15: beam images captured at various stages along the laser, a) pump beam at output of telescope b) QCW output, c) Q-switched output, d) diffuser-homogenised pump beam at output of telescope e) QCW output with diffuser-homogenised pump beam, f) Q-switched output with diffuser homogenised pump beam.

Now comparing the pump beam images, with and without the employment of the diffuser (Figure d) and a) respectively), it is immediately apparent that the profile of the beam has been substantially improved by the diffuser. Although not transformed into a top-hat profile, as quoted by the manufacturer, it is considerably more homogeneous than without the diffuser. As a result, the QCW beam (Figure e)) has a smoother profile (compared to Figure (b)) and the Q-switched beam (Figure f)), is significantly more uniform (Figure c)).

Now we will consider how the Q-switched single pulse energy is improved by pump beam homogenisation. Figure 2.16 shows the dependence of single Q-switched pulse energy on the round trip loss of the resonator, for both systems with and without the diffuser and telescope (i.e. only the SAC lens coupling the pump beam into the rod). The pump beams are approximately equal in diameter in both scenarios.

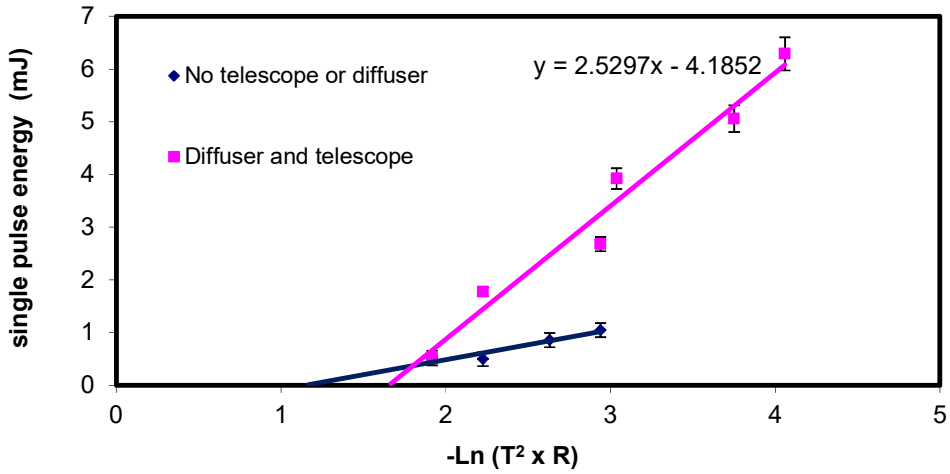

Figure 2.16: Single Q-switched pulse output energy as a function of the non-parasitic loss (T and R), measured with and without a diffuser and telescope coupled pump beam. Displayed errors are the standard error of the regression (straight line) analysis.

The resonator losses (gain) were varied by changing the initial transmission of the saturable absorber, whilst keeping the output coupler constant at 30 percent reflectivity. As expected the Q-switched pulse energy increases as the unsaturated transmission of the saturable absorber decreases. This is due to greater energy storage before a pulse is released (i.e. greater *hold-off*). The resulting energies are greatly improved (more than double) when a telescope and diffuser are used to couple the pump beam into the rod, despite the 81 % loss of pump energy introduced by these components (see Table 2.1). This again highlights that a more uniform, lower intensity pump beam is better suited for pumping a Q-switched system.

2.3 Optimised pump optics for efficient Q-switching

Up until now the pump optics were not optimised for transmission, and the experiments were to prove the principal that pump homogenisation with an engineered diffuser would increase Q-switched pulse energy. In this section we present a pump scheme with improved pump transmission which allows us to reach even higher Q-switched pulse energies. Firstly, this includes an engineered diffused to homogenise the pump beam. Secondly, a large aperture condenser lens is used to collect and focus the homogenised pump beam. Thirdly, the beam is focused onto a much larger 10 mm diameter Nd:YAG rod, allowing a much larger volume of the rod to be energised by the pump beam. Below is a schematic and photograph of the laser apparatus.

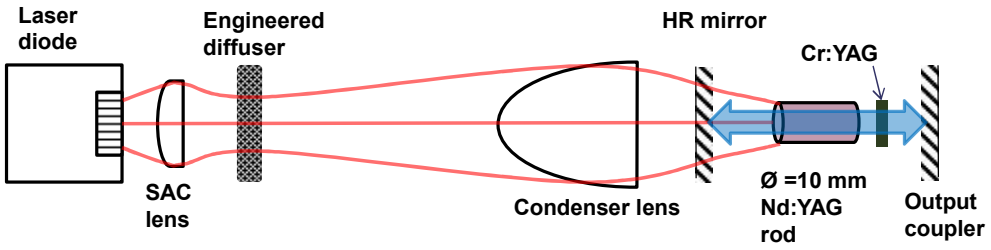

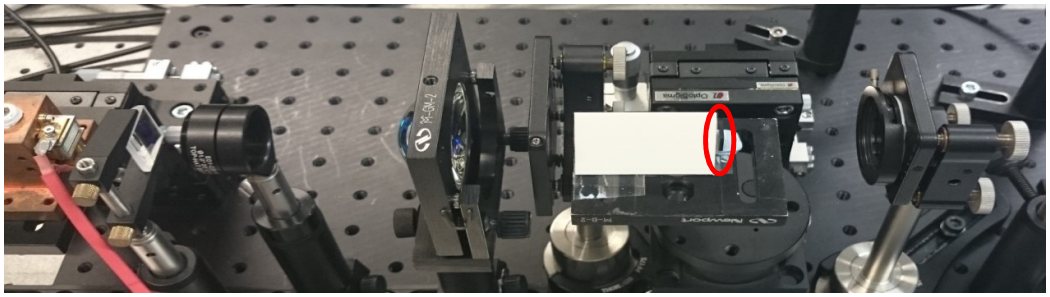

Figure 2.17: Schematic and photograph of laser apparatus with improved pump system. The Cr:YAG Q-switch crystal is placed in the centre of the resonator, and is highlighted in a red circle in the photograph. The Nd:YAG laser rod is encased in a white plastic mount.

As evidence for the improvement in the laser setup, we present the single pulse energy measured over 500 shots shown in Figure 2.18. The average single pulse energy over 500 pulses is measured to be 53.4 $\pm$ 1.53 mJ, which represents a considerable improvement on the previous results. This system will be the basis of our investigations into timing jitter and passive Q-switch materials in the following chapters.

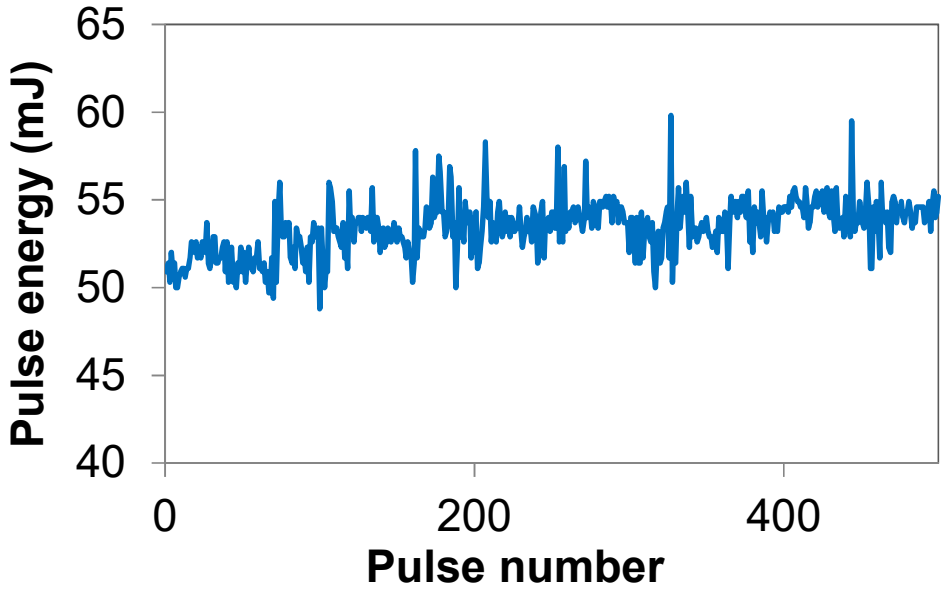

Figure 2.18: Single pulse energy measured over 500 shots. The average pulse energy is 53.4 ± 1.53 mJ.

2.4 Discussion and Conclusions

The current system presented in this report, although not fully optimised, shows promising results for passive Q-switching of Nd:YAG. In an attempt to improve the spatial profile of the pump beam, homogenisation was carried out using an engineered diffuser coupled into the rod by a telescope. The QCW performance of the laser was assessed using a modified Findlay-Clay analysis designed to model high gain. From this analysis, the internal losses of the resonator were calculated to be around 1.1% and 1.2 %, with and without the diffuser, respectively. This was close to the expected results based on the residual reflection losses of the optical elements. We believe this is the first time this type of analysis has been performed to simulate the high gain regime of a passively Q-switched system.

The effects of improving the pump beam on Q-switching performance were also investigated. The Q-switch energy obtained was more than 2 times greater with homogenisation compared to the unhomogenised beam, for the same cavity loss and *hold-off*. Whilst the resulting beam was considerably more uniform and higher energy than without the diffuser, the losses introduced into the pump system were

large. This meant the Q-switched energy was limited, as low initial transmission saturable absorbers could not be used. For this reason, the pump coupling scheme was improved using a single AR-coated collimating lens in place of the telescope to increase the energy transmission. With this improvement, together with a larger (1cm diameter) Nd:YAG laser rod and Cr:YAG crystal (1 cm diameter), we have achieved a significantly higher single Q-switched pulse energy. The resulting average energy was measured to be 53.4 mJ which is within the energy specification set out in the STANAG (> 50 mJ) [10]. We believe, this is the highest reported single pulse energy achieved with an end-pumped passively Q-switched Nd:YAG laser. We reported these results at a number of conferences [11][12]. It is worth noting that the energy is required to be maintained above 50 mJ during a pulse train, which is not achieved in Figure 2.18. This is likely to become a more prominent issue during temperature testing, since the energy is expected to drop even further. It is for this reason that further improvement of the pulse energy would be required in future experiments.

2.5 References

[1] M. Traub, H.-D. Hoffmann, H.-D. Plum, K. Wieching, P. Loosen, and R. Poprawe, “Homogenization of high power diode laser beams for pumping and direct applications,” *Proc. SPIE*, vol. 6104, p. 61040Q–61040Q–10, 2006.

[2] O. Homburg, A. Bayer, T. Mitra, J. Meinschien, and L. Aschke, “Beam shaping of high power diode lasers benefits from asymmetrical refractive micro-lens arrays,” *Proc. SPIE*, vol. 6876, p. 68760B–68760B–7, 2008.

[3] G. Morris and T. Sales, “Engineered diffusers^{TM} for display and illumination systems: Design, fabrication, and applications,” 2007.

[4] D. Findlay and R. A. Clay, “The measurement of internal losses in 4-level lasers,” *Phys. Lett.*, vol. 20, no. 3, pp. 277–278, 1966.

[5] G. Haag, M. Munz, and G. Marowsky, “Amplified Spontaneous Emission (ASE) in Laser Oscillators and Amplifiers,” *IEEE J. Quantum Electron.*, vol. 19, no. 6, pp. 1149–1160, 1983.

[6] Y. J. Huang, P. Y. Chiang, H. C. Liang, K. W. Su, and Y. F. Chen, “Efficient high-power UV laser generated by an optimized flat-flat actively Q-switched

laser with extra-cavity harmonic generations," *Opt. Commun.*, vol. 285, no. 1, pp. 59–63, 2012.

[7] W. Koechner, *Solid-State Laser Engineering*. New York: Springer, 2006.

[8] K. Lee, H. C. Lee, J. Cho, J. Lee, and J. Yi, "Optics & Laser Technology Passively Q-switched , high peak power Nd : YAG laser pumped by QCW diode laser," *Opt. Laser Technol.*, vol. 44, no. 7, pp. 2053–2057, 2012.

[9] J. Dong, "Numerical modeling of CW-pumped repetitively passively Q-switched Yb:YAG lasers with Cr:YAG as saturable absorber," *Opt. Commun.*, vol. 226, no. 1–6, pp. 337–344, 2003.

[10] *Standardized Agreement 3733*, 2nd ed. North Atlantic Treaty Organisation, 2005.

[11] M. W. Smillie, M. Silver, S. T. Lee, and T. J. Cook, "High single-pulse energy, passively Q-switched Nd:YAG laser for defence applications," *Proc. SPIE*, vol. 8959, p. 89590Z, 2014.

[12] M. W. Smillie, M. Silver, and S. T. Lee, "Passive Q-switch materials for diode pumped Nd:YAG laser systems," in *Proceedings of the 2013 High Power Diode Lasers and Systems Conference, HPD 2013 - Co-located with Photonex 2013*, 2013, pp. 26–27.

Chapter 3 Investigation into the potential jitter mechanisms present in a high single pulse energy passively Q-switched laser

3.1 Introduction

In this chapter we investigate the mechanism of timing jitter in a passively Q-switched system. We will first examine why it is an important parameter when considering an application in laser target designation. Then we explore the literature detailing the reasons for, and the solutions to, timing jitter. Finally we will attempt to establish, experimentally and theoretically, which mechanisms we believe to be prevalent in our particular system.

3.1.1 Timing jitter

It is first important to define what timing jitter is for our application. The pulse-to-pulse timing jitter is defined as the time deviation of any given pulse relative to a predefined pulse train period. More specifically, the pulse train is set to have a certain time period between pulses, in our case 500 ms (2Hz). The jitter value would be the maximum value by which any given pulse-to-pulse period deviates from this 500 ms value. The notation used is therefore *Period* ± *Jitter*, being plus or minus due to the pulse being able to be detected either late or early relative to the defined period. This is distinct from other definitions of jitter, which are measured relative to the pump pulse.

3.1.2 Importance of jitter for applications in designation

For the application of laser designation, the pulse-to-pulse timing jitter is a crucial parameter. It is stipulated in a NATO standardised agreement (STANAG 3733 [1]) that it must be within ± 5 μs. This is to ensure that the precision of each pulse train is sufficient to allow detection of the intended encoded frequency.

A particular repetition frequency code, is selected for a given day, to ensure that enemy forces cannot interfere with the designation process. The choice of codes consists of a list of repetition frequencies at around 20 Hz, the details of which are confidential. An example of two possible codes is presented below in Figure 3.1, which shows the difference in pulse repetition period of a 20.0 Hz and 20.1 Hz code.

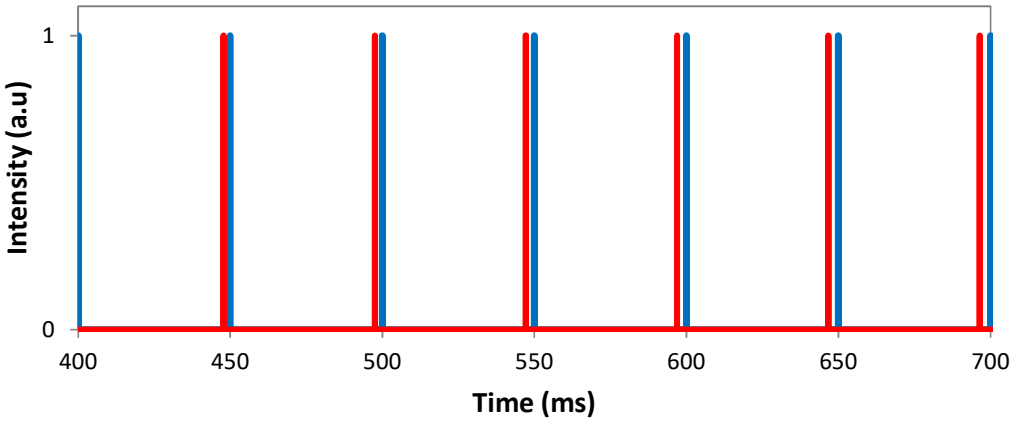

Figure 3.1: Diagram illustrating the difference between two designator codes, 20.0 Hz (blue) and 20.1 Hz (red). The pulse repetition period of the 20.0 Hz (blue) is 50 ms and the 20.1 Hz (red) is 50.1 ms.

The difference in pulse period between the 20.1 Hz and 20 Hz code is 100 µs, any significant error (i.e. above $\pm$ 5 µs jitter) in the period could prevent the seeker from resolving the correct designator frequency code. It is for this reason that the jitter is defined as the maximum value, rather than a standard deviation value. In actively Q-switched systems, precise control of the switch itself means that the jitter is small enough not to be problematic. Passive Q-switching, however, does not allow such precise control of the switching time [2]. The specific physical mechanisms behind timing jitter are explained in the following section.

3.1.3 Potential jitter mechanisms in passive Q-switching

There are two main aspects to the jitter investigation. Firstly a reliable jitter measurement method is required. The method we have used is described in section 3.3.2. Secondly, the causes of jitter need to be assessed, either experimentally or theoretically. This involves quantifying the contribution of each mechanism towards the total jitter in the system. The potential mechanisms are described below.

3.1.3.1 Mechanical vibrations

Mechanical instability of the resonator mirrors can create pulse timing fluctuations through a variation in cavity losses. At the optimised mirror alignment, the cavity losses should be at a minimum. Conversely, when the mirrors are perturbed from an optimised configuration, by airflow or vibrations for example, the losses will increase. This will alter the build-up time of the pulse by a duration related to the change in the round-trip losses of the cavity. If the round-trip gain varies between pulses, this introduces timing jitter. This is similar to the mechanism of pump power fluctuations described below in the following section.

3.1.3.2 Pump power fluctuations

It has been reported that variations in the pump power will lead to increased timing jitter [3][4]. These systems are based on repetitive Q-switching rather than a QCW (Quasi Continuous Wave) pumped system such as ours. An explanation of the process which we believe to be affecting the jitter is as follows.

We are QCW pumping the system to reduce thermal loading of the Nd:YAG rod. The rod is pumped for a period less than the fluorescence lifetime of Nd:YAG (230 μs), at a repetition rate of 2 Hz. The pulse-to-pulse period of our pump system (500 ms) is considerably greater than the upper laser level lifetime of Nd:YAG, which means that pump power fluctuations do not affect the Q-switched repetition rate. This is unlike other systems which are repetitively Q-switched using a CW pumping scheme. In our study we have modelled how pump power fluctuations affect timing jitter, using an approximation of pump fluctuations based on real measurements.

Figure 3.2 provides an illustration as to how pump power affects the timing jitter in our system.

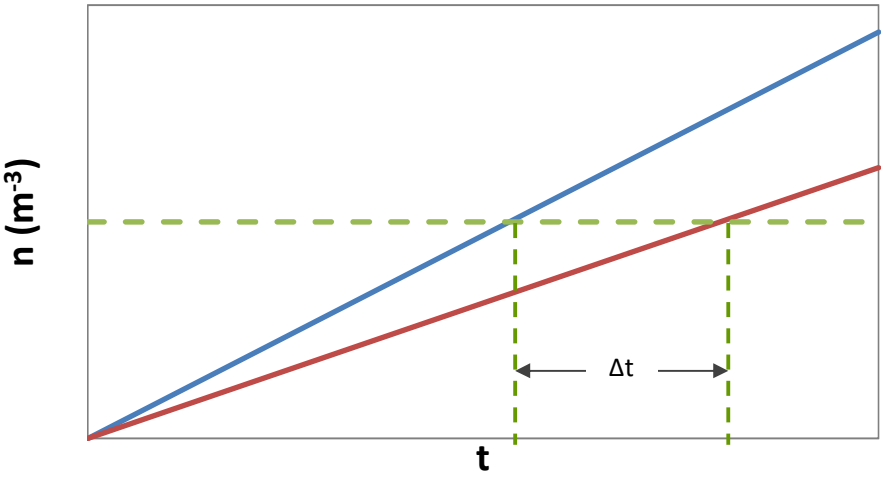

Figure 3.2: Diagram of population inversion density (n) versus time to illustrate how pump power fluctuations contribute to timing jitter. Blue line has higher pump power than the red line. Horizontal green dashed line represents threshold inversion level of laser. The jitter is the resulting timing difference between the blue and red lines reaching the threshold point, shown on the graph as Δt.

During a single pump cycle, any fluctuation in the pump power will lead to a direct variation in the total pump energy delivered to the gain medium. If the pump energy drops, the system will take longer to reach threshold than if it were higher. This would result in the delayed emission of the Q-switched pulse, relative to the start of the pump pulse. The pulse would be emitted somewhat earlier if the pump energy increases. The net effect of this would be fluctuations in the Q-switched pulse timing relative to the start of each pump cycle. If the red line represents a low pump power and the blue a relatively higher pump power, we can see that the blue line reaches threshold, as represented by the green dashed line, first. This would result in fluctuations in the Q-switched pulse timing relative to previous and following pulses. Our investigation of pump fluctuations is described in section 3.2.3.

3.1.3.3 Spontaneous emission noise

The most commonly reported mechanism responsible for timing jitter is the uncertainty in the build-up of the laser emission from noise. This is commonly referred to as spontaneous emission noise [5]. The basic principle relies on the fact that the fluorescence (i.e. spontaneous emission) of the laser gain medium is a random process. The resonating intensity is required to be sufficiently high to bleach the saturable absorber, which is dependent on the moment that the amplified spontaneous emission reaches a sufficient level. Due to the random nature of this process, an uncertainty in the switching time of the absorber is introduced.

The values of jitter attributed to spontaneous emission noise tend to be in the tens of nanosecond in a passively Q-switched system. Although the systems reported [3] [6] are of considerably higher repetition rate (kHz compared with our Hz), we believe that the contribution of spontaneous emission noise jitter would still be in the nanosecond range. We have carried out modelling of this noise to justify this hypothesis, which can be found in Section 3.2.2.

3.1.3.4 Satellite pulses (mode competition)

It has been cited [7] that jitter can be a product of other temporal instabilities, in this case satellite pulses. There are two relevant mechanisms involved: firstly, how the satellite pulse is formed, and secondly, how this affects timing jitter. The mechanism by which satellite pulses are formed is as follows. If two modes (transverse or longitudinal) have different threshold gain values, then they will begin to oscillate at different times, resulting in two distinct pulses separated in time. In essence, the lifetime of Cr:YAG is sufficiently long (4 μs) that the primary mode with the highest gain bleaches the Q-switch, which remains open, thus allowing the mode with the second highest gain to reach threshold. The two modes will share some portion of the gain region, which will be partially depleted when the primary pulse begins to oscillate. The primary pulse has now been produced and its gain region pushed well below threshold. With continued pumping of the gain material, the gain region shared by the two modes will increase to a level allowing the secondary mode to reach threshold and oscillate shortly after the main pulse.

The mechanism by which mode competition affects the pulse-to-pulse timing jitter is as follows. Considering first, two competing transverse modes, the fundamental TEM_{00} and any higher order mode. Both modes will have a different spatial gain distribution, but will overlap in certain points. It is at these points of overlap where the competition will arise. Here the presence of a secondary mode will cause a portion of the fundamental mode to experience diminished gain. The system will now require additional pump energy (pump time) to reach threshold. Since the competition of these modes is unstable, the additional time for the pulse to be produced will vary, thus leading to timing jitter between pulses [8][9]. This description of mode competition jitter is applicable to longitudinal modes, with satellite pulses being attributed to spatial hole burning within the gain medium [10].

In terms of what is observed, the pulse train is characterised by the primary pulse, within which the majority of the energy is contained, being closely followed by a much smaller pulse. The period between the main and satellite pulse is typically of the order of tens of nanoseconds in our laser, ruling out that possibility as a significant factor in the microsecond jitter regime. We have conducted some experiments to confirm that this is the case, which can be found later in section 3.3.6.1.

3.1.4 Jitter reduction methods

In this section we will outline some of the jitter reduction techniques described in the literature. It should be noted that the laser systems described in this literature are all of a much higher repetition rate and lower energy than our system. Consequently, spontaneous emission noise is cited as the main cause of timing jitter in these systems. The following laser systems all use diode end pumped Nd:YAG with a Cr:YAG saturable absorber.

3.1.4.1 Composite pump pulse

One jitter solution is based on a composite pump pulse consisting of a steady pump power for most of the duration of the pump time, which is followed immediately by a sharply increased pump power for a short time at the end. Such a design has been reported by [3] Khurgin et. al, in which the timing jitter of a passively Q-switched

laser was reduced from 6 to 0.5 µs. The system was similar to ours in that it has a diode pumped Nd:YAG crystal, passively Q-switched using Cr:YAG. The most significant difference is that this is a very low energy system, using only 2 laser diodes driven at 1 A, compared with our 10 bar stack which is driven at 240 A. The current of 1 A was applied to the first diode and 4 A applied to the second diode to provide the instantaneous surge of pump power. The laser was repetitively Q-switched with a resulting pulse separation of 0.36 ms. Whilst they saw a significant reduction in timing jitter; this technique may not be viable in our configuration as we are already running the diode stack at full power, with no scope to immediately increase the power during pumping. It would also greatly complicate the design and cost of our system, even if possible.

3.1.4.2 Combined active and passive Q-switch

Another novel concept of jitter reduction as reported by [6] Wang and Xu, involves the use of both active and passive Q-switching simultaneously. The laser system has an Nd:YAG gain medium codoped with Cr:YAG with an initial transmission of 75.5 %, to act as the saturable absorber. There is also an acousto-optic modulator (AOM) to act as the active Q-switch. The cavity loss is held high until the AOM is switched to the low loss state, allowing the gain to drop partially, thus emitting an appreciable number of cavity photons to bleach the saturable absorber. At this point the Q-switched pulse is emitted. The active Q-switch provides a method of pulse timing control, and therefore jitter reduction, compared with a solely passively Q-switched system. The passively Q-switched component here is used mainly to ensure TEM_{00} oscillation and prevent higher order modes. The laser diode module produced 20 W of pump power and the system was CW pumped. The AOM was driven at a repetition rate of between 4.8 and 16.2 kHz during the experiment, which dictated the rep-rate of the Q-switched pulse. The timing jitter achieved using the combined active and passive Q-switch was 400 ns, compared with 56 µs using only passive Q-switching. Whilst this is a significant reduction in timing jitter, the purpose of our research is to avoid active Q-switching completely so this technique is not suitable for our application.

3.1.4.3 Independently bleached saturable absorber

A jitter reduction technique described by B. Cole. et. al. [5] uses a separate laser diode bar, additional to the pump diode, to bleach the Cr:YAG saturable absorber. This provides control over the precise instance of saturable absorber bleaching, independent of the main cavity oscillation. The bleaching diode is positioned orthogonal to the direction of oscillation. A jitter reduction from 241 ns to 20 ns is achieved using the bleaching diode, compared with standard repetitive Q-switching under CW pumping. The Q-switched pulse separation was found to be 198 μs. This technique would not be ideal for our configuration given that it requires additional driving electronics and optical components.

Having considered some of the jitter reduction techniques, we will now describe the rate equation model that we have used to model our laser system.

3.2 Theory

The following sections describe the handling of laser rate equations used to model the production of a passively Q-switched pulse. This model is used extensively throughout the rest of the thesis. We explain how the model is applied to estimate the effects of spontaneous emission noise and also pump power fluctuations on the pulse timing jitter.

3.2.1 Rate equation modelling of a 3-level Nd:YAG system

To assess the root cause of our satellite pulses we have turned to rate equation modelling. The following set of equations is based on work carried out by Ng et. al. [11]. The fundamental difference of this model to others is the assumption that the lifetime of the lower laser level of Nd:YAG is not infinitely short. It is their view that when considering the finite lifetime of this level in certain four-level gain medium, the model predicts a secondary satellite pulse. The rate of change in the density of cavity photons is given by:

$$\frac{d\phi}{dt} = \phi\frac{1}{\tau_r}\left(\left(2\sigma_g l_{eff} n\right) - \left(2\sigma_s l_s N_s\right) - \left(2\sigma_{es} l_s N_{es}\right) - \left(ln\left(\frac{1}{R}\right) + L\right)\right) + \frac{\kappa N_2}{\tau_f},$$

Equation 3.1

where ϕ is the cavity photon density in m^{-3}, R is the output coupler reflectivity (no units), L is the round trip parasitic losses, τ_f is the fluorescence lifetime of Nd:YAG in *s*, τ_r is the resonator round trip time in *s*, σ_g is the effective stimulated emission cross section of Nd:YAG in m^2, σ_s and σ_{es} are the ground and excited state absorption cross sections of the saturable absorber, respectively, in m^2, l_{eff} is the effective length of the gain material over which 95 % of the pump light is absorbed in m, l_s is the length of the saturable absorber crystal in m, n is the population inversion density (i.e. N_2-N_1) in m^{-3}, κ is the efficiency of spontaneous emission coupling with the laser mode [12], N_2 and N_1 are the population densities of the upper and lower laser level of Nd:YAG, respectively, N_s and N_{es} are the ground and excited state population densities of Cr:YAG in m^{-3}. The population densities N_2, N_1 and N_s are calculated using the following equations:

$$\frac{dN_2}{dt} = P - (\gamma_{20} + \gamma_{21})N_2 - \sigma_g c\phi n\,,$$

Equation 3.2

$$\frac{dN_1}{dt} = -\gamma_{10}N_1 + \gamma_{21}N_2 + \sigma_g c\phi n\,,$$

Equation 3.3

$$\frac{dN_s}{dt} = \gamma_s(N_{s0} - N_s) - \sigma_s c\phi(N_s)\,,$$

Equation 3.4

where $\gamma_{20}$is the rate of decay of the upper laser level of Nd:YAG into the ground state, γ_{21} from the upper laser level to the lower laser level, γ_{10} from the lower laser level to the ground state, γ_s is the rate of decay of the excited state of Cr:YAG in s^{-1}, c is the speed of light in ms^{-1}, N_{s0} is the total population density of Cr:YAG (N_s+ N_{es}) in m^{-3}, and P is the pumping rate density of the upper laser level of Nd:YAG as given by:

$$P = \frac{P_{\text{in}}}{h\upsilon_{\text{p}}}\left(\frac{1 - exp(-\alpha_{\text{g}} l_{\text{g}})}{\pi\omega_{\text{p}}^2 l_{\text{eff}}}\right)$$ Equation 3.5

where P_{in} is the pump power incident on the rod face in W given by $P_{\text{in}} = \eta P_{\text{P}}$, where η is the coupling efficiency of the pump radiation into the rod and P_{P} is the total available pump power of the laser diode stack, $h\upsilon_{\text{p}}$ is the energy of a 1064 nm photon in J, ω_{p}^2 is the pump beam radius in m, α_{g} is the absorption coefficient of Nd:YAG in m^{-1}.

With the variables and parameters explained, we can now outline the important terms in each equations. The significant terms in the equation for the rate of change of the cavity photon density (Equation 3.1) are as follows:

$\left(2\sigma_{\text{g}} l_{\text{eff}} n\right)$ adds photons to the cavity by the stimulated emission of the Nd:YAG population inversion (N_2 - N_1).

$-(2\sigma_{\text{s}} l_{\text{s}} N_{\text{s}})$ and $-(2\sigma_{\text{es}} l_{\text{s}} N_{\text{es}})$ subtracts photons by absorption of the saturable ground and excited state, respectively.

$-\left(ln\left(\frac{1}{R}\right) + L\right)$ is the useful loss of photons (i.e. output coupling) and the parasitic (non-uselful) losses in the cavity.

$+\frac{\kappa N_2}{\tau_{\text{f}}}$ is an additive term which couples a portion of the fluorescence into the resonating cavity photons.

The following diagram (Figure 3.3) illustrates the transition rates of each energy level described by the above set of equations Nd:YAG.

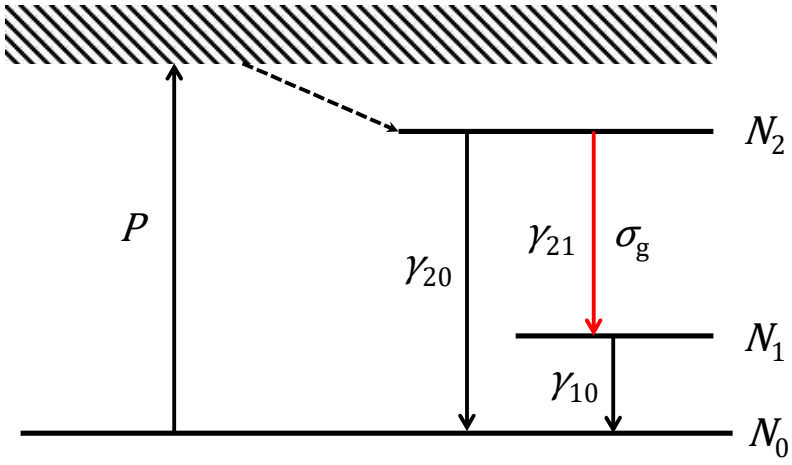

Figure 3.3: Energy level diagram illustrating the Nd:YAG transition rates described by Equations 3.2 and 3.3. The pump band is shown as diagonal stripes, with a fast non-radiative transition to the N_2 level shown as a dashed line. The 1064 nm laser transition is shown in red.

The terms in Equation 3.2, which models the rate of change of the population density of the upper laser level (N_2) can be explained with the aid of Figure 3.3 as follows:

P is the pumping term which excites the Nd ions from the gound (N_0) to the excited state (N_2), via a fast non-radiative relaxation from the pump band.

$-(\gamma_{20} + \gamma_{21})N_2$ is a subtractive term owing to the decay of the N_2 level into the N_1 and N_0 level, as governed by the rates γ_{21} and γ_{20}, respectively.

$-\sigma_g c\phi n$ is another subtractive term in which laser emission (1064 nm) occurs by the stimulated transition from the N_2 to the N_1 level.

We have an additional rate equation (Equation 3.3), compared with typical models, which considers the finite lifetime of the lower laser level (N_1). The rate of decay (γ_{10}) from N_1 to N_0 (ground state) is typically assumed to be infinitely fast and therefore this level is usually not considered. However, we have chosen to include this term based on the work by Ng. et. al. [11]. The relevant terms are:

$-\gamma_{10}N_1$ subtracts from the N_1 population via fast non-radiative decay to the ground state.

$+\gamma_{21}N_2$ increases the population of N_1 by the decay of the N_2 level

$+\sigma_g c\phi n$ adds to the N_1 population by the stimulated emission of the N_2 level

We can now evaluate the populations and transitions of the saturable absorber, in this case Cr:YAG, according to Equation 3.4 and Figure 3.4

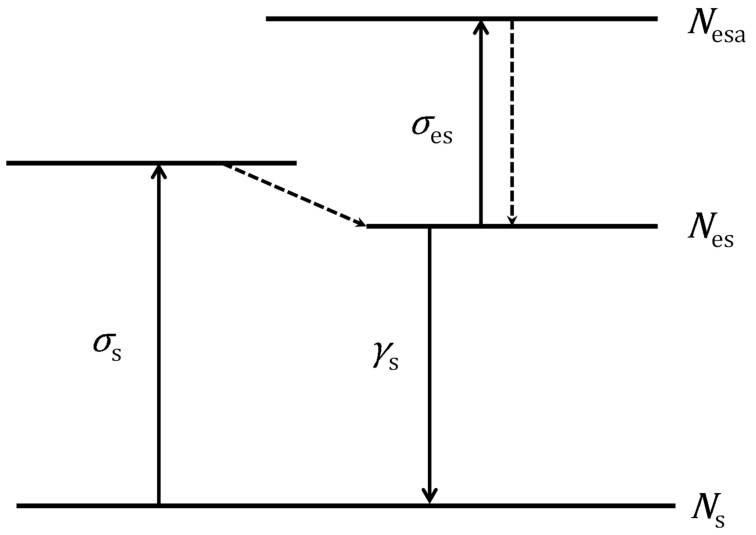

Figure 3.4: Energy level diagram illustrating the Cr:YAG transition rates described by Equation 3.4.

The decay from the N_{esa} level is assumed to be infinitely fast such that there is never an appreciable population, therefore we do not consider this level in the rate equations. The ground state (N_s) population is governed by the following terms from Equation 3.4:

> $\gamma_s(N_{s0} - N_s)$ increases the ground state population (N_s) by the decay of the excited state (N_{es}), where $N_{s0} - N_s = N_{es}$
>
> $-\sigma_s c\phi(N_s)$ subtracts from the ground state population (N_s) following the stimulated transition from the excited state (N_{es}) by the resonating cavity fluence (ϕ)

In the following section we describe how we have used this set of rate equations to model how spontaneous emission noise affects timing jitter.

3.2.2 Spontaneous emission noise modelling

We use the rate equations described above to evaluate whether the uncertainty in the build-up from noise has a significant contribution to the timing jitter, at the microsecond level. The following equation illustrates how we have included a randomised function into the spontaneous emission coupling term (κ) to simulate spontaneous emission noise.

$$\frac{d\phi}{dt} = \phi \frac{1}{\tau_r} \left(\left(2\sigma_g l_{eff} n\right) - (2\sigma_s l_s N_s) - (2\sigma_{es} l_s N_{es}) - \left(\ln\left(\frac{1}{R}\right) + L\right)\right) + \frac{(noise(t))\kappa N_2}{\tau_f}, \quad \text{Equation 3.6}$$

where the term labelled ($noise(t)$) is a periodic function of randomly varying amplitude. The maximum and minimum fluctuations are extracted from experimental measurements further discussed in section 3.3.4. This term randomly varies the point at which the spontaneous emission begins the rapid build-up of an oscillating pulse, thus generating a timing fluctuation of Q-switched pulse generation into the model. The results of this model are described in section 3.3.4.

3.2.3 Modelling variations in pump power vs jitter

A crucial parameter when considering timing jitter, is the fluctuation of pump power. To assess the link between pump power fluctuations and jitter, we can vary the pump power input to the model. Simply entering a maximum and minimum pump power into the model, and determining the difference in the timing of the first pulse in each case, will give a value of timing jitter. The method by which this is carried out is further explained in Section 3.3.5.

3.2.4 Model parameters

Here we present the parameters used in our rate equation model as described above.

Table 3.1: Model parameter values used in rate equation modelling throughout this chapter.

Symbol	Model Parameter	Value
λ	Laser wavelength	1064 nm
L	Cavity parasitic loss	2 %
R	Output coupler reflectivity	70 %
P_p	Pump power	2800 W
t_p	Pump duration	200 µs
η	Pump coupling efficiency	55 %
w_p	Pump beam radius	3.25 mm
w_l	Laser mode radius	3.25 mm
α	Nd:YAG absorption coefficient	1.82 [13]
l_g	Nd:YAG length	5 cm
γ_{21}	Nd:YAG decay rate of 2-1 level	2434.78 s^{-1} [14]
γ_{20}	Nd:YAG decay rate of 2-0 level	1304.35 s^{-1} [14]
γ_{10}	Nd:YAG decay rate of 1-0 level	5 x10^7 [11], 1 x10^9 s^{-1}
τ_f	Nd:YAG fluorescence lifetime	230 µs [14]
σ_g	Nd:YAG stimulated emission cross section	2.8 x10^{-19} cm^2 [13]
k	Efficiency of spontaneous emission mode coupling	1 x10^{-6} [19]
		Cr:YAG
T_0	Saturable Absorber (SA) initial transmission	60 %
l_s	Saturable absorber thickness	1.74 mm
γ_s	SA excited state decay rate	2.44 x10^4 s^{-1} [15]
σ_s	SA ground state absorption cross section	*4 x10^{-18} cm^2 [15]
σ_{es}	SA excited state absorption cross section	*7 x10^{-19} cm^2 [15]

An important consideration is the choice of the value of the Nd:YAG excited state decay rate, which varies enormously across the literature. The value of the Nd:YAG decay rate of 1-0 level (γ_{10}) has been selected based on a review of the measured values by Bibeau et. al. [16]. This study shows a range of values from 0.3 to 30 ns, which indicates the large uncertainty in the parameter value. We have chosen a value of 1 ns in all of our modelling throughout the thesis, with the exception of section 3.3.6.2, which uses a longer lifetime of 20 ns, as reported by Ng et. al. [11], in the analysis of satellite pulses. In any case, varying the lifetime value from 0.3 to 10 ns causes very little change in the modelled laser performance, therefore using 1 ns does

not impact the reliability of the model and also allows faster simulations than a shorter lifetime.

3.3 Experimental method and results

In this section we present the laser apparatus used in our experiments, and define how we measure timing jitter. We then move on to assess each probable cause of timing jitter in our system, using both modelling and experimental data.

3.3.1 1064 nm passively Q-switched laser

In all of the experimental aspects of this chapter we have used a similar arrangement of apparatus. Some areas of the laser setup are slightly altered in order to measure specific characteristics, but the general layout remains the same. This layout is presented in Figure 3.5 and Figure 3.6.

Figure 3.5: Photograph of laser setup, including Spiricon CCD camera, energy sensor and fast photodiode for measurements.

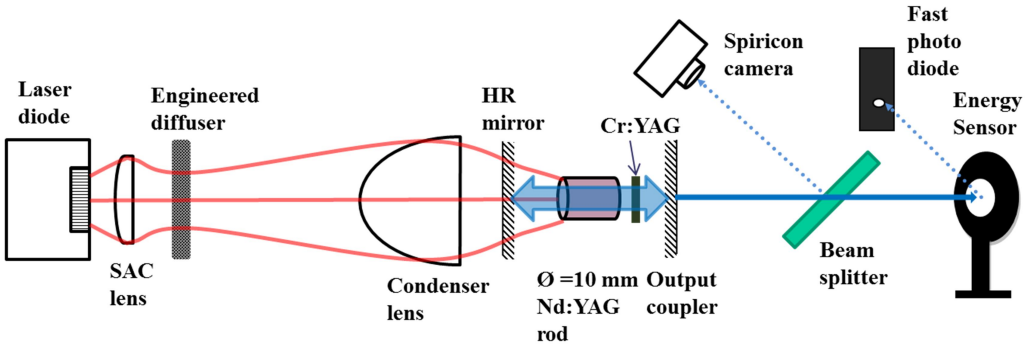

Figure 3.6: Schematic of laser setup, including measurement apparatus.

From left to right the components are as follows. The optical pump source is a 3 kW, 808 nm semiconductor laser, consisting of 12 stacked diode bars each with integrated fast-axis collimating optics. A cylindrical lens is mounted such that the diode's slow-axis of divergence is appropriately collimated. In order to produce a uniform gain distribution, the pump light is directed through an engineered diffuser, which creates a suitably homogeneous beam. The resulting divergent beam is collected by a condenser lens, and coupled into the end of the 10 mm diameter 1 at.% doped Nd:YAG rod. The pump coupling optics, including the engineered diffuser, are discussed in more depth in Chapter 2. Q-switching is achieved by an 10 x 10 mm Cr:YAG saturable absorber crystal of length 1.74 mm. Both crystals are anti-reflection (AR) coated at 1064 nm to minimize parasitic cavity losses. The laser rod is also AR coated at 808 nm to increase the pump coupling efficiency. The crystals are contained within a 10 cm plane-parallel laser cavity, formed by a pump-through high-reflectivity (AR at 808 nm, HR at 1064 nm) mirror on the left and an output coupler (70 % reflectivity) to the right of the laser rod. The energy transmission efficiency of the pump optics onto the rod face is 55 %. The pump laser is driven at 2 Hz, which dictates the repetition rate of the Q-switched output. The Q-switched pulse energy is measured using an Ophir® pyro-electric energy sensor and Laserstar meter. A Spiricon CCD camera was used to observe the beam profile (configured as shown in Figure 3.5 and Figure 3.6) and also, using the focal length method (on a separate test bench), to measure the beam divergence.

3.3.2 Initial jitter measurement technique at 2 Hz

In order to be classified as a laser designator module, the pulse timing jitter has to be below a certain value. Firstly, we describe the timing jitter relevant to this application. At a given repetition rate, the timing of adjacent pulses must not vary by more than ± 5 μs. The segmented oscilloscope trace in Figure 3.7 is representative of the type of measurement used to calculate the timing jitter. For illustrative purposes, only the central 200 ns around each pulse is shown. This is achieved using the oscilloscope in sequence sampling mode, which is programmed to ignore the majority of the time between triggering events (pulses). The interval between each

pulse was then extracted from the precise pulse timing data and the variation (jitter) calculated. The pulse timing data was recorded using a LeCroy Waverunner® oscilloscope in conjunction with a silicon Newport fast photo-diode. The trigger level of the oscilloscope was set to approximately the half maximum level of the Q-switched pulse. The oscilloscope was set to record 500 shots using the segmented acquisition mode. The trigger timings were extracted to calculate the interval between each pulse. The expected pulse interval, 500 ms when driven at 2 Hz, was subtracted from each measured interval to find the max-min jitter value.

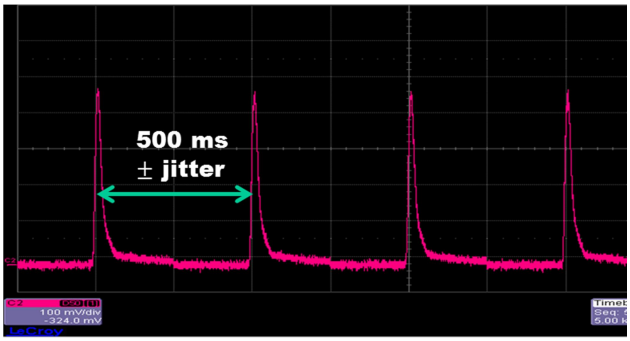

Figure 3.7. Segmented oscilloscope trace of consecutive Q-switched pulses. Most of the dead-time between pulses has been removed for illustrative purposes. The jitter is the fluctuation from the expected pulse interval of 500 ms (2 Hz), as marked on the figure.

Each of the extracted pulse intervals is then plotted on a histogram to illustrate the spread of jitter values, as in Figure 3.8. The max-min jitter value in this example is ± 16 μs, which is well above the ± 5 μs required.

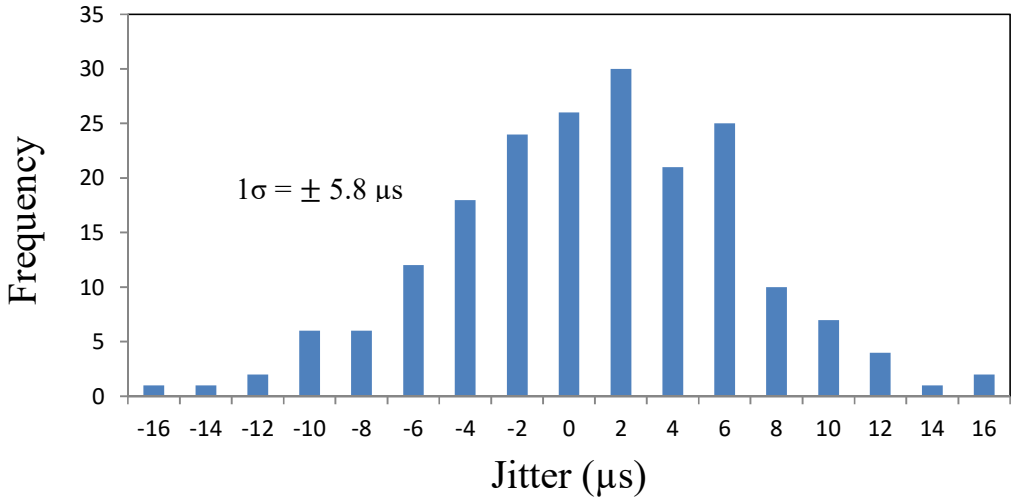

Figure 3.8: Histogram of jitter values, measured over 500 shots, without any jitter reduction techniques in place.

3.3.3 Jitter reduction by environmental isolation

In the following sections we outline the methods used to isolate the laser from environmental vibrations, in an attempt to lower the jitter value to an acceptable level.

3.3.3.1 Air flow analysis

One of the mechanisms we believed to be affecting the stability of our laser was air currents and vibrations. Since the system will always be affected by mechanical vibrations to some extent, it was important to establish whether this was contributing to the high levels of jitter in our case.

To assess whether air currents were affecting the stability of our system, we needed a way of simulating periods of increased air flow. To do this, a can of compressed air (Air-duster) was directed at various components in the resonator. The components targeted were the output coupler, high reflectivity mirror, saturable absorber and directly through the resonator (empty space). The compressed air was released approximately every 50 to 100 shots (25 to 50 seconds). The results of this experiment are presented in Figure 3.9 to Figure 3.12.

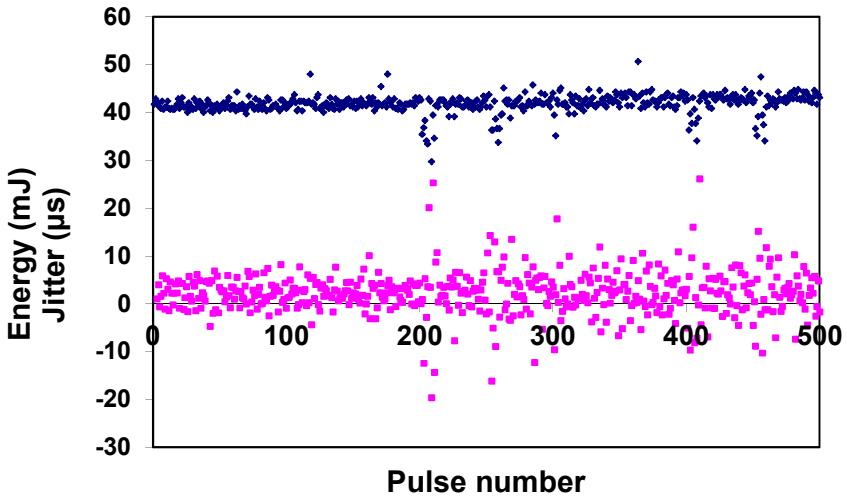

Figure 3.9: Plot of pulse-pulse timing jitter (pink) and pulse energy (blue) over 500 shots. Compressed air was directed at the output coupler to investigate the effects of airflow on the temporal stability of the laser. The distinct fluctuations in both energy and timing occur during periods of increased airflow.

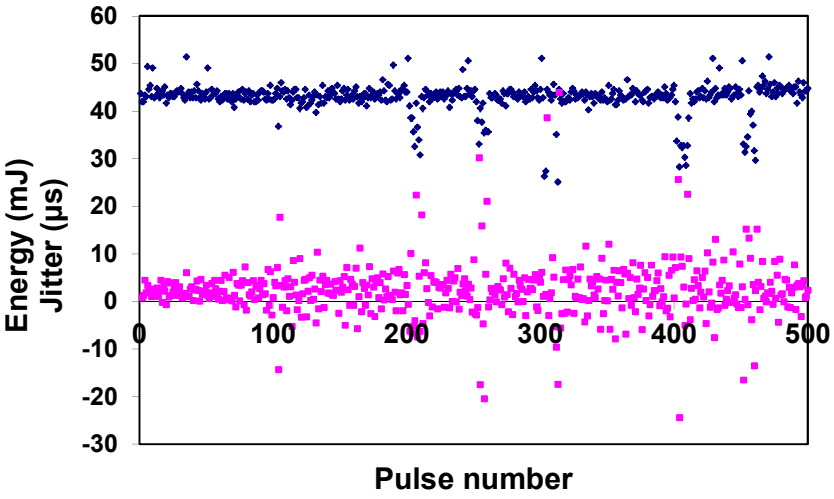

Figure 3.10: Plot of pulse-pulse timing jitter (pink) and pulse energy (blue) over 500 shots. Compressed air was directed at the high reflectivity (HR) mirror to investigate the effects of airflow on the temporal stability of the laser. The distinct fluctuations in both energy and timing occur during periods of increased airflow.

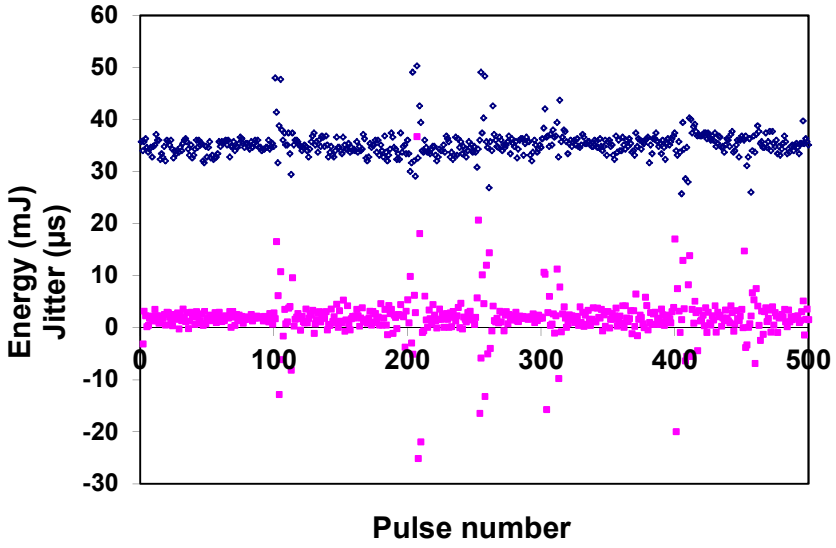

Figure 3.11: Plot of pulse-pulse timing jitter (pink) and pulse energy (blue) over 500 shots. Compressed air was directed at the saturable absorber (Cr:YAG) to investigate the effects of airflow on the temporal stability of the laser. The distinct fluctuations in both energy and timing occur during periods of increased airflow.

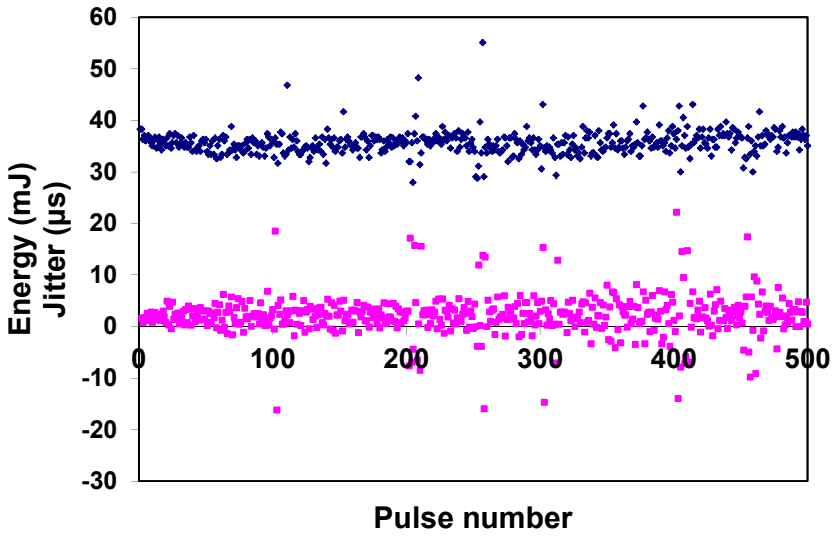

Figure 3.12: Plot of pulse-pulse timing jitter (pink) and pulse energy (blue) over 500 shots. Compressed air was directed through the resonator, avoiding any components, to investigate the effects of airflow on the temporal stability of the laser. The distinct fluctuations in both energy and timing occur during periods of increased airflow.

It can be seen from this figure that during periods of increased airflow, there is a sharp rise in the timing jitter (pink dots). This evidence confirms that the pulse

timing in our system is extremely sensitive to mechanical vibrations. Additionally, during periods of perturbation there is a correlation between high jitter and increased fluctuations in energy. For these reasons it is important to protect the resonator from airflows and dampen any vibrations.

3.3.3.2 Environmental isolation

First, it was important to ensure that the mounts and stages used in the setup were sufficiently resistant to movements. Previously we had been using adjustable, rail-mounted dovetail mounts, for holding the HR and output coupling mirrors. These were replaced with more robust and relatively more static mounts. To further improve the mechanical stability we needed to cover the entire system to protect from air currents. The method we used was to place an enclosure over the whole laser. Next, we needed to reduce the effects of vibrations from the environment (optical table). We positioned a partially inflated bicycle inner tube beneath the breadboard setup. However crude these methods may seem, the results show that increased isolation from the environment has a significant impact on the jitter levels of the system. The results of the environmental isolation are presented in Figure 3.13 and Figure 3.14.

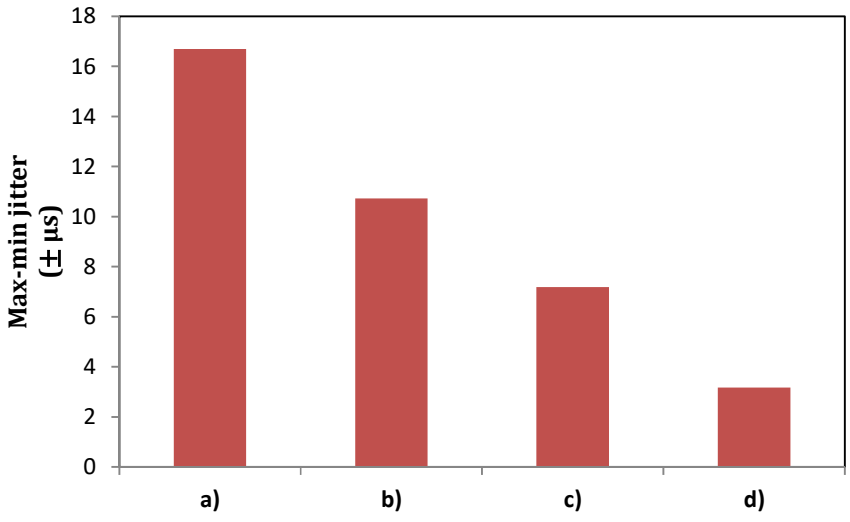

Figure 3.13. Max-min (±) jitter values measured under varying experimental and environmental conditions. These are as follows; a) with OC and HR mirrors positioned on dovetail rail for ease of adjustment, b) mirrors mounted on more permanent and robust

mounts, c) protective cover installed to reduce air flow, d) protective cover used in conjunction with air-filled cushion for vibration dampening.

From Figure 3.13 it can be seen that the initial jitter value of 16 µs (a) is reduced to 11 µs (b) by improving the stability of the mirror mounts. The next reduction to 7 µs (c) was achieved by covering the laser. The most significant reduction comes from using a combination of protective covering and vibration dampening (d), resulting in a jitter value of 3.2 µs.

A pair of histograms are presented in Figure 3.14, showing the improvement of jitter from 16 µs to 3.2 µs. This is now within the ± 5µs required for STANAG compliance [1], The blue data points represent the unaltered (a) setup whereas the pink bars are from the improved setup with the covering and dampening (d). The histograms are composed of 500 hundred jitter measurements each. From this we can establish that the most significant contribution to our system's high jitter levels are from mechanical vibrations and air currents.

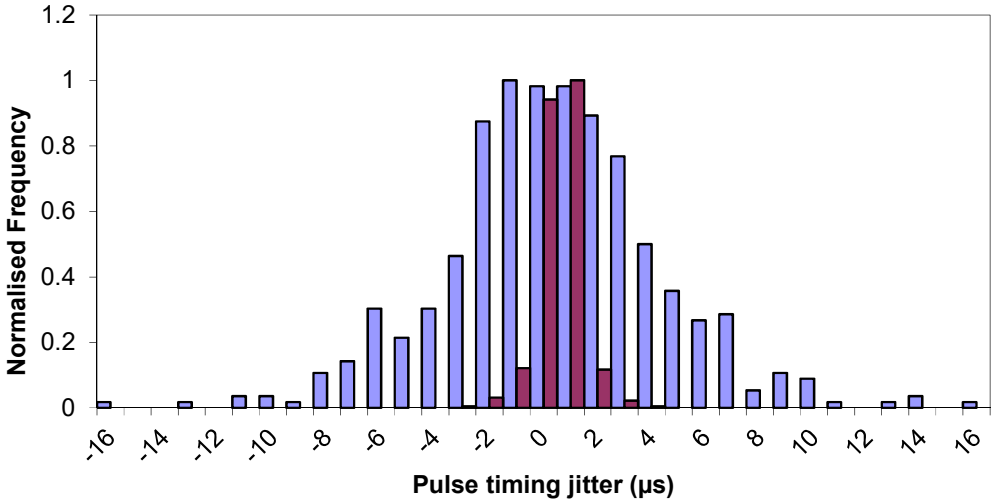

Figure 3.14: Normalised histogram of jitter values for 500 shots before (blue bars) and after (pink bars) airflow and vibration reduction methods have been implemented.

3.3.4 Spontaneous emission noise modelling

In this section we will use the rate equation model combined with our random noise term as described in section 3.2.2. In an attempt to quantify the effects of spontaneous emission, we first had to measure the spontaneous emission noise of our

optically pumped Nd:YAG gain medium. To do this, we positioned the Newport silicon detector directly in front of the laser rod (i.e. without cavity mirrors) and recorded the waveform on the oscilloscope. This is illustrated by the schematic below in Figure 3.15.

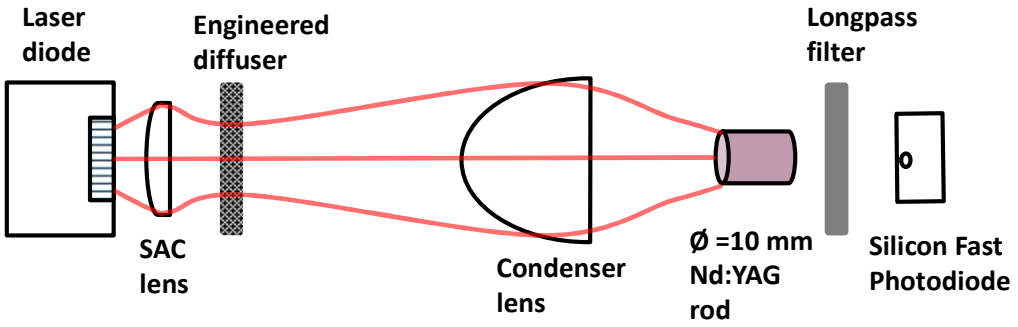

Figure 3.15: Schematic of 1064 nm fluorescence measurement apparatus.

At this stage the laser was not oscillating, so only the 1064 nm fluorescence is being detected. A longpass filter was placed in front of the detector to remove the 808 nm pump light from the detected signal. An oscilloscope trace of the resulting measured fluorescence is presented in Figure 3.16.

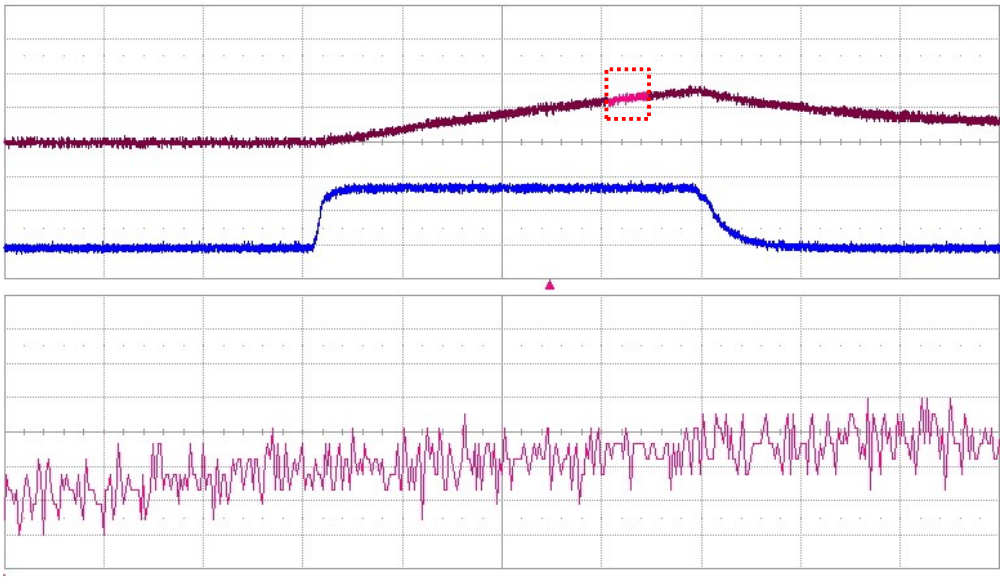

Figure 3.16: Fluorescence output of optically pumped Nd:YAG rod (C2-pink), and current signal of pump diode (C3-blue). The top section, (C2 and C3), has a timebase of 50 µs/division. The lower section (Z2) is a zoomed section of C2, highlighted in the top section by a dashed red box. Rod is pumped for 200 microseconds and output measured with a Silicon fast photo-diode. A longpass filter is used to prevent detection of the 808 nm pump light.

We then used this data to make an assumption of the max-min fluctuation of the fluorescence, and the period at which it fluctuates. From the measurement in Figure 3.16, we have extracted a function which varies randomly with a period of 100 ns, within a floor and ceiling of 0.8 and 1.2, respectively (i.e. a fluctuation of +/- 0.2 around a mean value of 1). Each time the value is randomised, between 0.8 and 1.2, this value is held for a period of 100 ns. This value is used to periodically vary the spontaneous emission-mode coupling term (κ) in Equation 3.1, as described in the theory section 3.2.2. The results of this simulation, ran 500 times, is plotted in a histogram in Figure 3.17.

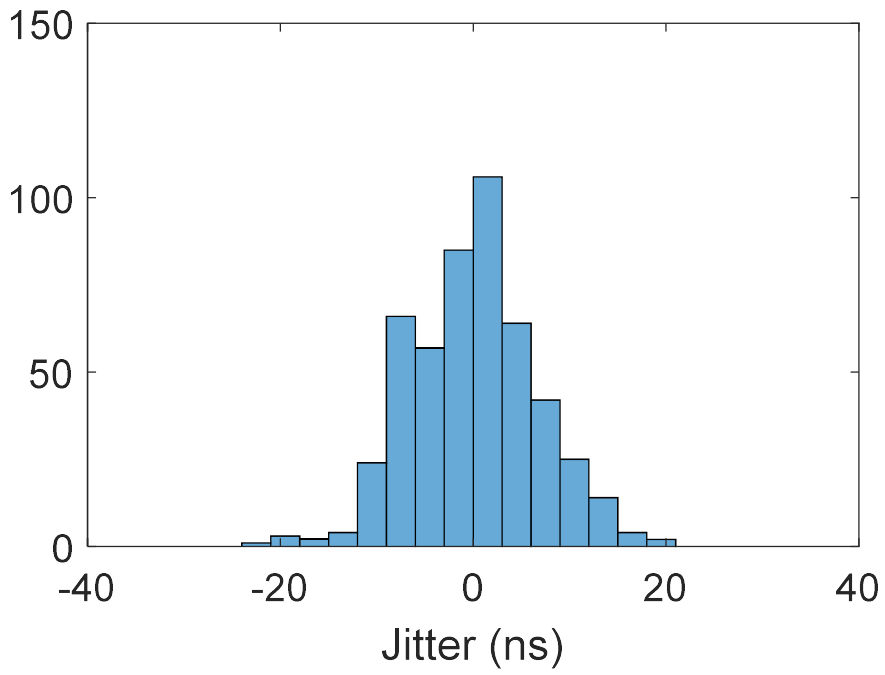

Figure 3.17: Histogram of modelled spontaneous emission noise jitter.

The histogram shows the spread of jitter values from pulse-to-pulse for 500 consecutive pulses, with a pump repetition rate of 2 Hz, using our spontaneous emission model. We can see that there is a much lower instance of timing jitter, with a max-min of only around 20 ns; whereas our experimental results are of the order of microseconds. From this calculation, we can rule out spontaneous emission noise as the cause of timing jitter in our system.

3.3.5 Pump beam instabilities

We describe in this section how we have investigated the link between pump power fluctuations and timing jitter. The details of this mechanism are described previously in sections 3.1.3.2 and 3.2.3. Firstly, we provide a summary of the different ways in which we measured the pump beam fluctuations.

3.3.5.1 Measuring pump beam instabilities

Below is an example of an oscilloscope trace of the current applied to the laser diode stack. It is helpful to refer to this figure when we discuss measurements of the various pump parameters.

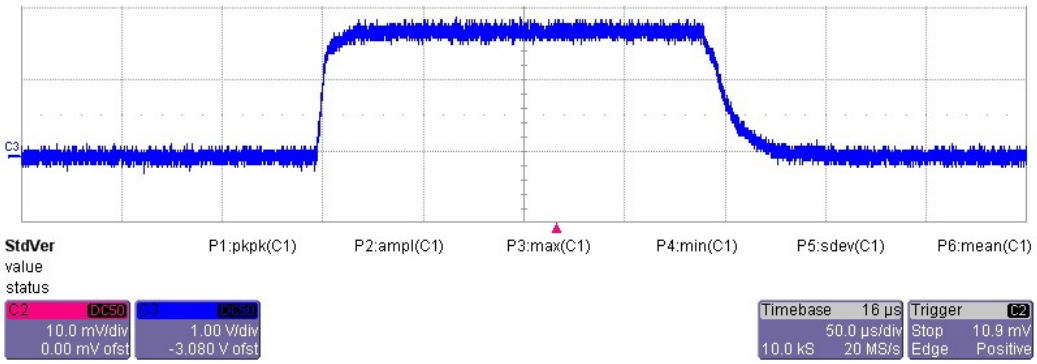

Figure 3.18: Oscilloscope trace of the driver current applied to the laser diode stack, as measured by a Rogowski coil.

There are several different parameters that can be measured to assess the stability of the pump beam. The first would be the pump energy per pulse, which is directly related to the pump power level of the near rectangular pumping pulse and its duration. We measure the pump energy using an Ophir energy sensor and meter, as depicted below in Figure 3.19.

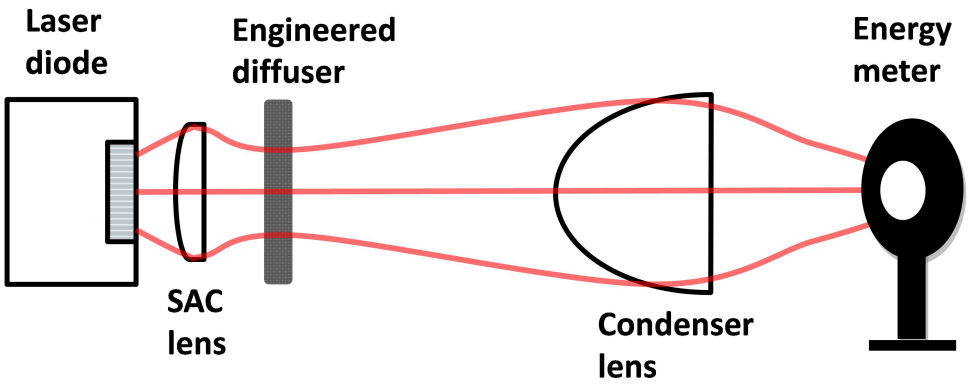

Figure 3.19: Schematic of experimental apparatus for measuring pump fluctuations.

The second set of measurements involves recording the current delivered to the diodes. One method of measuring the current is with a Rogowski coil, which monitors the temporal evolution of the current applied to the diode pump. An example oscilloscope trace of the pulse, as recorded using the Rogowski coil, is presented in Figure 3.18. The pulse area, the total integrated oscilloscope trace, would give provide a measure of the total pulse energy delivered to the silicon fast photo-diode. Whilst we do not know precisely how a variation in input current translates to a fluctuation in output energy, this measurement provides a reasonable approximation for our purposes. The diode driver (Northrop Grumman eDrive) also has an internal current monitor which we have used in our measurements.

The fluctuation in the pump power level is determined from the measurement of the pump energy with a fixed pump time of 200 μs. When recorded over 500 shots, this would indicate how the total energy of each pump pulse varies over time. If this resulted in a maximum 1 % fluctuation in pump energy from the average measurement, this would translate into a 1 % maximum variation in the pump power, assuming we are in a linear regime, and since the pump time is fixed. This power fluctuation can then be fed into a rate equation model to predict the effect on pulse timing. An overview of the variations in the diode pump parameters is presented in Table 3.2.

Table 3.2: Table of measured pump parameter fluctuations. The integrated area under the oscilloscope trace, as measured by the Rogowski coil and internal current monitor, has units of sV (seconds Volts).

	Ragowski current area (sV)	eDrive current area (sV)	Energy (mJ)
Mean	4.33×10^{-4}	3.60×10^{-4}	419
Max-min	6.16×10^{-6}	7.21×10^{-6}	2.5
± % fluctuation	0.71 %	1.0 %	0.60%

To populate this table, the energy sensor is positioned directly in front of the pump diode for an absolute energy measurement, whilst simultaneously observing the temporal profile using the oscilloscope. For each parameter the max-min (the difference of the maximum and minimum values), mean and total % fluctuation are calculated over 500 shots. The maximum percentage fluctuation is calculated by taking the total range (max-min) as percentage of the mean value for each parameter. The process of using these measured fluctuations in our rate equation model (Equation 3.5) involves applying the percentage fluctuation to the pump power (P), using one of our measured values from Table 3.2. We have chosen to use the fluctuation measured by the eDrive current monitor, which is $\pm$ 1 %. This is the highest measured fluctuation and therefore represents the worst case scenario of pump fluctuations.

3.3.5.2 Modelling pump beam instabilities and the effect on timing jitter

Firstly we input into the model, the average pump power of our laser diode pump, which is 2800 kW. We then ran the model and made a note of the precise time at which the first Q-switched pulse was emitted. Then we reduced the pump power by 1 % to 2.772 kW, to simulate a fluctuation in the total delivered pump power. We ran the model a final time with the pump power increased by 1 %. The difference in the

pulse timing of the perturbed pulses represents the timing jitter associated with a pump power fluctuation of ± 1 %. The results are presented below in Figure 3.20.

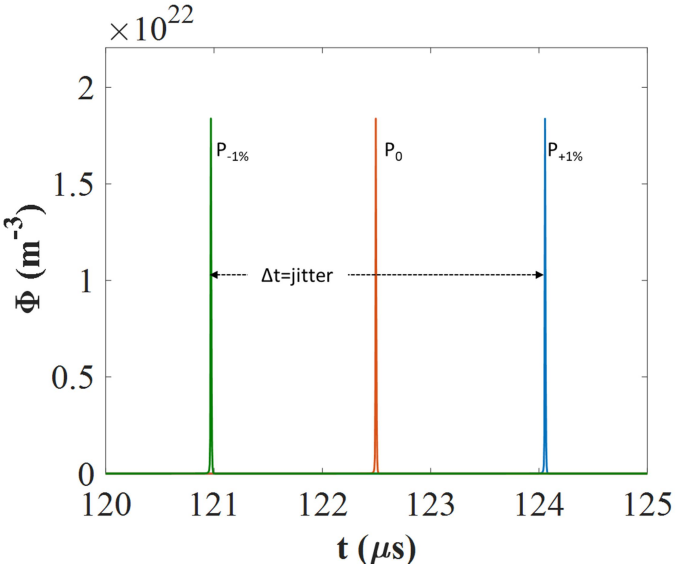

Figure 3.20: Plot of cavity photon density against time for modelled Q-switched pulses, calculated using pump power varied by ± 1 %. Lower laser level lifetime of Nd:YAG was set to 1 ns. The Δt of $P_{+1\%} - P_0$ is marginally longer than $P_0 - P_{-1\%}$

It was calculated that a 1 % fluctuation in pump power resulted in a max-min timing jitter of ± 1.55 µs. Given that we have measured a residual jitter after environmental isolation to be 3.2 µs, we can conclude that pump fluctuations can make up a significant portion of the remainder. Further experimental evidence of the effect of pump fluctuation on jitter can be found by varying the threshold pump pulse length in the laser by introducing different cavity losses and pump efficiencies.

3.3.5.3 Experimental confirmation of the impact of pump fluctuations on timing jitter.

If there is a strong link between pump power fluctuations and jitter we would expect to see an increase in jitter with increasing threshold pump duration. This is because the longer pump time required to reach threshold will lead to a wider variation in total pump energy due to the likely fluctuation in the pump power. This is exactly what we see in Figure 3.21 below which shows the jitter value for resonators with different cavity optics and pump/beam overlaps to change pump efficiency. All of

the jitter values are plotted on the positive y-axis, for ease of interpretation of the results.

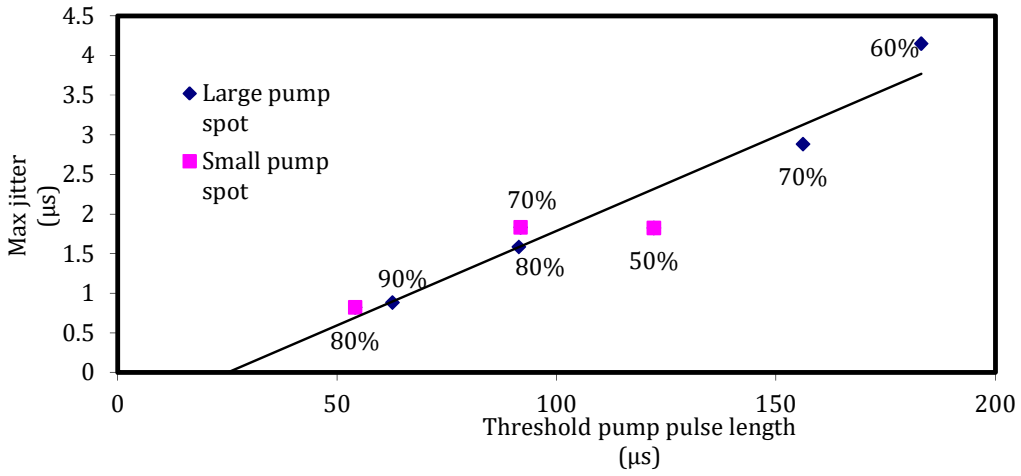

Figure 3.21: Plot of maximum timing jitter for Q-switched pulses against threshold pump pulse length, for different saturable absorber initial transmissions and pump spot size. The maximum jitter and average energy are calculated from 500 consecutive laser pulses for each initial transmission. The initial transmission is noted beside each data point. The purple data points are from a system using a small, more intense, pump spot. The blue data points are obtained using a larger, less intense, pump spot. Linear fit to the data points is for illustration of the upward trend of jitter vs threshold.

We used two different pump spot sizes to provide extra data points, the larger spot size has a relatively lower pump intensity with the same pump power, and in turn results in a relatively longer threshold pump time. The results here confirm that the pump power fluctuations have a strong impact on the Q-switched jitter, since the jitter increases the longer the pump duration.

It is important, not only to investigate pump power fluctuations, but also pump timing jitter and the impact it has on Q-switched jitter. To investigate the effect of the pump pulse jitter, we have measured the Q-switched pulse jitter against pump pulse jitter for each shot. The experimental setup is shown below.

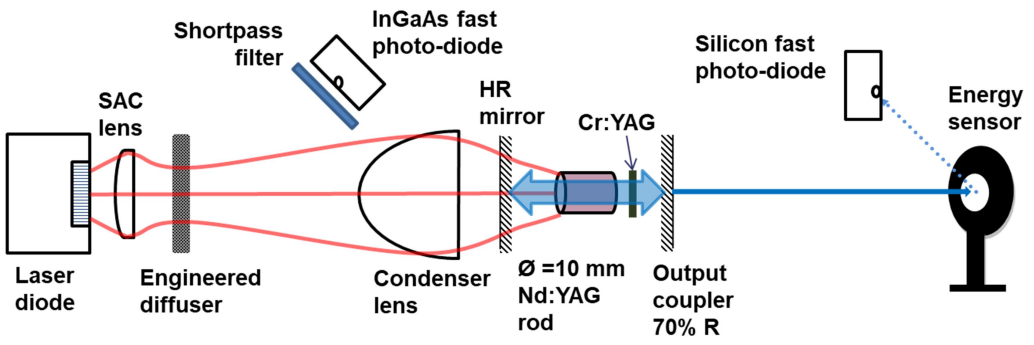

Figure 3.22: Schematic of laser setup used to measure pump and Q-switched jitter simultaneously. A shortpass filter is used to prevent the InGaAs photo-diode from detecting the Q-switched pulse.

For each Q-switched pulse recorded with the Silicon detector, the corresponding pump pulse is recorded using the InGaAs detector. A shortpass filter is used with the InGaAs photo-diode to ensure only the pump beam is detected. A plot of the resulting data is shown in Figure 3.23. Each point on the graph shows the Q-switched jitter on the y-axis, with the corresponding pump jitter on the x-axis.

From Figure 3.23, it is difficult to see any significant relationship between the pump jitter and the Q-switched jitter. Whilst there is likely to be some timing jitter carried over from the pump to the Q-switched pulse, it is not the dominant mechanism. If the pump jitter was the most significant factor contributing to jitter we would expect the data to follow a 45° gradient, where an increase in jitter would result in an equivalent increase in Q-switched jitter. Therefore the correlation between pump jitter and Q-switched jitter is weak. When considering the pump pulse, the dominant contribution to the Q-switched jitter is more likely to be the fluctuations on pump power.

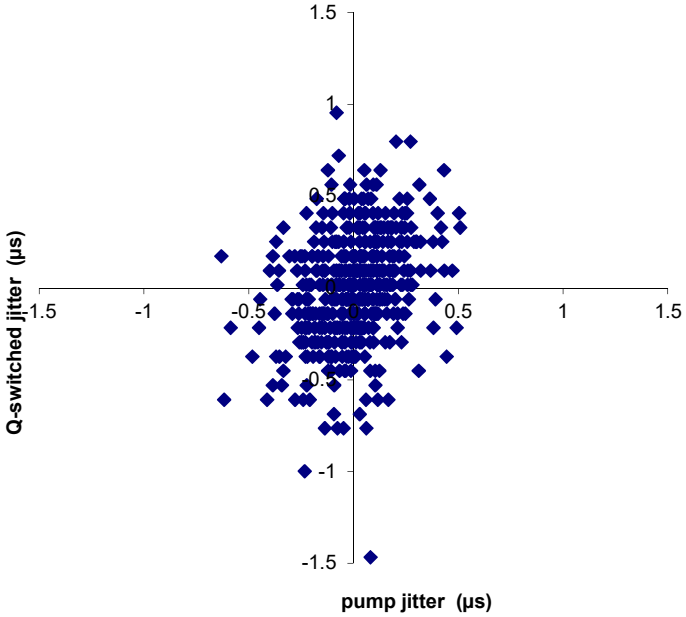

Figure 3.23: Plot of Q-switched jitter against pump jitter. Both are measured using separate fast photodiodes connected to an oscilloscope.

In the following sections we will outline our investigation into the mechanism responsible for satellite pulses, and how it affects timing jitter. The three areas we will assess are the finite lower laser level of Nd:YAG and transverse and longitudinal mode competition.

3.3.6 Satellite peaks investigation

As mentioned previously, one of the mechanisms from the literature which is reported to contribute to timing jitter is the presence of satellite pulses. In this section we will look into the relationship between satellite peaks and timing jitter, and also investigate the mechanism which may be the cause of the occurrence of these secondary peaks. First we will describe an experiment for analysing the link between jitter and satellite pulses.

3.3.6.1 Investigating the relationship between timing jitter and satellite peaks

To investigate whether this is strongly contributing to our observed levels of jitter, we have measured the timing jitter with and without the presence of these satellite pulses. The experimental setup is equivalent to that shown previously in Figure 3.6.

The oscilloscope trace of each pulse was recorded for 30 shots. Below we present an oscilloscope trace showing Q-switched pulses with an intermittent satellite. Pulses with no satellite are highlighted in blue.

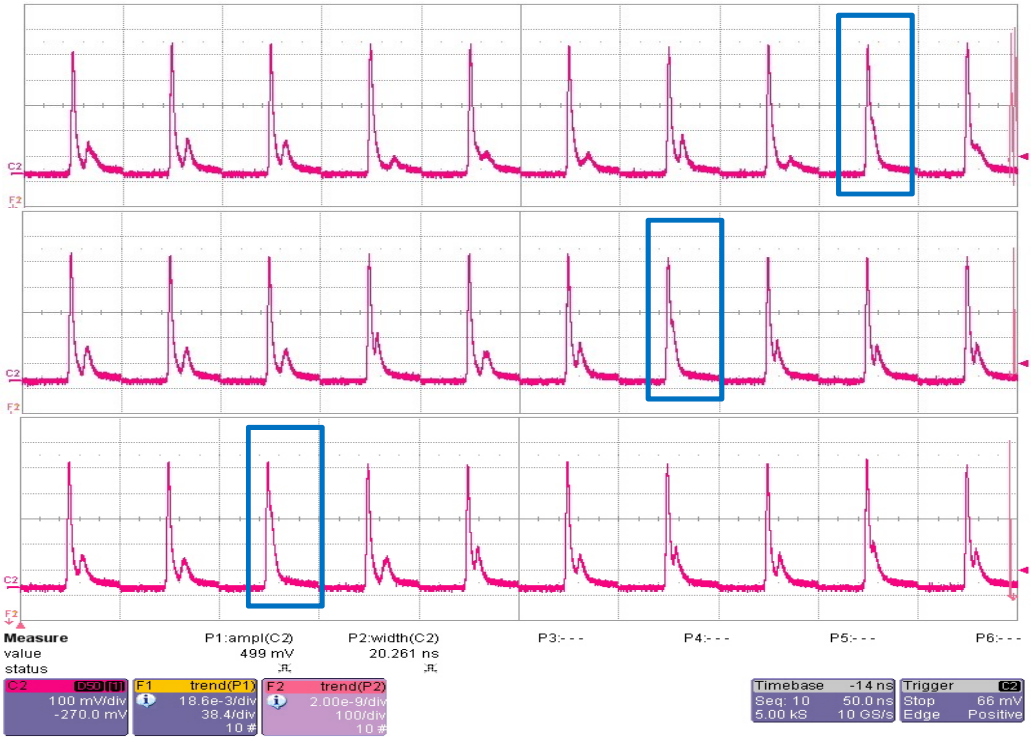

Figure 3.24: Three separate segmented oscilloscope traces of Q-switched pulses. Marked inside blue rectangles are single pulses with no satellite peak. The amplitudes of the satellite peaks are measured using a rule to provide the data for Figure 3.25.

It can be seen in Figure 3.24 that the satellite is present in the majority of Q-switched pulses. For each pulse we measured the timing jitter relative to the previous pulse. The amplitude of each satellite was measured by hand using a rule. The amplitude of the primary pulse, as measured by the oscilloscope, was used to convert this measured size to a voltage. The resulting plot of jitter against satellite amplitude is shown below.

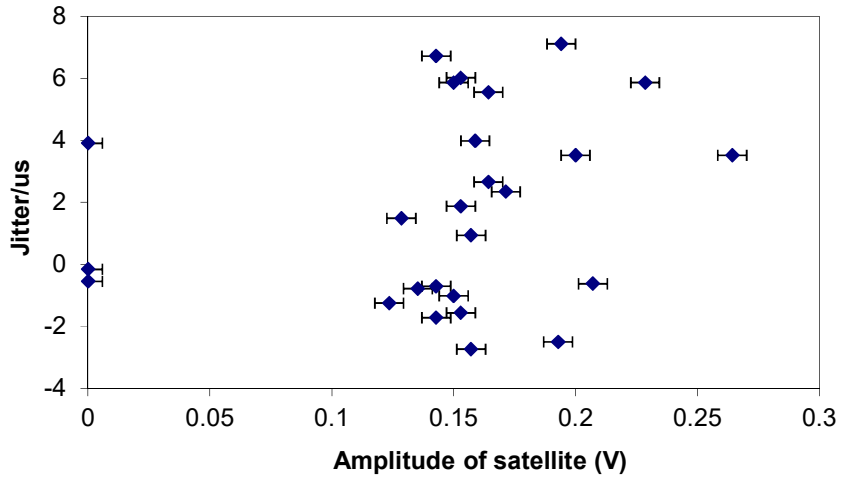

Figure 3.25: Plot of timing jitter against satellite amplitude for pulses shown in Figure 3.24. The error bars are a systematic $\pm$ 0.5 mm converted to a voltage of 5.9 x10^{-3} V.

From Figure 3.25, it can be seen that there is no visible link between the amplitude or presence of a satellite and the corresponding jitter. Although it does not affect the timing jitter, we have chosen to further investigate the origins of this temporal instability, starting with the potential contribution of the finite lower laser level of Nd:YAG, as discussed previously in section 3.2.1.

3.3.6.2 Finite lower laser level lifetime of Nd:YAG

In Figure 3.26 we present the evolution of a pulse as modelled using the parameters from Table 3.1. Using this finite lower laser lifetime model, with a lifetime value of 20 ns [11] , the results show the presence of a satellite pulse that as first glance looks similar to that seen in the experimental data. However, the presence of the pulse depends on the model parameters. If, for example, we use lifetime values from 0.3 ns to 10 ns we see no significant variation in the energy extraction, and crucially no satellite pulse. At this stage, however convenient, it seems unlikely that the satellite pulse generation is a product of this lifetime, owing to the fact it is temporally unstable and moves around on the oscilloscope trace from pulse to pulse. The instability of the secondary pulse cannot be described by this model. We therefore investigate further mechanisms, starting next with transverse mode competition.

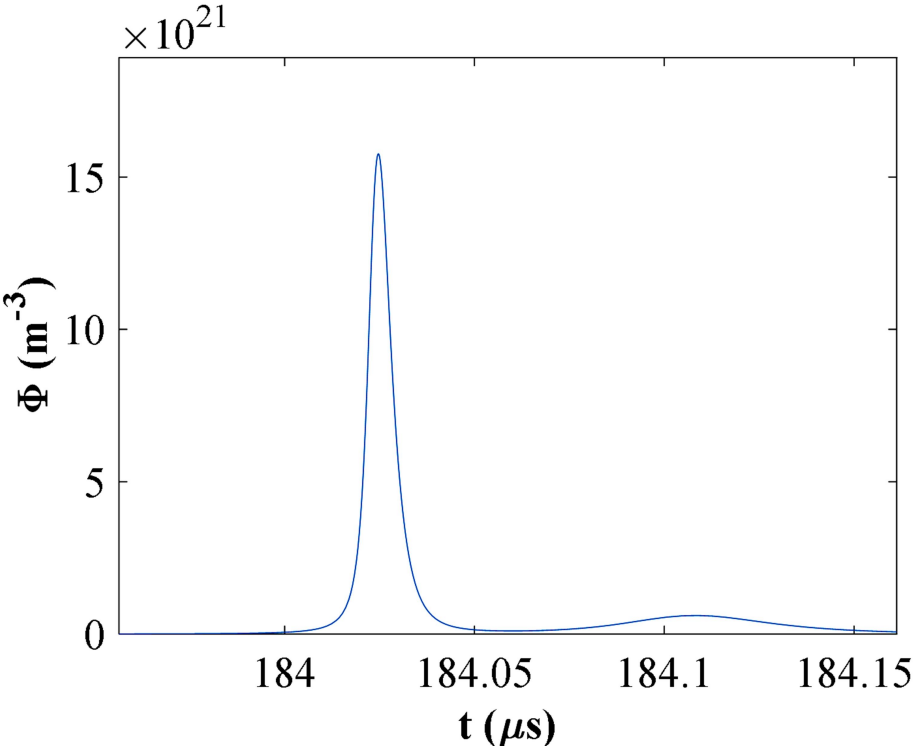

Figure 3.26: Rate equation model results of cavity photon density against time using the parameters from Table 3.1, with the exception of τ_{10} which has a value of 5 x10^7 s^{-1} (i.e lifetime of 20 ns).

3.3.6.3 Transverse mode competition

In this section we will evaluate the likelihood of transverse mode competitions being the mechanism behind satellite pulses and timing jitter. The experiment for this involved modifying the set-up from Figure 3.6, to replace the plane-parallel HR mirror with a curved HR-mirror, and inserting a variable aperture (Iris) into the cavity, as shown in Figure 3.27.

In using a plane-concave resonator configuration the transverse mode composition is focused, thus allowing many more high-order modes to resonate within constraints of the laser rod aperture [17]. With more high-order modes, there is an increased instance of mode competition leading to the emission of multiple, closely spaced, satellite Q-switch pulses. These satellite modes reach threshold at different times, as discussed in section 3.1.3.4. By adjusting the size of the iris variable aperture we can control the number of oscillating transverse modes, since

higher order modes are more divergent. Thus, we can evaluate how the number of modes affects the jitter and number of satellite pulses present. The results of this experiment are shown in Figure 3.28, where the temporal profile of a Q-switched pulse is presented for varying aperture diameters. The temporal profile was measured with a silicon fast-photodiode.

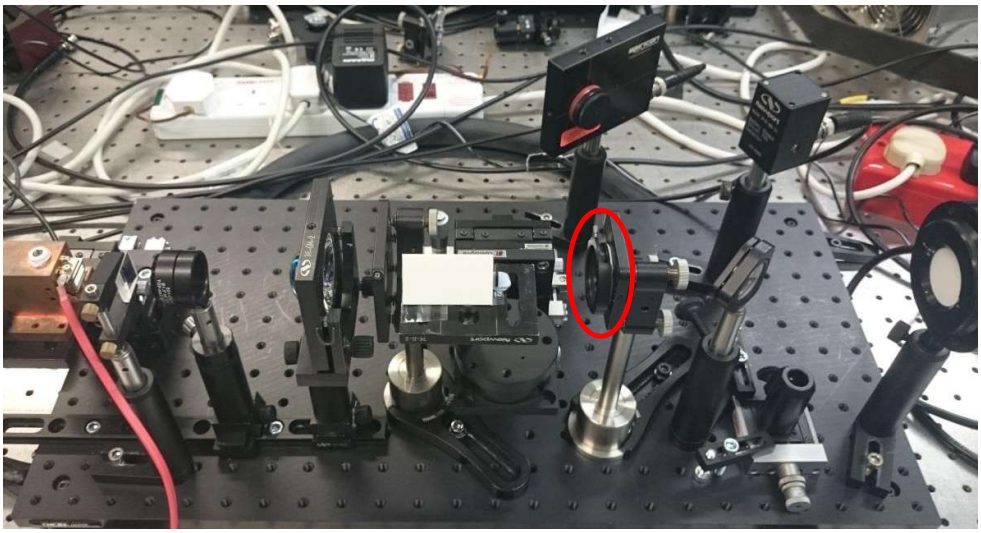

Figure 3.27: Photograph of transverse mode experimental setup. The plane HR mirror has been replaced by a curved mirror of 2 m ROC. An adjustable iris, circled in red, has been attached to the output coupler inside the resonator to aperture out higher order modes.

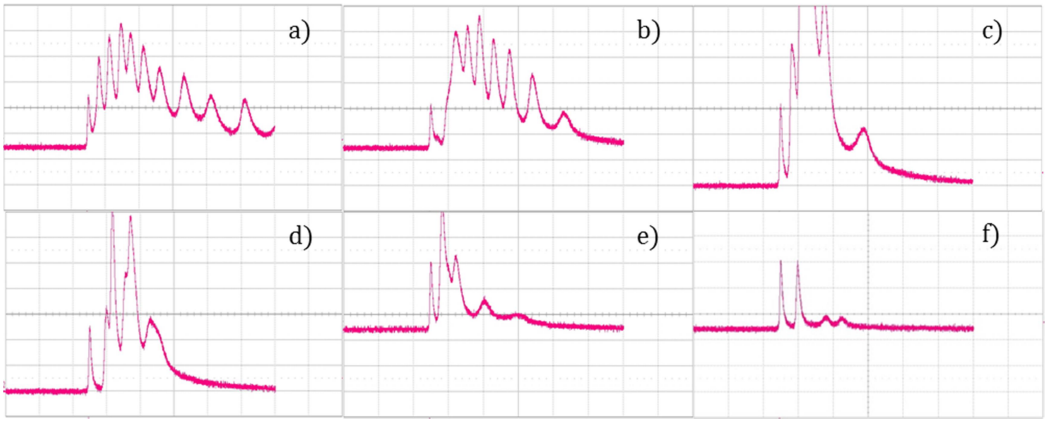

Figure 3.28: Oscilloscope traces of Q-switched output for cases with different sizes of aperture inside the cavity. The time-base on each trace is 200ns/div, the y-scale is different depending on the amplitude of the detected signal. For a)-b) the y-scale is 100 mV/div, c)-f) it is 50 mV/div. This set of oscilloscope traces is to demonstrate the effects of reducing the intracavity aperture on the temporal profile of the Q-switched pulse, specifically the number of satellite pulses. The aperture sizes are as follows: a) 25 mm [iris open fully]; b) 6.5 mm; c) 5.5 mm; d) 4.5 mm; e) 3.5 mm; f) 2.5 mm. The laser is pushed below threshold when the aperture is reduced below 2.5 mm.

In Figure 3.28 a), the aperture is fully open and the maximum number of transverse modes are able to oscillate, resulting in a large number of satellite pulses. In figure b) to f) the aperture is made progressively smaller, resulting in a decrease in the number of transverse modes and therefore satellite pulses. Figure f) represents the smallest possible aperture diameter, without pushing the whole system below threshold and producing no Q-switched pulse.

To assess the impact of increasing mode competition on the timing jitter we have plotted the aperture diameter against timing jitter. This is shown below in Figure 3.29.

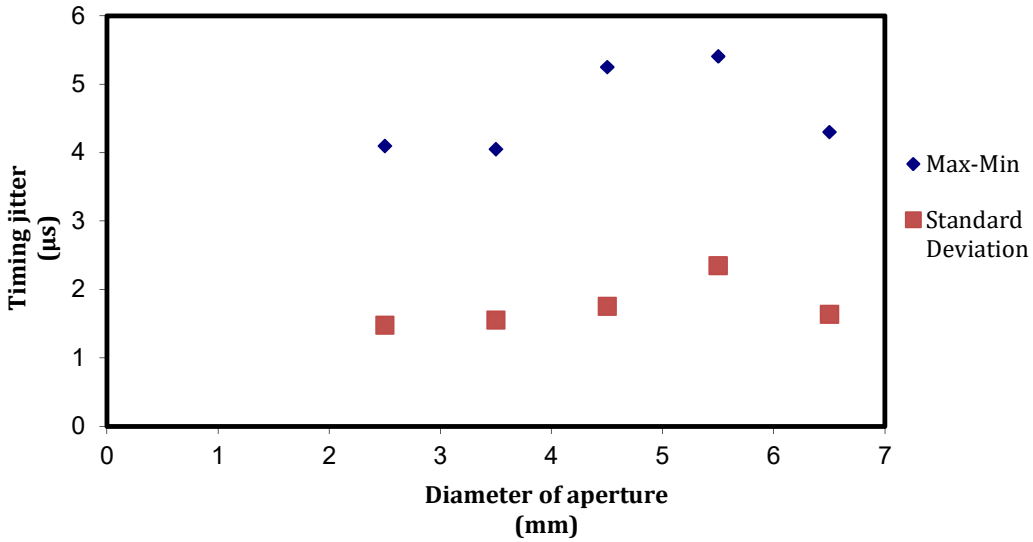

Figure 3.29: Timing jitter against aperture diameter. Both the max-min and standard deviation jitter are plotted.

Considering both the standard deviation and max-min jitter, Figure 3.29 does not show a clear increase with decreasing aperture diameter. The highest value of jitter (both max-min and standard deviation) occurs at a diameter of 5.5 mm and drops again at 6.5 mm. Our plane-parallel cavity has a max-min jitter of 3.2 µs, compared with the highest instance here (5.5 mm aperture) being 5.4 µs. This is evidence that at instances of high transverse mode competition the timing jitter can be affected by over 2 µs. But when the number of transverse modes is lower the variation in jitter is smaller (i.e. compared to the jitter results with a small aperture). With our plane-parallel configuration we see only one satellite pulse, which indicates a less severe instance of mode competition than we see here. However, it is not clear that the

satellite pulse is caused by transverse modes (see next section). Even so, we can conclude that if the satellite peak was due to transverse mode competition, we can expect that the contribution to timing jitter will be a relatively small. We now consider the presence of longitudinal mode competition and the effect on satellite pulse generation.

3.3.6.4 Longitudinal mode competition

As with transverse modes, we would expect that the presence of multiple longitudinal modes would lead to satellite pulses. Hence by looking at the spectral and temporal response of the laser we will attempt to deduce the presence of longitudinal modes.

We will assess the spectral output of two pulses with different saturable absorber initial transmissions, 80 % and 50 %. By comparing this with the temporal profile of each pulse we can better evaluate the link between the temporal satellite pulse and the longitudinal mode composition. Firstly we will look at the 50 % initial transmission case. Presented in Figure 3.30 is an oscilloscope trace showing the temporal profile of the pulse notably including a satellite pulse, followed by the corresponding spectrum of the pulse (Figure 3.31).

From a comparison of the oscilloscope trace and spectrum we can see that there is a small satellite peak in both cases, which closely accompanies a much larger peak. Although the resolution of the spectrometer (1 nm) is not sufficient to fully differentiate between both peaks, it does provide an indication that there may an additional spectral component separate from the main pulse (to the right of the blue dotted line).

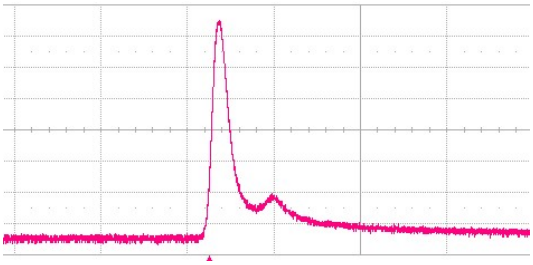

Figure 3.30: Oscilloscope trace of Q-switched pulse produced using a 50 % initial transmission Cr:YAG saturable absorber. The timebase is set to 100 ns/division and the y-axis is set to 50 mV/division.

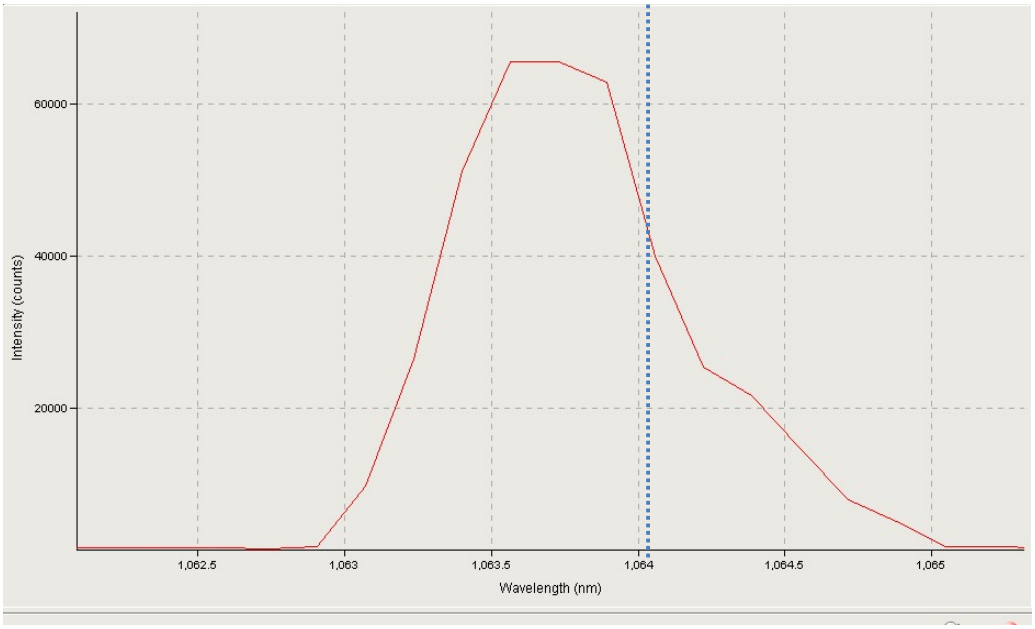

Figure 3.31: Spectral output of Q-switched pulse produced using a 50 % initial transmission Cr:YAG saturable absorber. The figure shows intensity (counts) against wavelength (nm), with the 1064 nm point on the x-axis highlighted by a blue dotted line. The scale of the x-axis is 0.5 nm/division.

The following graphs (Figure 3.32 and Figure 3.33) show the same outputs but this time using an 80 % initial transmission saturable absorber.

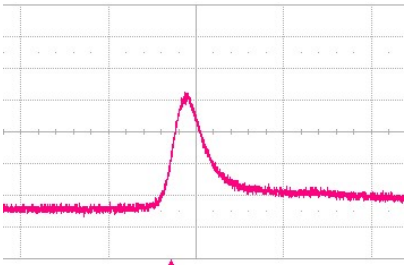

Figure 3.32: Oscilloscope trace of Q-switched pulse produced using a 80 % initial transmission Cr:YAG saturable absorber. The timebase is set to 100 ns/division and the y-axis is set to 50 mV/division.

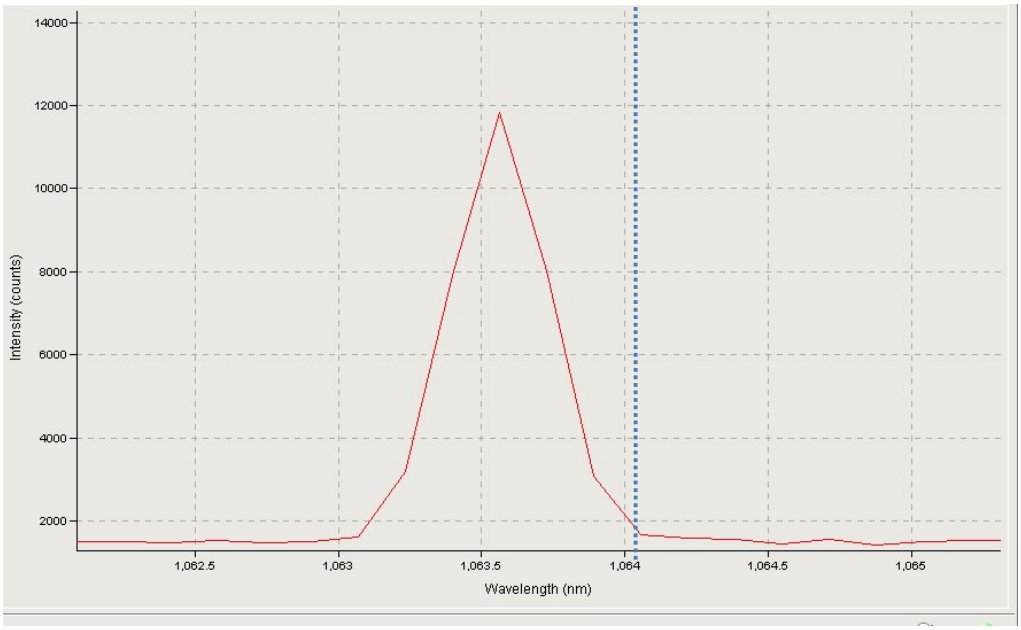

Figure 3.33: Spectral output of Q-switched pulse produced using a 80 % initial transmission Cr:YAG saturable absorber. The figure shows intensity (counts) against wavelength (nm), with the 1064 nm point on the x-axis highlighted by a blue dotted line. The resolution of the x-axis is 0.5 nm/division.

This time, in Figure 3.32, we find that the satellite is barely visible, if not completely diminished, in the temporal profile. Similarly, Figure 3.33 shows little indication of an additional spectral component following the main peak, particularly to the right of the blue line, unlike the 50 % case. From comparison of the 80 % T_0 and 50 % T_0 cases, there is a link between the presence of a satellite peak in the temporal and spectral profiles of the Q-switched pulses. From this evidence we can assume that the presence of the satellite pulse is related to the spectral composition of the pulse.

One possible mechanism is an adjacent longitudinal mode being associated with the temporal satellite pulse, which could potentially have a distinct spectral

component. This mechanism seems less likely when considering the free spectral range of our 10 cm cavity is of the order of 6 x10^{-3} nm. The separation of the primary spectral component and the satellite (Figure 3.31) is approximately 0.5 nm which is 2 orders of magnitude greater that the free spectral range of the cavity. It is for this reason that we believe an adjacent longitudinal mode is not responsible for the temporal satellite pulses as observed in Figure 3.30.

A more likely explanation is that there is an additional transverse mode lasing which is spectrally distinct from the main pulse. This builds on the result of section 3.3.6.3, which is evidence that the number of transverse modes is related to the number of temporal satellites. This observation of multiple transverse modes with distinct spectral components has been observed in vertical cavity diode lasers (VCSEL) by Chang-hasnain et. al. [18]. They have observed a wavelength separation of 0.4 nm between the fundamental TEM_{00} mode and a second high order mode. Whilst these systems are very different to our research, with much shorter cavity lengths, it is evidence for our satellite pulses being caused by transverse mode competition.

3.4 Discussion and conclusions

The first part of our experimental work was to measure the timing jitter values in our breadboard laser. This was found to be $\pm$ 16 μs, which far exceeded the $\pm$ 5 μs required for STANAG classification. It was therefore necessary to identify the prominent jitter mechanisms. From the literature, it is generally accepted that the most prominent cause of jitter is the uncertainty in spontaneous emission noise. We have applied our rate equation model with a randomised element to simulate this. This resulted in a max-min jitter value of only approximately ± 20 ns, which can be considered negligible in our system. We then worked through the most likely potential causes of the jitter with a combination of modelling and experimental work.

We started with environmental factors such as vibrations and air currents. It was identified that when compressed air was directed at the laser, the jitter levels increased significantly. Therefore we protected the breadboard from vibrations and airflow using an inflated inner tube and a protective covering, respectively. This lowered our jitter levels to $\pm$ 3.2 μs, thus identifying mechanical vibrations and air

currents as the primary causes of timing jitter in our system. A more mechanically stable resonator design is discussed in Chapter 5.

We then measured the fluctuations in the diode pump power to model how this may affect timing jitter. A Rogowski coil and the diode driver internal current probe were used to measure the current delivered to the diode, and an energy meter was used to record the energy fluctuations in the pump beam. From this data we concluded that the worst case scenario was a pump power fluctuation of $\pm$ 1 %, as measured by the diode driver's internal current probe. This fluctuation was entered into our rate equation model, which does not consider mechanical vibrations, and a jitter value of $\pm$ 1.55 μs was calculated. This represents a significant portion of the 3.2 μs remaining after environmental isolation, potentially taking the figure down to 1.65 μs if the pump fluctuations were removed.

Another aspect of temporal stability which we have investigated was the presence of a satellite pulse, and how it may impact timing jitter. It was seen that the presence and amplitude of the satellite peak did not have any discernible relation to the Q-switched timing jitter. Despite this, we investigated the potential mechanisms responsible for the satellite pulse, starting with the finite lower laser lifetime of Nd:YAG.

We modelled the effect of having a finite lower laser lifetime in the rate equation models and showed that, above a certain lifetime (around 10 ns), it produced a satellite pulse. However, the reported lifetime values in the literature vary significantly, making it difficult to select the correct value. And in any case the modelled behaviour of the satellite pulse does not match the experiment. In particular modelling shows the satellite pulse to be very broad and fixed in time. In reality, the peak is quite sharp and moves around in time with respect to the main peak between respective pulses.

Next we designed an experiment to investigate the likelihood of transverse mode competition causing the satellite peaks. For this we used a combination of a concave HR mirror and a variable aperture within the cavity, to control the number of high order transverse modes, and therefore increase the instance of mode competition. We found that, even with the aperture at its smallest diameter, there remained an additional satellite pulse which could not be removed without pushing

the whole system below threshold. We did find a link between the instance of transverse mode competition and timing jitter, particularly with a large number of satellite pulses. However, the instance of transverse mode competition is likely to be less extreme in a system with only 1 satellite pulse, and therefore we do not believe it makes significant contribution to the jitter in our system.

We then considered the mechanism of longitudinal mode competition as the cause of satellite pulses. We simultaneously recorded the spectrum and temporal shape of the Q-switched pulse using a 50 % and 80 % initial transmission Cr:YAG absorber. It was found that there was a satellite in both the spectral output and oscilloscope trance with the 50 % sample, but were barely visible with the 80 % sample. Although the resolution of the spectrometer was not optimal, we believe that this is strong evidence that there is a link between spectrally separated peaks and temporally separated pulses (i.e. satellite pulses). We have postulated that this is due to two competing transverse modes oscillating at two distinct wavelengths. As part of future work we should conduct a systematic study relating the character of the satellite pulse and its correlation with the timing jitter.

In conclusion, we have succeeded in lowering the timing jitter of our bread-board laser to acceptable levels for STANAG classification. This was achieved by environmental isolation using a protective cover and an inflated inner tube. We will build on this work with a more mechanically stable resonator in Chapter 5. With a combination of modelling and experimental measurements we then identified that a large portion of the remaining jitter comes from fluctuations in the pump power. A next step would be to insert some feedback loop into the pump driver electronics to ensure a more stable output power. This, in conjunction with a more mechanically stable laser, should bring the total jitter close to $\pm$ 2 µs, which is ideal for designators.

3.5 References

[1] *Standardized Agreement 3733*, 2nd ed. North Atlantic Treaty Organisation, 2005.

[2] T. Dascalu, G. Philipps, and H. Weber, “Investigation of a Cr4+: YAG passive Q-switch in CW pumped Nd: YAG lasers,” *Opt. Laser Technol.*, vol. 29, no. 3, p. 145, 1997.

[3] J. B. Khurgin, F. Jin, G. Solyar, C.-C. Wang, and S. Trivedi, “Cost-effective low timing jitter passively Q-switched diode-pumped solid-state laser with composite pumping pulses.,” *Appl. Opt.*, vol. 41, no. 6, pp. 1095–7, 2002.

[4] A. F. Shatalov and F. A. Shatalov, “Reduction Of The Pulse Repetition Period Jitter Of A Diode-Pumped Passively Q-Switched Solid-State Laser,” *Radiophys. Quantum Electron.*, vol. 52, no. 4, pp. 337–342, 2009.

[5] B. Cole, J. Lei, T. DiLazaro, B. Schilling, W. Trussell, and L. Goldberg, “Reduction in timing jitter for a Cr:YAG Q-switched Nd:YAG laser,” *Proc. SPIE*, vol. 7578, p. 75781Q–75781Q–7, 2010.

[6] X. Wang and Z. Xu, “Timing jitter reduction and single-frequency operation in an acousto-optic Q-switched Cr,Nd:YAG laser.,” *Appl. Opt.*, vol. 45, no. 33, pp. 8477–8483, 2006.

[7] M.-D. Wei, C.-C. Cheng, and S.-S. Wu, “Instability and satellite pulse of passively Q-switching Nd:LuVO4 laser with Cr4+:YAG saturable absorber,” *Opt. Commun.*, vol. 281, no. 13, pp. 3527–3531, 2008.

[8] J. Žabkar, M. Marinček, and M. Zgonik, “Mode competition during the pulse formation in passively Q-switched Nd: YAG lasers,” *IEEE J. Quantum Electron.*, vol. 44, no. 4, pp. 312–318, 2008.

[9] M. Wei, C. Cheng, and S. Wu, “Instability and satellite pulse of passively Q-switching Nd : LuVO 4 laser with Cr 4 + : YAG saturable absorber,” *Opt. Commun.*, vol. 281, pp. 3527–3531, 2008.

[10] J. Bartschke, K. Boller, and R. Wallenstein, “Diode-pumped passively Q - switched self- frequency-doubling Nd : YAB laser,” vol. 14, no. 12, pp. 3452–3456, 1997.

[11] S. Ng, D. Tang, L. Qian, and L. Qin, “Satellite pulse generation in diode-

pumped passively Q-switched Nd: GdVO4 lasers," *IEEE J. Quantum Electron.*, vol. 42, no. 7, pp. 625–632, 2006.

[12] C. J. Mercer, Y. H. Tsang, and D. J. Binks, "A model of a QCW diode pumped passively Q- switched solid state laser," *J. Mod. Opt.*, vol. 54, no. 12, pp. 1685–1694, 2007.

[13] Crytur, "Laser rods - Neodymium doped," *Nd:YAG laser material properties*, 2017. [Online]. Available: https://www.crytur.cz/products/laser-rods-neodymium-doped/. [Accessed: 08-May-2017].

[14] W. Koechner, *Solid-State Laser Engineering*. New York: Springer, 2006.

[15] J. Dong, "Numerical modeling of CW-pumped repetitively passively Q-switched Yb:YAG lasers with Cr:YAG as saturable absorber," *Opt. Commun.*, vol. 226, no. 1–6, pp. 337–344, 2003.

[16] C. Bibeau, S. a. Payne, and H. T. Powell, "Direct measurements of the terminal laser level lifetime in neodymium-doped crystals and glasses," *J. Opt. Soc. Am. B*, vol. 12, no. 10, p. 1981, 1995.

[17] J. Goldsborough, "Beat frequencies between modes of a concave-mirror optical resonator," *Appl. Opt.*, vol. 3, no. 2, pp. 267–275, 1964.

[18] C. J. Chang-hasnain, J. P. Harbison, G. Hasnain, A. C. Von Lehmen, L. T. Florez, and N. G. Stoffel, "Characteristics of Vertical Cavity Surface Emitting Lasers," *IEEE J. Quantum Electron.*, vol. 27, no. 6, pp. 1402–1409, 1991.

Chapter 4 Assessment of Cr:YAG, V:YAG and BDN Dye Saturable Absorbers as Passive Q-switches for High Energy 1064 nm Lasers.

4.1 Introduction

One of the most important design considerations in a passively Q-switched system is the choice of saturable absorber material. Practically, the material has to be readily commercially available, of high quality within manufacturing tolerances, and possess suitable properties to allow efficient Q-switching. These properties are summarised below:

- High ground-state absorption cross section, to allow fast opening of the Q-switch.
- An excited state absorption cross section as close to zero as possible, to limit residual absorption losses once the Q-switch is saturated (open),
- An excited state lifetime many times longer than the output pulse duration, to stop the Q-switch closing prematurely.

In particular, the absorption cross sections of Cr:YAG have been reported to vary considerably between samples [1]. For this reason we have deemed it important to measure the cross sections. Many procedures to find the absorption cross section of a material (i.e. measuring the absorption coefficient of a crystal of known concentration) do not work for Cr:YAG, since the actual concentration of the near infrared (NIR) optical centres is unknown [1]. Instead we have used the Z-scan method to measure the absorption cross sections, which is described in section 4.2. We will now discuss the three materials available, Cr:YAG, BDN dye and V:YAG.

4.1.1 Saturable absorber materials

In this chapter we assess both crystalline and polymer based saturable absorbers for high energy passive Q-switching at 1064 nm.

4.1.1.1 Polymer based materials: BDN

Since the laser was in its infancy in the 1960s, it has been known that certain saturable absorber dyes were viable components for passive Q-switching [2]. The material we are concerned with consists of a saturable absorber polymer dye suspended in transparent acetate. The polymer is - Kodak 15064 - BDN (bis[4-dimethylaminodithiobenzil] nickel) [3]. For many years dye saturable absorbers were the only available products suitable for passive Q-switching and, due to the relatively simple method of production, were very cheap and available in large quantities. Unfortunately, now that the sourcing of these absorbers is much more difficult, many systems reliant on this technology are switching to crystalline saturable absorbers. Dyes also suffer significantly poorer component lifetimes compared with the crystal alternatives [4], so are less attractive from an engineering perspective. It is also not practical to apply optical coatings of a sufficient quality to the acetate substrates, which introduces additional non-saturable cavity losses. Due to the historical importance of these materials in the defence industry, it is useful to compare their performance to the favoured crystalline Q-switches.

4.1.1.2 Crystalline material – Cr:YAG

The most popular material for passive Q-switching at 1 micron is crystalline Cr:YAG. It is extremely durable – optically, thermally, and mechanically – making it an excellent choice for military applications [5]. There are also a number of manufacturers able to prepare the absorbers for passive Q-switching, complete with optical coatings. This allows for security of supply in a laser engineering and manufacturing environment, if one supplier was unable to meet demand. It is also a very well researched material, with many publications available on both the applications and material science of Cr:YAG. This material has so far formed the basis of our engineering research, and the other materials will naturally be compared to its performance and material properties. Cr:YAG has sufficiently high absorption

at 1064 nm and a suitably long excited state decay time, of around 4 μs [6], for efficient nanosecond Q-switching.

4.1.1.3 Crystalline material – V:YAG

The only other commercially available saturable absorber for 1 micron generation is currently V:YAG crystal. It has a much shorter decay rate than Cr:YAG, and it tends to be highly variable, even from the same manufacturer. For example, the decay rate is reported to vary between 5 and 22 nanoseconds, in samples from the same manufacturer. This could pose problems for our system which has previously produced pulses longer than 20 nanoseconds [7]. Despite this, V:YAG may offer a suitable alternative for 1 micron generation.

4.2 Measuring absorption cross sections – Z-scan technique

Although the absorption cross sections of the materials purchased for our experiments are included in the manufacturer's specifications, it has been reported that these can vary considerably, even within samples from the same manufacturer [1]. For this reason we have measured the ground and excited state absorption cross sections of the materials used in our experiments.

In order to evaluate the potential of a particular material as a passive Q-switch, we have used the z-scan experimental technique to measure the absorption cross sections [1]. The materials investigated in this experiment are Cr:YAG and V:YAG. We were unable to measure the cross sections of any BDN dye Q-switches as the samples were unavailable for the duration of the experiment, due to the difficulty of sourcing the material.

We will now describe in full the experimental method used to measure the absorption cross sections. This includes a description of the relevant equations and the treatment of experimental data used in our analysis.

4.2.1 Z-scan experimental method

Below we present the apparatus used in our z-scan experiments [1] to find the ground and excited state cross sections of both V:YAG and Cr:YAG.

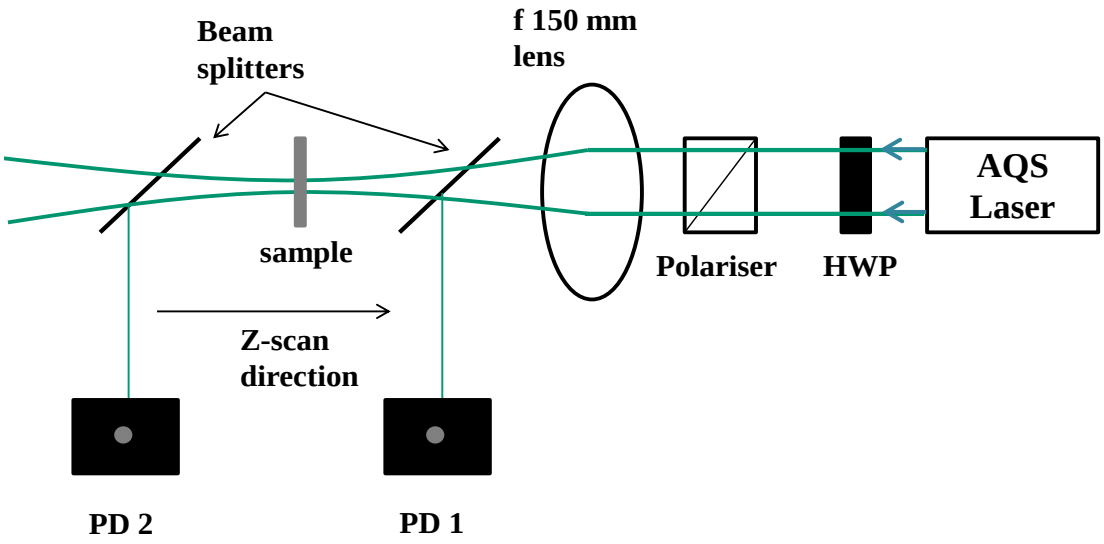

Figure 4.1: Z-scan experiment for measuring the normalised transmitted radiation of a V:YAG or Cr:YAG sample at varying fluence levels. The system uses two photodiodes (PD1 and PD2) to record the relative transmission of the sample. The laser source was actively Q-switched (AQS), and was used in tandem with a half-wave plate (HWP) and polarizer to control the pulse energy incident on the sample.

The apparatus consists of a 2 Hz pulsed laser source at 1064 nm, a half wave plate coupled with a polarizer to control attenuation of the pulse energy incident on the sample, a 150 mm focusing lens to bring the beam to a waist, and two beam splitters to allow a normalised transmission measurement. The laser used was an actively Q-switched (Continuum minilite) 1064 nm laser with a single pulse energy and duration of 100 mJ and 12 ns, respectively. The half-wave plate (HWP) and polariser are used to variably attenuate the total pulse energy incident on the sample by rotating the HWP relative to the polariser. The samples are Cr:YAG from the manufacturer EKSMA and V:YAG from Crytur, both of which are AR coated at 1064 nm. The Cr:YAG sample has a 10 mm diameter square cross section, and the V:YAG has 10 mm diameter circular cross section. A pulsed source was used to provide sufficient fluence to completely bleach the saturable absorber, ensuring that the transmission is confidently measured for the material's saturated state. The experimental methodology is as follows.

The sample is moved in the z-direction at increments of 5 mm, recording the oscilloscope voltage ratio of PD1/PD2 to give the transmission through the sample at each point. The energy at PD1 was measured using an energy meter before and after the z-scan sweep. This, together with the beam caustic trace (Figure 4.3), is used to

calculate the fluence levels at each point. The pulse energy of the laser incident on the sample was variably attenuated by rotating the half wave plate between z-scan runs. This is necessary because the range in beam fluence during a single z-scan run was not sufficient to achieve the full transmission range of the sample (T_0 to T_{SAT}). At low fluence levels, the absorber will be in the unsaturated (T_0) state; then as the fluence is increased, more of the absorbing ions are excited and eventually the excited state becomes saturated (T_{SAT}). This will lead to an S shaped transmission vs fluence curve. The first step in the experiment is to measure the beam caustic trace, which is described in the next section.

4.2.1.1 Beam caustic trace

In order to measure the fluence values at each increment during the z-scan, a beam caustic trace was required. This involved moving a Spiricon CCD camera along the z-direction and measuring the beam diameter at each increment. A diagram of the procedure is presented below, followed by the resulting beam diameter trace in Figure 4.2 and, Figure 4.3 respectively.

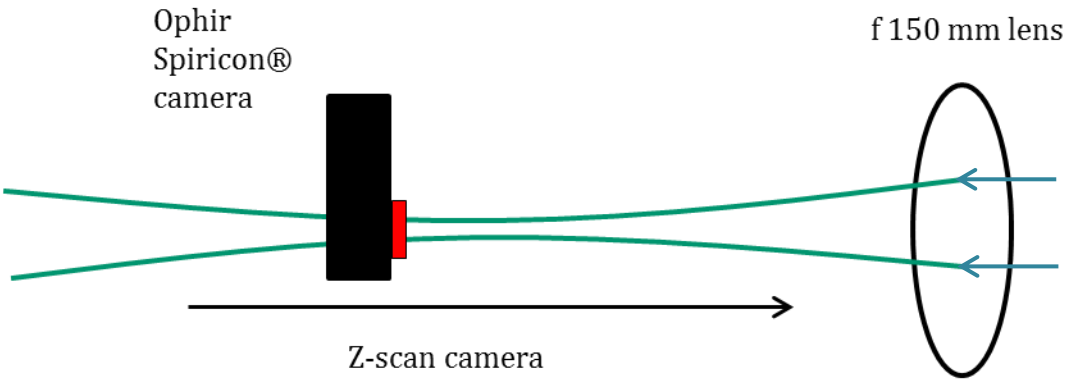

Figure 4.2: Schematic of beam caustic trace experimental apparatus

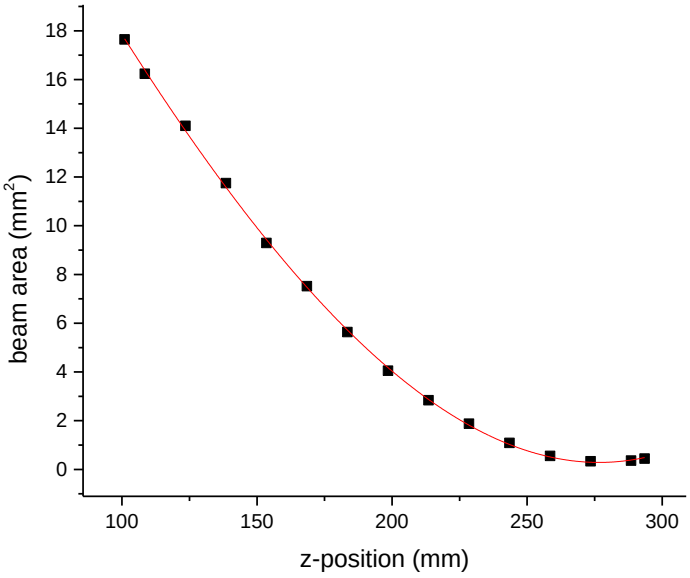

Figure 4.3: Beam caustic trace (beam area against z-position),

The resulting beam area was calculated by measuring the second moment beam diameter (x-axis and y-axis) and approximating an elliptical beam area with a Gaussian intensity distribution. Consequently, we have the position of the beam waist relative to the focusing lens and have the beam area for each point along the z-scan. This data, together with the beam energy measured before each z-scan, is used to calculate the beam fluence for each point along the z-scan. Next we will outline how the measurements were used to calculate the ground and excited state absorption cross section for the materials.

With the transmission values measured for each z-increment, and having measured the caustic beam trace, we can plot the transmission versus the energy density incident on the sample. We now present the relevant equations for fitting a curve to the transmission data and extracting values for the excited state absorption. Following this we present the results of the experiment and subsequent modelling for the 60 % initial transmission V:YAG and Cr:YAG samples.

4.2.1.2 Z-scan theory: curve fitting to find the ground and excited state absorption cross sections

The resulting experimental data consists of a range of beam transmission values for a set of given beam fluence values. The following equations are then used to numerically fit a curve to the data [8]. The equations calculate the relative transmission at a certain beam fluence value, through a sample with a given ground and excited state absorption cross section. We start with an equation which includes the density of absorbing centres N_0, and explain how this can be removed by substitution.

$$\frac{\partial F}{\partial z} = -\sigma_{es} N_0 F + (\sigma_s - \sigma_{es}) \left[\exp\left(\frac{-F}{F_s}\right) - 1\right] N_0 F_s \qquad \text{Equation 4.1}$$

Where F is the beam fluence (J cm^{-2}), z is the thickness of the material (mm), N_0 is the density of absorbing centres (cm^{-3}), σ_s and σ_{es} are the ground and excited state absorption cross sections (cm^2), respectively, F_s is the saturation fluence, which indicates the point at which the saturable transmission reaches 1/e of its total range, given by $F_s = \frac{\hbar\omega}{\sigma_s}$.

Combining this with the definition of small signal, initial transmission: $T_0 = \exp(-N_0 \sigma_s l_0)$, where l_0 is the thickness of the absorber, we can arrange the equation such that it no longer requires the density of absorbing centres N_0.

$$\frac{\partial F}{\partial z} = \hbar\omega \, \frac{\ln(1/T_0)}{l_0 \, \sigma_s} \left[\left(1 - \frac{\sigma_{es}}{\sigma_s}\right)\left(1 - \exp\left(\frac{-\sigma_s F}{\hbar\omega}\right)\right) + \frac{\sigma_{es} F}{\hbar\omega}\right] \qquad \text{Equation 4.2}$$

The data was fitted by solving Equation 4.2 numerically. This was done for a range of σ_s and σ_{es} until an acceptable fit to the experimental data was achieved. The model was fitted to the data first by varying only σ_s. At very low fluence the levels of excited state absorption will be negligible and the excited state will have no

significant population [1]. In this instance it can be assumed that the data collected at low fluence levels relates only to the ground state absorption. Therefore we have fitted the curve to the low fluence by varying only σ_s, whilst holding σ_{es} constant. Once a reasonable fit to the low fluence data has been achieved, σ_s is held constant and the remainder of the data set is fitted to by varying σ_{es}. The model assumes that the beam radius at a given z-position, and therefore the fluence, remains constant throughout the sample. Whilst not ideal, this assumption had to be compromised in our experiments so the beam could be focused, in order to reach sufficiently high fluence levels for saturation of the material.

4.2.1.3 Z-scan curve fitting and calculation of absorption cross sections

Using the theory described above we now present the resulting transmission against fluence graphs for Cr:YAG and V:YAG, respectively. The theoretical fits (red lines in Figure 4.4 - Figure 4.6) were optimised using Equation 4.2. The optimised values of absorption cross section are displayed on the graphs in Figure 4.4 - Figure 4.6.

During the z-scan experiment, the range of fluence values was too large to carry out the scan in a single stage. This was due to the fact that a very high fluence was required to reach saturation, and exploration of the lower section of the transmission curve required the laser pulse energy to be lowered. This meant that the scan was carried out in two stages, at two different oscilloscope V/division scales (readings from photodiodes) and pulse energies. The two sets of data had to be stitched together later, during the analysis, using the two different energy values with the beam caustic trace. The stitch point appears as a slightly flatter region in the middle of the curve, at around 0.2 J cm^{-1} in Figure 4.4. The numerical fit appears to overlap well with the measured data. The ground and excited absorption cross sections used to plot the red curve to the data are σ_s = 2.1 $x10^{-18}$ cm^2 and σ_{es} = 3.13 $x10^{-19}$ cm^2, respectively.

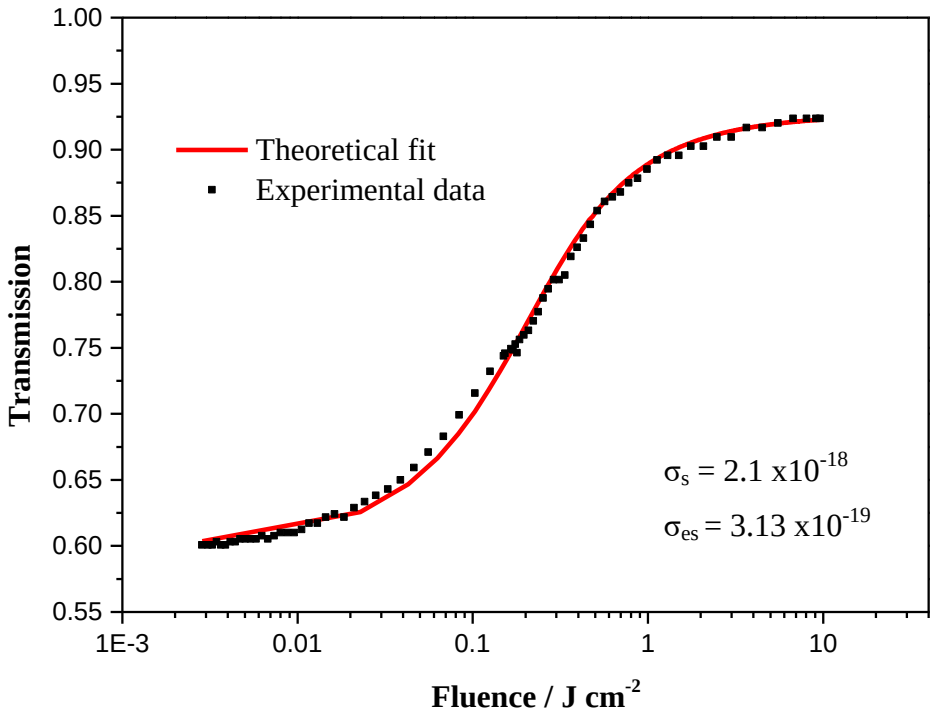

Figure 4.4: Transmission against Fluence for 60 % T_0 Cr:YAG sample (supplied by EKSMA), black dots represent data from the z-scan experiment and the red curve is fitted using the method described in section 4.2.1.2. The ground and excited state absorption cross sections, extracted during the fitting procedure, are presented in the plot area.

We now illustrate how changing the ground-state and excited-state absorption cross sections by a factor of two affect the transmission curve fit. The results are presented in Figure 4.5, with Table 4.1 outlining the cross sections used to plot each curve.

Table 4.1: Table of ground and absorption cross section values used to plot different coloured curves in Figure 4.5.

Curve colour	σ_s (x10^{-18} cm^2)	σ_{es} (x10^{-18} cm^2)
Red	2.1	3.13
Green	4.2	3.13
Pink	2.1	6.26
Blue	4.2	6.26

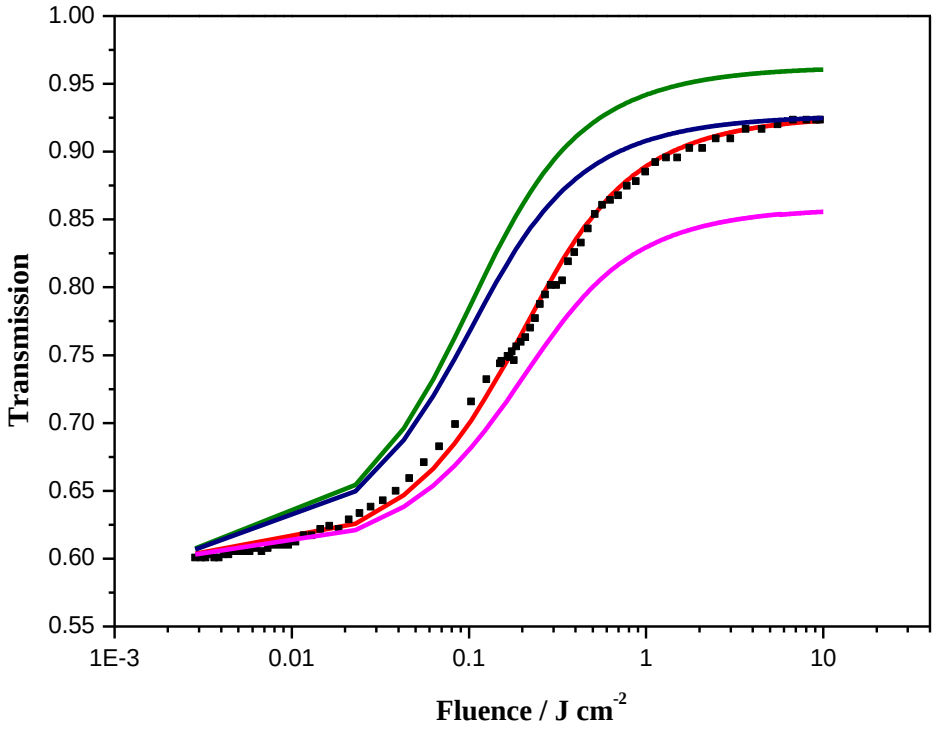

Figure 4.5: Transmission against Fluence for 60 % T_0 Cr:YAG fitted using different values of σ_s and σ_{es} to illustrate how this affects the transmission curves. The black dots represent data from the z-scan experiment and the coloured curves are fitted using the method described in section 4.2.1.2. The curves are fitted using the cross sections as shown in Table 4.1.

The red fitted curve in Figure 4.5 is equivalent to that in Figure 4.4, whereas the other coloured lines are fitted according to variations in the cross sections as shown in Table 4.1. The green curve represents an increase in the ground-state absorption cross section (σ_s) by a factor of 2, compared with the red curve. This results in a lower saturation fluence (i.e. the fluence at which the transmission increases to 50 % of its total range) and a higher final (saturated) transmission value than the red curve. In terms of Q-switching this would be a favourable set of parameters as the losses would switch from high to low faster, and the residual losses would be lower. The blue curve shows what happens if both the ground (σ_s) and excited-state absorption (σ_{es}) are doubled, relative to the red curve. The saturated transmission remains the same as the red curve, at approximately 92 %, because the $\frac{\sigma_{es}}{\sigma_s}$ ratio is equivalent. Again the saturation fluence is reduced compared with the red curve, but to a lesser extent than the green curve due to the higher losses from the increased excited-state (σ_{es}) cross section. The pink curve depicts a reduction in the saturated transmission

due to only the excited-state (σ_{es}) absorption cross section being increased by a factor of two, relative to the red curve. There is also a noticeable increase in the saturation fluence due to the higher losses from the larger excited-state (σ_{es}) absorption cross section. The results of this analysis show that there are visibly significant fluctuations in the fitted curves caused by increasing the ground-state (σ_s) and excited-state (σ_{es}) absorption cross sections by a factor of 2. This gives us more confidence in the fitting procedure used to extract the cross sections from our experimental data.

Next we look at the transmission data from the measurements of the 60 % T_0 V:YAG sample and the extracted absorption cross sections, presented in Figure 4.6. We can see that the fit does not follow the same smooth S-shaped profile as the Cr:YAG sample. This is due to the thickness of the sample (6.22 mm) being 6 times greater than the expected Rayleigh length of the incident pulse (approximately 1 mm). The beam radius does not remain constant throughout the interaction length within the sample, as assumed in the model. We believe this to be the reason that the data is more noisy and the numerical fit is not as good as with the Cr:YAG sample, which had a sample thickness of 1.58 mm. Being only twice the thickness of the estimated Rayleigh length means that the assumption of constant beam radius is more accurate, and therefore the confidence in the numerical fit is greater. We were unable to increase the Rayleigh range (i.e. by increasing the focal length of the lens) any further without dropping the beam fluence below the threshold for complete saturation of the material.

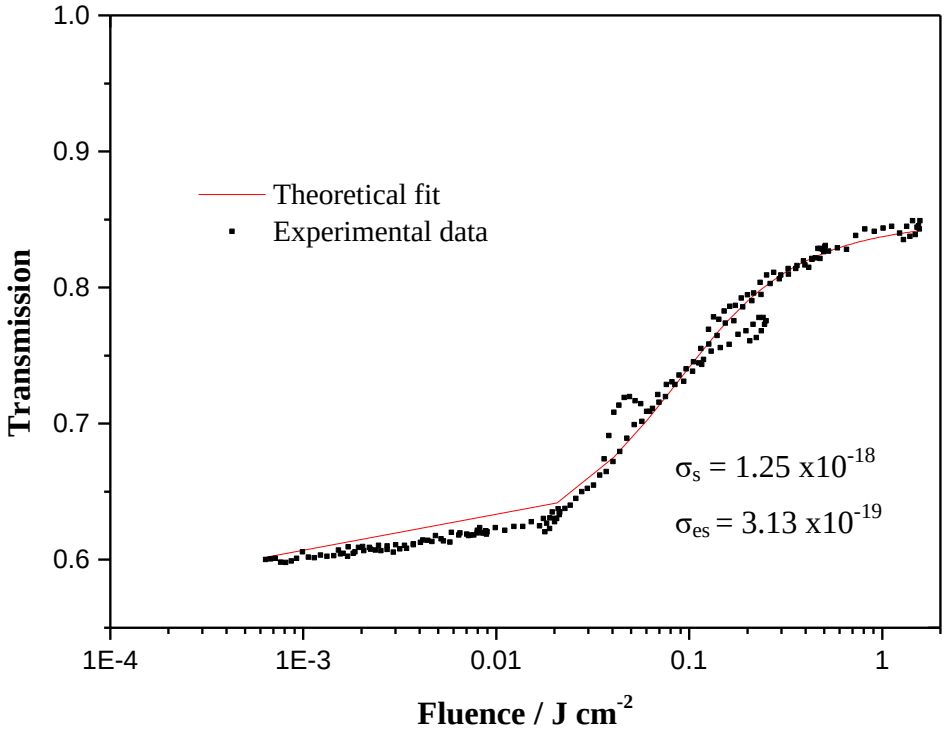

Figure 4.6: Transmission against Fluence for 60 % T_0 V:YAG sample (supplied by Crytur), black dots represent data from the z-scan experiment and the red curve is fitted using the method described in section 4.2.1.3. The ground and excited state absorption cross sections, extracted during the fitting procedure, are presented in the plot area.

4.2.1.4 Absorption cross section results

The absorption cross section values for both materials are presented in Table 4.2, together with values quoted by the manufacturers. The excited state cross section data is unavailable from EKSMA, who supplied the Cr:YAG we used in our experiment. For this reason we have chosen to compare our measured values for the EKSMA sample with values quoted by Crytur for the same material [7]. The V:YAG samples were supplied by Crytur.

The ground and excited state absorption cross section values we calculated are in line with that quoted by the manufacturers, for both materials. The excited state absorption cross section, in both Cr:YAG and V:YAG, was found to be higher in our experiment than is quoted by the manufacturers. This would lead to a higher

saturable loss and, therefore, lower energy Q-switched pulses. Additionally, despite the uncertainty in the measurements of the V:YAG cross sections, the values are similar to the manufactures so we are confident in using our measurements in the modelling later in this chapter.

Table 4.2: Comparison of absorption cross section values of V:YAG and Cr:YAG found during our z-scan experiment and from the manufacturers specifications/literature [7]. β ratio is also presented for easier comparison of potential transmission modulation depth.

	Measured by manufacturer			**Measured results of z-scan**		
	σ_s (10^{-18} cm^2)	σ_{es} (10^{-19} cm^2)	$\beta = \frac{\sigma_{es}}{\sigma_s}$	σ_s (10^{-18} cm^2)	σ_{es} (10^{-19} cm^2)	$\beta = \frac{\sigma_{es}}{\sigma_s}$
V:YAG	1.0	2.2	0.22	1.25	3.1	0.25
Cr:YAG	2.1	1.7	0.081	2.1	3.1	0.15

We are confident that our measurement of the Cr:YAG and V:YAG cross sections are accurate enough to use in our model, particularly since we do not have manufacturers data applicable to the crystal we have used in our experiments. This modelling is described later in section 4.3.2, but first we will outline the experimentally determined laser performance of each passive Q-switch material.

4.3 Passive Q-switching: experimental method and results

This section describes the evaluation of the saturable absorbers samples as high-energy single-pulse passive Q-switches. This was achieved through a comparison of modelled and experimental data. Firstly we will consider the experimental results of passive Q-switching using the 3 materials.

4.3.1 Experimental measurement of Q-switched performance

The following section outlines the experimental measurement of the laser performance using the different passive Q-switch materials, Cr:YAG, BDN and V:YAG. The experimental set up is the same breadboard laser from Chapter 3. A schematic of the apparatus is presented below. The parameters from

Table 4.3 (section 4.3.2) used in the modelling later in this chapter are based on this setup, including cavity length, rod length and diameter, and pump radius.

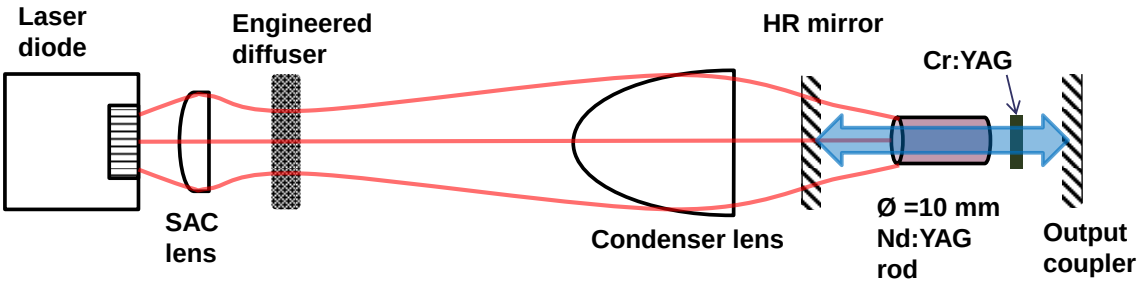

Figure 4.7: Schematic diagram of laser apparatus used in the following experiments. The Cr:YAG is interchangeable with V:YAG and BDN dye. The apparatus is described in full detail in Chapter 3. SAC (Slow axis collimator).

We use the oscilloscope traces of the temporal shape of each pulse to compare, qualitatively, each material in terms of laser performance. The pulse energy and pulse duration give a more quantitative picture on the performance of each material.

4.3.1.1 Experimental comparison of pulse characteristics using Cr:YAG and V:YAG

We begin by looking at the Q-switching measurements using a Cr:YAG Q-switch. An oscilloscope trace is presented in Figure 4.8 showing the pulse train after 200 microseconds of pump time.

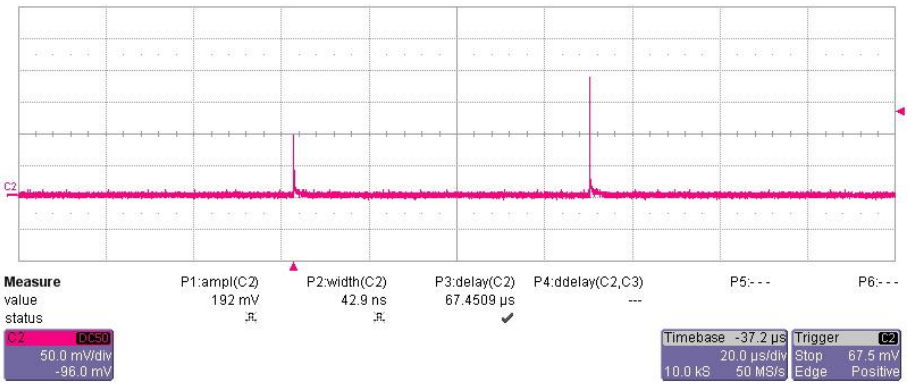

Figure 4.8: Oscilloscope trace of Q-switched output pulse train using a 60 % T_0 Cr:YAG saturable absorber. The total energy contained within both pulses is 50 mJ. Each pulse is 32 ns in duration and is accompanied by a satellite. The pulse width of 32 ns does not include the satellite. Timebase is 20 µs/division. The difference in the pulse amplitudes is caused by the instability of the accompanying satellite peaks, shown in Figure 4.9.

The trace shows two Q-switched pulses emitted during the 200 µs pump cycle. Each pulse is approximately 25 mJ. The pulse duration of each is measured to be 32 ns. It should be noted that by reducing the pump duration, it is possible to produce a single 25 mJ pulse. A close up of a single pulse is presented in Figure 4.9, showing the presence of a satellite pulse.

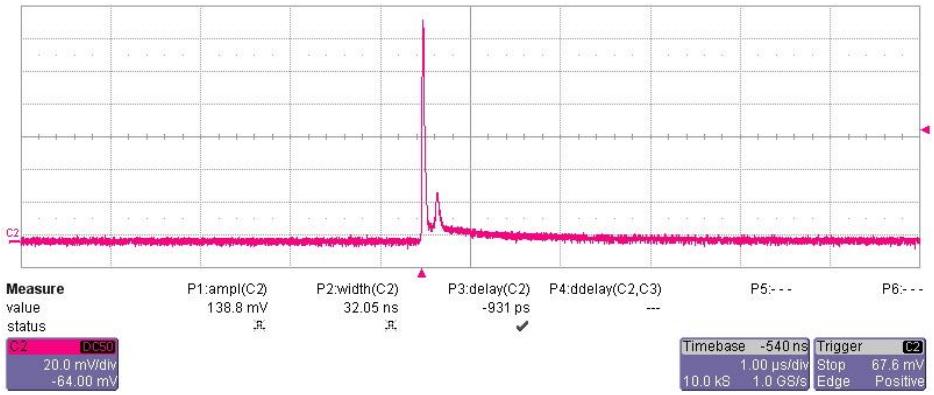

Figure 4.9: Oscilloscope trace of Q-switched output pulse train from Figure 4.10, with adjusted time base to resolve a single Q-switched pulse. A prominent satellite pulse follows the main pulse. Timebase is 1 µs/division.

Next we look at the performance of a V:YAG Q-switch. Presented below are the experimental results from the 60 % T_0 V:YAG Q-switched system.

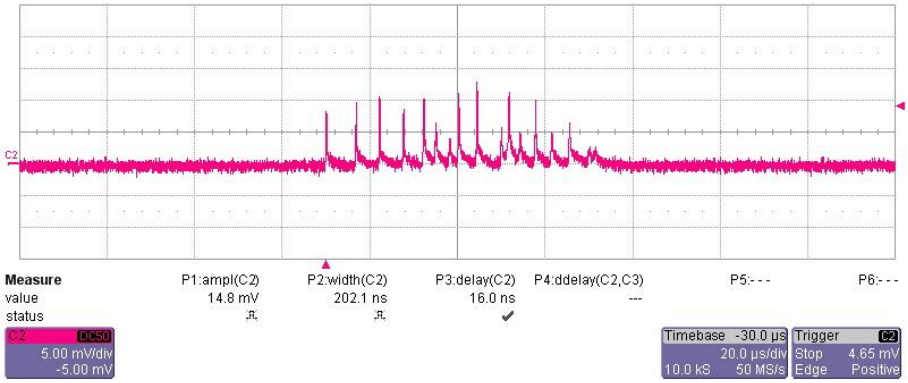

Figure 4.11: Oscilloscope trace of Q-switched output pulse train using a 60 % T_0 V:YAG saturable absorber. The energy contained within the entire pulse train is 2 mJ, and each pulse is 200 ns in duration with no satellites. The entire pulse train lasts approximately 60 µs. Timebase is 20 µs/division.

In Figure 4.11 there are approximately 15-20 Q-switched pulses within a single 200 microsecond pump cycle. This is many more than with Cr:YAG which produced only two pulses. The total energy of the pulse train is 2 mJ, which indicates a single

pulse energy somewhere in the region of 0.1 to 0.2 mJ. Closer inspection of a single pulse is presented below in Figure 4.12, which shows no accompanying satellite.

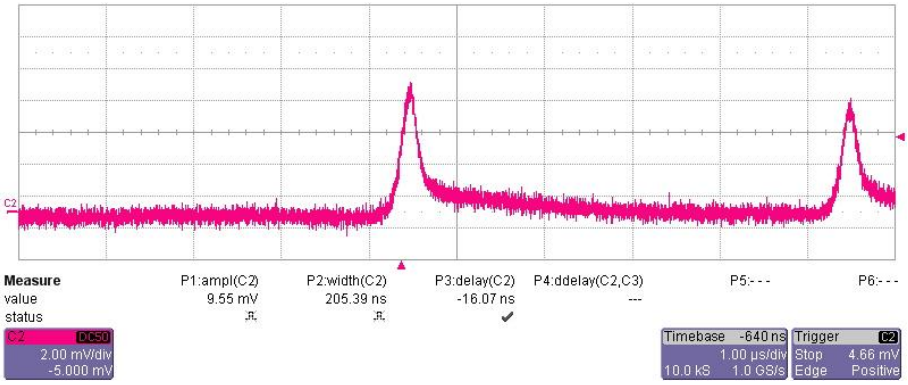

Figure 4.12: Oscilloscope trace of Q-switched output pule train from Figure 4.11, with adjusted time base to resolve a two Q-switched pulses. No satellite pulses are present. Timebase is 1 µs/division.

Despite the presence of the satellite pulse in the Cr:YAG case, it is preferable to V:YAG as a material for high energy passive Q-switching. We have seen that Cr:YAG can be used to produce a single high energy Q-switched pulse, whereas V:YAG produces a pulse train of numerous low energy pulses. For the next section we will compare Cr:YAG with BDN dye.

4.3.1.2 Experimental measurement of pulse characteristics using Cr:YAG and BDN dye

The experimental results from Q-switching with dye and Cr:YAG saturable absorbers are described in the following section. The BDN samples we had available were 51 % T_0, and therefore the performance was compared with a 50 % T_0 Cr:YAG sample. Firstly, we look at the pulse characteristics from a 50 % T_0 Cr:YAG Q-switch, which can be seen below in Figure 4.13. We again see the presence of a satellite pulse. The pulse was measured to have 32 mJ across both the main and satellite pulses, with the main pulse having a 22.5 ns duration.

Presented in Figure 4.14 is the measured oscilloscope trace from the BDN dye Q-switch. It is interesting to see that there is no satellite pulse present in the measured oscilloscope trace of Figure 4.14. The reason for this will be explored using the rate equation model in section 4.3.2.2 (Figure 4.21).

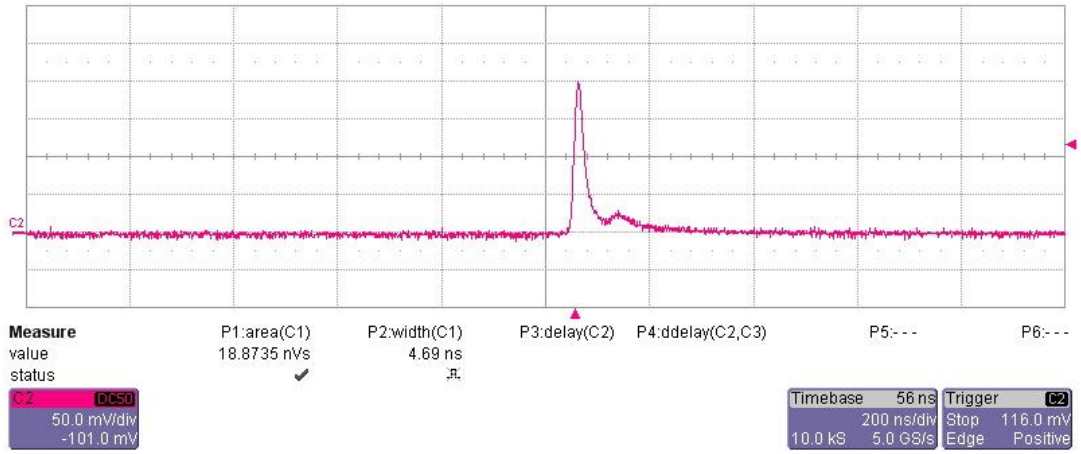

Figure 4.13: Oscilloscope trace of Q-switched pulse using a 50 % T_0 Cr:YAG saturable absorber. The total energy contained within both the primary and satellite pulse is 32 mJ. The FWHM duration of the primary pulse is 22.5 ns, with a clearly visible satellite pulse following. A pump duration of 200 µs resulted in a single Q-switched pulse, with an accompanying satellite. Timebase is 200 ns/division.

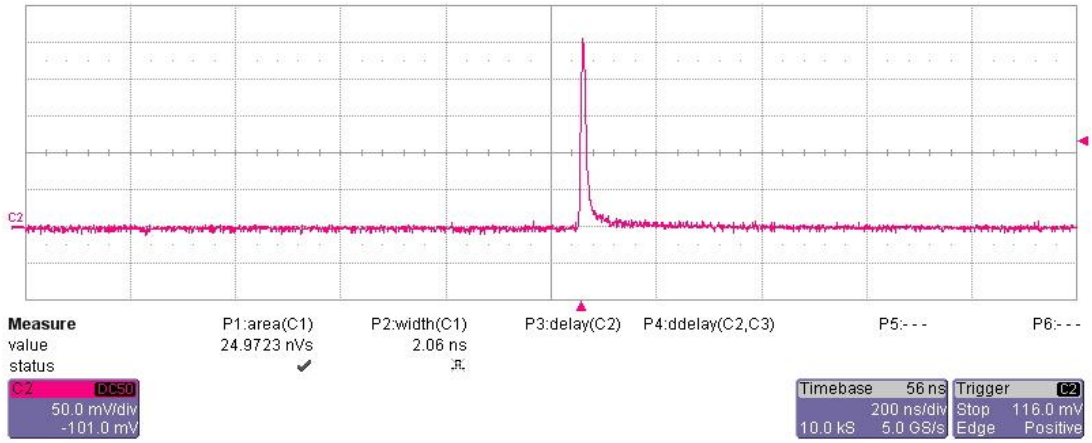

Figure 4.14: Oscilloscope trace of Q-switched pulse using a 51 % T_0 BDN dye saturable absorber. A single pulse, with no accompanying satellite, is observed. The pulse energy is 20 mJ with a FWHM duration of 13 ns. The system was pumped for a duration of 240 µs, resulting in a single Q-switched pulse. Timebase is 200 ns/division.

The energy of the pulse is lower than with the Cr:YAG, at only 20 mJ. At 13 ns the pulse duration was also shorter than the Cr:YAG experiment, which was measured to be 22.5 ns. Another important aspect is that the system was required to be pumped for 240 microseconds before a pulse was produced. Compared to the Cr:YAG experiments, this represents a lower system efficiency and increased power consumption, which is important considering designator systems are generally powered with batteries. The higher threshold is unsurprising, considering that the dye

acetate is uncoated, unlike the crystal Q-switches, which leads to higher loss to overcome before lasing. From these measurements it is clear that Cr:YAG is superior to BDN as a high-energy, passive Q-switch. In the following section we describe the rate equation modelling of passive Q-switch performance for each material, in an attempt to better understand the mechanism responsible for the differences in laser output seen above.

4.3.2 Modelling of Q-switched pulse characteristics

Modelling was carried out using coupled rate equations to allow comparisons of the Q-switched performance of systems using Cr:YAG, V:YAG and BDN dye saturable absorbers. The model, as outlined in Chapter 3, includes a relaxation rate of lower laser level of Nd:YAG of 1 $x10^9$ s^{-1}. Setting this value prevents the generation of a satellite peak in the model, which we concluded in Chapter 3 was not caused by the finite lower laser level. The purpose of the modelling here is to gain a qualitative picture of the performance of each of the Q-switch materials to better understand the experimental results. The model does not consider any high order modes and assumes a homogeneous gain distribution. Additionally, as discussed previously, there is significant uncertainty in the saturable absorber parameters, particularly the absorption cross sections. It is for this reason that we do not expect quantitative agreement between the experimental and modelled data. In this section we are using the rate equation model to help understand, qualitatively, the main features of the Q-switched pulses generated using each of the saturable absorber materials. The following simulated graphs are a result of rate equation modelling described in Chapter 3, and the parameters shown in Table 4.3.

Table 4.3: Parameter values for rate equation modelling. * absorption cross sections are the measured results of the z-scan experiment in Table 4.2

	Model Parameter	Value
λ	Laser wavelength	1064 nm
L	Cavity parasitic loss	1.2 %
R	Output coupler reflectivity	70 %
P_p	Pump power	2800 W
t_p	Pump duration	200 µs
η	Pump coupling efficiency	55 %
ω_p	Pump beam radius	2.5 mm
ω_l	Laser mode radius	2.5 mm
α	Nd:YAG absorption coefficient	1.82 [9]
l_g	Nd:YAG length	5 cm
γ_{21}	Nd:YAG decay rate of 2-1 level	2434.78 s^{-1} [10]
γ_{20}	Nd:YAG decay rate of 2-0 level	1304.35 s^{-1} [10]
γ_{10}	Nd:YAG decay rate of 1-0 level	1 x10^9 s^{-1}
τ_f	Nd:YAG fluorescence	230 µs [10]
σ_g	Nd:YAG stimulated emission cross section	3.8 x10^{-19} cm^2 [9]
κ	Efficiency of spontaneous emission mode coupling	1 x10^{-6} [11]

		Cr:YAG	V:YAG	BDN (Dye)
T_0	Saturable Absorber (SA) initial transmission	50 %, 60 %	60 %	51 %
l_s	Saturable absorber thickness	1.58 mm, 2.12 mm	6.3 mm	0.125 mm
γ_s	SA excited state decay rate	2.44 x10^4 s^{-1} [12]	4.55 x10^7 s^{-1}[7]	1.75 x10^8 s^{-1}[13]
σ_s	SA ground state absorption cross section	*2.1 x10^{-18} cm^2	*1.25 x10^{-18} cm^2	1.0 x10^{-16} cm^2[13]
σ_{es}	SA excited state absorption cross section	*3.13 x10^{-19} cm^2	*3.13 x10^{-19} cm^2	3.0 x10^{-17} cm^2[13]

4.3.2.1 Modelling of Cr:YAG and V:YAG Q-switched pulse characteristics

In this section, we will look at a complete pulse train produced during a 200 µs pump cycle and a close up of a single Q-switched pulse, for both V:YAG and Cr:YAG saturable absorbers, with a comparison of BDN and Cr:YAG following after in section 4.3.2.2. Firstly, we will consider the case of a Cr:YAG passive Q-switch.

Here we present the results of our numerical modelling of a Cr:YAG Q-switch with an initial transmission of 60 %. A pump duration of 200 µs was used, starting at t = 0 µs.

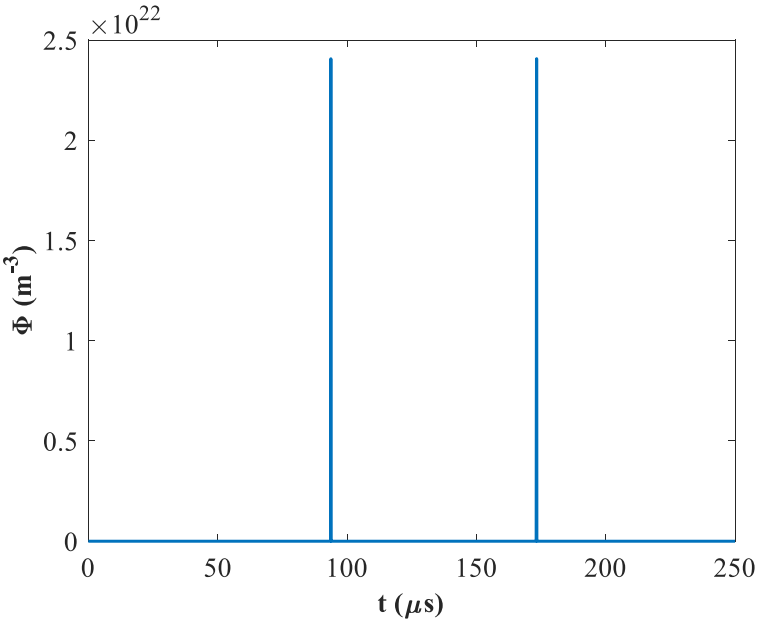

Figure 4.15 Graph showing cavity photon density Φ against time for a numerically simulated Q-switch pulse train during a single 200 µs pump cycle (starting at t = 0), for a 60 % T_0 Cr:YAG saturable absorber. Two pulses are observed during a single pump, each with a FWHM duration of 4.8 ns and a 10-90% energy of 24.4 mJ.

In Figure 4.15 we can see that there are two Q-switched pulses produced during the 200 µs pump cycle. Each pulse contains 24.4 mJ with a FWHM duration of 4.8 ns. If we now consider the different levels in the rate equations we can evaluate how the Q-switching mechanism works.

Presented below in Figure 4.16 are four figures showing the cavity photon density, upper and lower laser level population densities of Nd:YAG, and the ground state population density of Cr:YAG. In the first graph of cavity photon density against time, we see a single pulse with no satellite pulse. As discussed in Chapter 3, we have chosen to supress the satellite pulse by setting the lower laser lifetime of Nd:YAG to 1 x10^{9} s^{-1}, in order to simplify the comparison of modelled results.

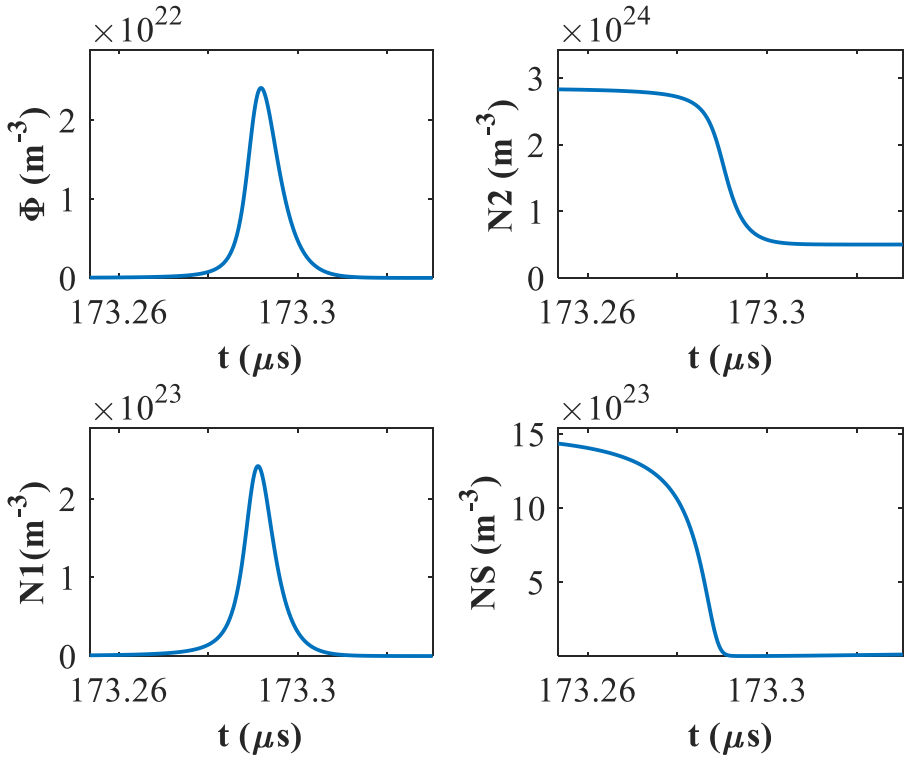

Figure 4.16: Figures showing, from left to right, cavity photon density (Φ), upper laser level population density of Nd:YAG (N2), lower laser level population density of Nd:YAG (N1), and the ground state population density of Cr:YAG (NS). The time scale on each graph is the same.

Considering firstly the population density of the Cr:YAG ground state (NS) over the course of the pulse formation (Φ). The cavity photon density increases rapidly as the Cr:YAG ground state is depopulated by the resonating photons. By 173.29 μs the NS level is almost completely empty as the population shifts into the excited state. At this point the Q-switch remains open for, and longer than, the duration of the Q-switched pulse formation. This allows efficient formation of the Q-switch pulse, without the Q-switch closing duration the pulse formation. We will now move on to apply this rate equation model to a V:YAG Q-switch.

In the case of Figure 4.17, we can see that instead of a single Q-switched pulse we find nearly 100 pulses, spaced approximately 2.5 μs apart, being produced. The pulse amiplitude here is 3 orders of magnitude lower than with Cr:YAG in Figure 4.15. These pulses have a duration of 82.1 ns and are only 0.24 mJ, compared with the 4.8 ns, 24.4 mJ pulses from the Cr:YAG Q-switch.

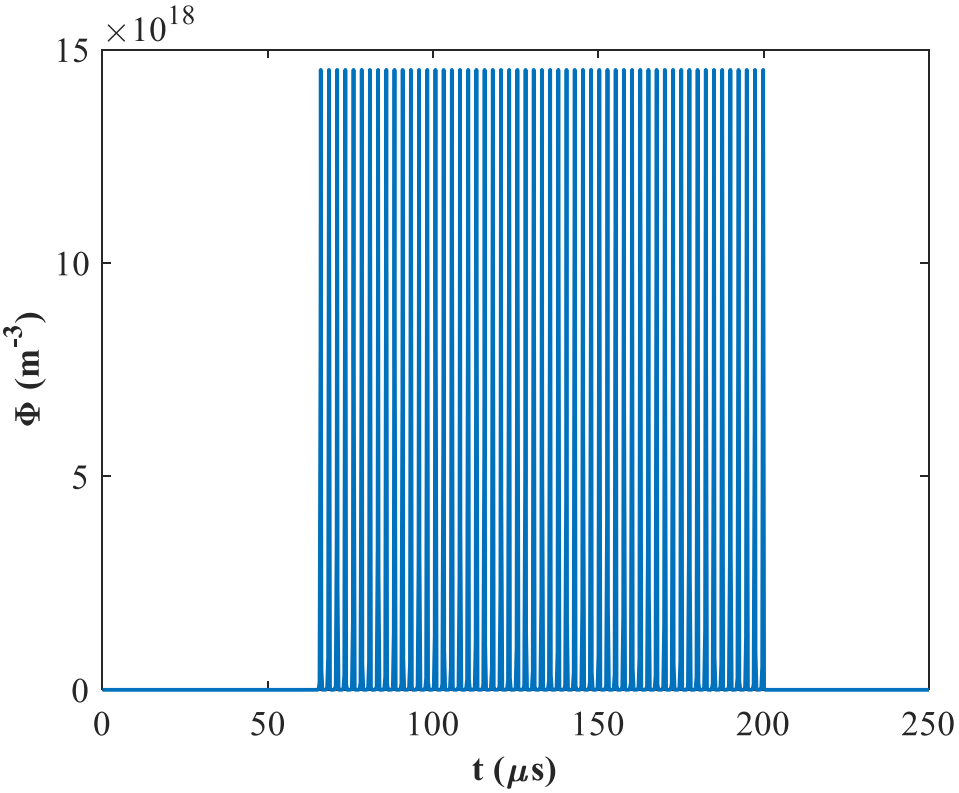

Figure 4.17: Graph showing cavity photon density Φ against time for a numerically simulated Q-switch pulse train during a single 200 μs pump cycle (starting at t = 0), for a 60 % T_0 V:YAG saturable absorber. Close to 100, low amplitude, pulses are observed during a single pump cycle. Pulses are each 82.1 ns in duration and contain 0.24 mJ of energy, with the pulse train totalling 32.0 mJ.

To provide an indication as to why the energy is so low, we can consider the various levels in the rate equation to determine the limitations of using V:YAG, compared with Cr:YAG. This analysis is presented in Figure 4.18.

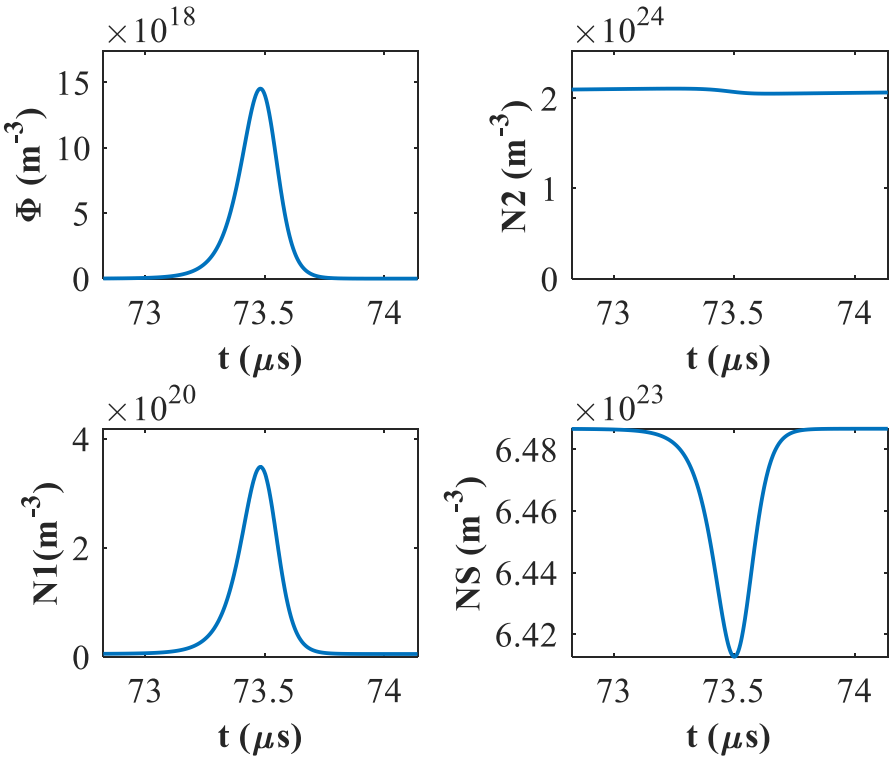

Figure 4.18: Figures showing, from left to right, cavity photon density (Φ), upper laser population density of Nd:YAG (N2), lower laser population density of Nd:YAG (N1), and the ground state population density of V:YAG (NS). The time scales are the same on each graph.

Firstly we will evaluate the occurrence of multiple pulses within a single pump cycle, as seen in Figure 4.17. Looking at Figure 4.18 above, it can be seen from the NS plot that the ground state of the Q-switch does not deplete to zero like the Cr:YAG example. In fact very few atoms in the saturable absorber reach the excited state before they relax back into the ground state NS. This is due to the excited state lifetime of V:YAG (22 ns) being orders of magnitude shorter than Cr:YAG (4 µs). From the N2 plot, we can see that the upper laser level exhibits very little decay, due to stimulated emission, and therefore a relatively small density of cavity photons Φ build up during this period. It is this low density of resonating cavity photons that prevents the V:YAG from becoming appreciably saturated.

From this model we can see that V:YAG does not allow for efficient Q-switching of high energy, low repetition rate, single shot systems, and when compared with Cr:YAG, is not suitable for high energy Q-switching.

4.3.2.2 Modelling of Q-switched pulse characteristics using BDN dye and Cr:YAG

In this section we will evaluate the use of a dye Q-switch against a Cr:YAG saturable absorber crystal. This will allow us to qualitatively evaluate the materials as passive Q-switches for high energy pulse generation at 1 micron. The parameters used in the model are presented in section 4.3.2.

First we present the model results from the 50 % T_0 Cr:YAG saturable absorber, to later compare against the 51 % T_0 BDN sample. Figure 4.19 shows the cavity photon density against time for the Cr:YAG absorber. Only a single Q-switched pulse is produced during the 200 microsecond pump time.

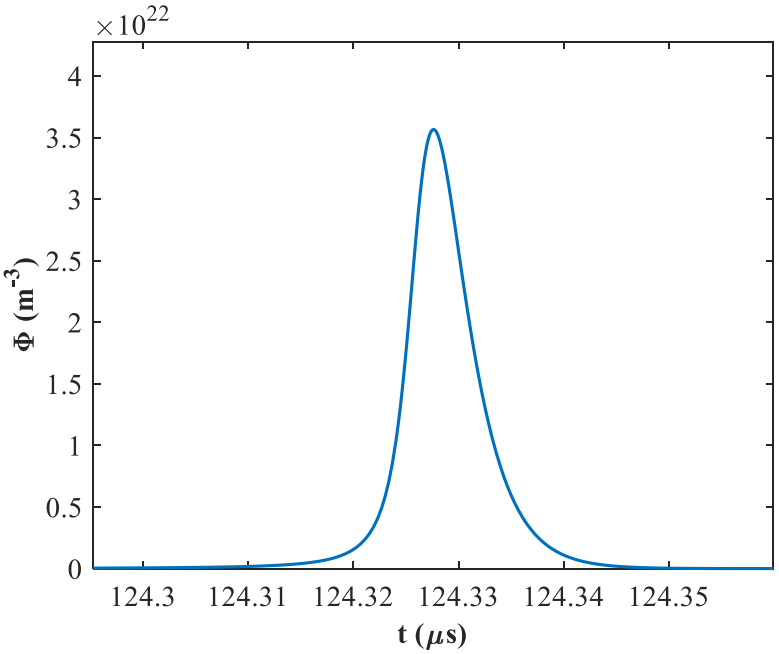

Figure 4.19: Numerically simulated Q-switched pulse during a single 150 µs pump cycle, for a 50 % T_0 Cr:YAG saturable absorber. The pulse has a FWHM duration of 4.0 ns duration and a 10-90% energy of 30.5 mJ.

Here we have a single Q-switched pulse with an energy of 30.5 mJ and duration of 4.0 ns, from a Cr:YAG absorber with an initial transmission of 50 %. Looking now to the dye example in Figure 4.20, we can compare the pulse charateristics.

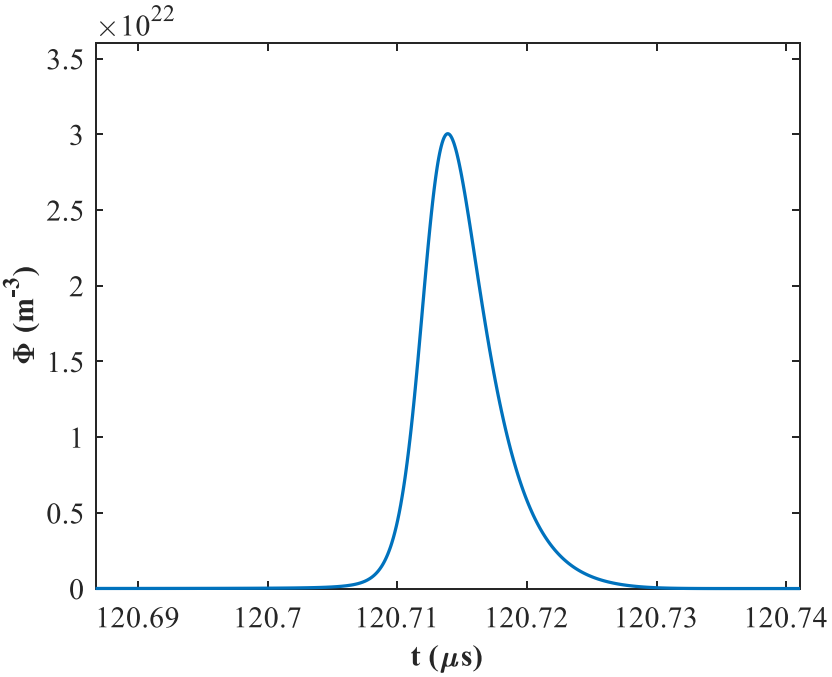

Figure 4.20: Numerically simulated Q-switch pulse during a single 150 µs pump cycle, for a 51 % T_0 Kodak 15064 DYE saturable absorber. The main pulse has a FWHM duration of 3.4 ns duration and a 10-90 % energy of 22.4 mJ.

The duration and energy of the pulses are 3.4 ns and 22.4 mJ, respectively, which are both lower than the Cr:YAG example. The most significant differences, in terms of the model parameters, between the Cr:YAG and dye are the decay rate of the excited state and the absorption cross sections. The dye has an excited state lifetime of 5.7 ns, compared to the 4 µs lifetime of Cr:YAG. BDN has a ground and excited-state absorption cross section of 1 x 10^{-16}cm^2 and 3 x 10^{-17}cm^2, respectively. If we now consider the individual levels in the rate equation we can evaluate how this affects the decay kinetics.

The first thing to glean from Figure 4.21 is that the graph of NS against time shows that the Q-switch opens completely as the cavity photon density Φ begins to build appreciably at 120.72 µs. Due to the ground state absorption cross section being very high (1 x 10^{-16} cm^2), the ground state of the absorber NS is depleted rapidly and completely as the atoms move to the excited state. This ensures that the Q-switch opens rapidly and fully, and the N2 level (i.e. upper laser-level) is depleted sufficiently through stimulated emission before the Q-switch returns to its initial transmission state.

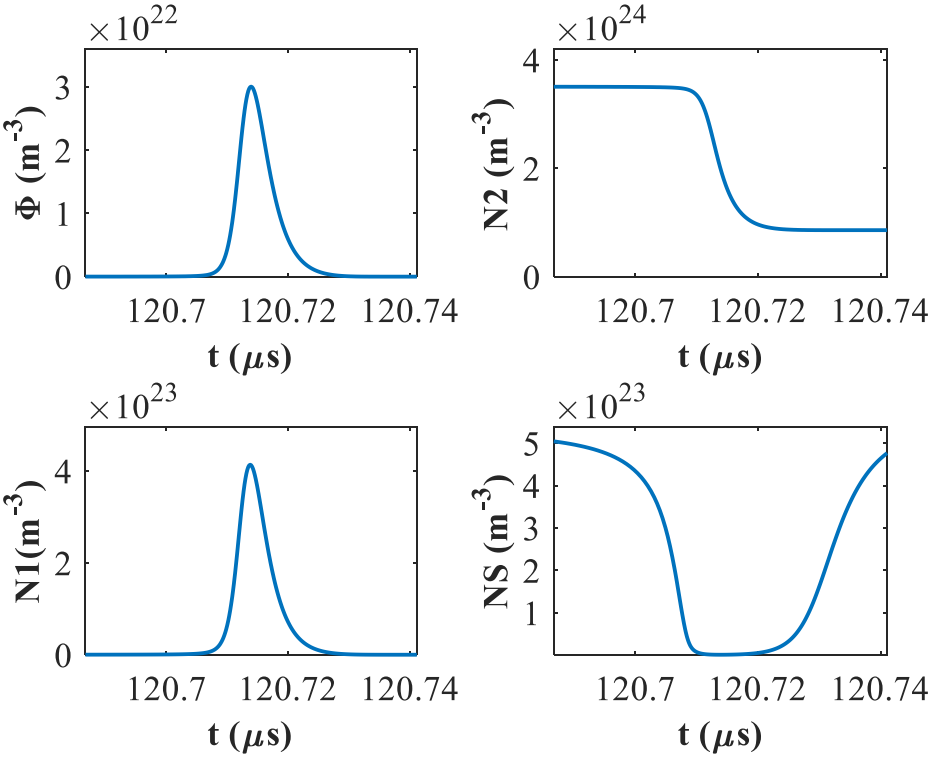

Figure 4.21: Figures showing, from left to right, cavity photon density (Φ), upper laser population density of Nd:YAG (N2), lower laser population density of Nd:YAG (N1), and the ground state population density of BDN (NS). The time scale on each graph is the same.

This allows an appreciable cavity photon density Φ to build up during this time, which in turn ensures the Q-switch is becomes fully saturated. The saturable absorber does, however, close during the stimulated emission of the N2 level, due to the short lifetime of the N2 excited state (5.7 ns). As seen in the V:YAG case in Figure 4.18, this limits how much energy is emitted in a single pulse, although to a lesser extent here than with V:YAG. We can also speculate as to why the satellite peak observed during the Cr:YAG experiment (Figure 4.13) was not seen in the BDN oscilloscope trace (Figure 4.14). This can be explained by considering the population of the saturable absorber ground state. At the point where a satellite pulse would be expected to be produced (approximately 50 ns after the primary pulse), the population of the excited state depletes due to the fast decay time of the absorber. The Q-switch is essentially closing too early to allow the production of a satellite pulse.

To summarise, the high ground state absorption cross section of BDN allows a significant pulse to be formed before the excited state of the saturable absorber

relaxes (with a lifetime of 5.7 ns). Unfortunately the excited state lifetime of BDN is too short and reduces the efficiency by 20 %, compared with Cr:YAG. The high excited state absorption cross section causes the saturated transmission to be relatively low at 82 %. This in turn causes the cavity decay lifetime to be very short, at 0.4 ns, thus allowing the resulting pulse duration to be as short as we see here, at 3.4 ns. It also has the negative effect of reducing the pulse energy achieved by introducing an increased non-saturable loss, compared with the Cr:YAG scenario which has a much higher saturated transmission of 97.5 %.

Below we present a table summarising the pulse energy and duration for all cases, both measured and simulated. This will assist in forming conclusions on the suitability of each absorber material.

Table 4.4: Comparison of measured and simulated pulse energy and duration for Cr:YAG, BDN and V:YAG.

Material (T_0)	Measured		Simulated	
	Energy (mJ)	Pulse duration (ns)	Energy (mJ)	Pulse duration (ns)
Cr:YAG (60%)	25.0	32	24.4	4.8
V:YAG (60%)	0.2	200	0.24	82.1
Cr:YAG (50%)	32	22.5	30.5	4.0
BDN (51%)	20	13	22.4	3.4

We found generally good agreement with the modelled and measured pulse energy. With pulse duration the measured value is always many times longer than the modelled result. This could potentially be a result of an underestimate of intracavity losses (not associated with the saturable absorber). Additionally, the model is a simplified case with no consideration of transverse mode structure of the Q-switched pulse or spatial profile of the pump, which will no doubt lead to discrepancies between modelled and measured pulse durations.

4.4 Discussion and conclusions

It was the purpose of this chapter to evaluate the suitability of available saturable absorber materials for application in laser target designators. From a material perspective we are looking predominantly for the ability to produce high energy pulses, ideally above 50 mJ.

Firstly, we investigated the variation in absorption parameters for Cr:YAG and V:YAG crystals. We found that the values quoted by manufacturers, and measurements from literature, can vary by orders of magnitude. For this reason we set up a z-scan experiment to determine the excited and ground state absorption cross sections of a Cr:YAG and V:YAG sample. The transmission of a Q-switched pulse through each material was measured for a range of incident beam fluence values, and S-shaped plots of transmission versus fluence were produced for V:YAG and Cr:YAG. We presented a theoretical model, which was then fitted by eye to the experimental data to extract the material parameters of the samples. By manually changing the ground and excited state cross sections of each material, we were able to achieve a visually good fit to the data.

The experiment and analysis was more successful for the Cr:YAG crystal than for V:YAG due to the later sample being many times thicker than the Rayleigh length of the measurement laser. However, our measured cross section values for both crystals fell in line with those reported by the manufacturers. It would be useful in the future to perform a z-scan measurement on more samples purchased from the manufacturer, to evaluate the variation in absorption cross section. This would allow laser production tolerances to be set to cater for this variation in material parameters.

Using a breadboard laser setup and laser rate equation modelling, we were able to assess how each of the materials would perform in the context of high energy Q-switching. From both the modelling and experimental results, we found that V:YAG is an unsuitable saturable absorber for our application of laser designators. When considering only the absorption cross sections of Cr:YAG and V:YAG, it would seem that the performance would be similar. However, from both modelling and experiment, we found that the V:YAG produces a pulse train of numerous low energy pulses. This is because the short lifetime of the excited state (22 ns) prevents

the upper laser level from fully depleting, through stimulated emission, to a sufficient level for high energy pulses production, before the Q-switch closes. This is unsuitable for laser target designators, since a single pulse energy of above 50 mJ would be unachievable.

The Q-switched performance of BDN (bis[4-dimethylaminodithiobenzil] nickel) dye [3] was then compared against that of the Cr:YAG system. This has been a reliable Q-switch used in many military applications, with its main drawback being its relatively poor component durability, especially when compared with Cr:YAG crystals. From our experiment we found that a BDN Q-switch with a 51 % initial transmission would produce a single pulse energy of 20 mJ and a duration of 13 ns; compared to that of the 50 % (T_0) Cr:YAG sample, with an energy of 32 mJ and duration of 22.5 ns. From modelling we predicted that the same BDN Q-switch (51 % T_0) would produce a single pulse energy of 22.4 mJ and a duration of 3.4 ns. We can conclude that despite the short excited state lifetime of BDN (2.9 ns), a substantial single Q-switched pulse is produced. This is because the ground state absorption of BDN is sufficiently high to allow the Q-switch to remain open long enough for the upper laser level to deplete appreciably.

So, following from our investigation of alternative saturable absorbers, we conclude that Cr:YAG is still the best available material for higher energy applications.

4.5 References

[1] G. Xiao, J. Lim, and S. Yang, “Z-scan measurement of the ground and excited state absorption cross sections of Cr4+ in yttrium aluminum garnet,” *IEEE J. Quantum Electron.*, vol. 35, no. 7, pp. 1086–1091, 1999.

[2] D. Hull, “Combination laser Q-switch using a spinning mirror and saturable dye.,” *Appl. Opt.*, vol. 5, no. 8, pp. 1342–3, 1966.

[3] Z. F. Zhu and E. M. Garmire, “Papers: Optical Bistability in BDN Dye,” *IEEE J. Quantum Electron.*, vol. 19, no. 10, pp. 1495–1498, 1983.

[4] J. Chen, H. Kung, H. Yau, H. Llu, T. Chen, and C. Cheng, “Passive Q-switches for Nd : hosted Solid State Lasers,” *Opt. Rev.*, vol. 7, no. 6, pp. 511–

519, 2000.

[5] R. Feldman, Y. Shimony, and Z. Burshtein, “Passive Q-switching in Nd:YAG/Cr4+:YAG monolithic microchip laser,” *Opt. Mater. (Amst).*, vol. 24, no. 1–2, pp. 393–399, 2003.

[6] B. Lipavsky, Y. Kalisky, Z. Burshtein, Y. Shimony, and S. Rotman, “Some optical properties of Cr4+-doped crystals,” *Opt. Mater. (Amst).*, vol. 13, no. 1, pp. 117–127, 1999.

[7] J. Šulc and P. Arátor, “Solid state saturable absorbers for Q-switching at 1 and 1.3 μm: investigation and modeling,” *Proc. SPIE*, vol. 6871, p. 68712D–68712D–11, 2008.

[8] T. Xia, D. J. Hagan, A. Dogariu, A. A. Said, and E. W. Van Stryland, “Optimization of optical limiting devices based on excited-state absorption.,” *Appl. Opt.*, vol. 36, no. 18, pp. 4110–22, 1997.

[9] Crytur, “Laser rods - Neodymium doped,” *Nd:YAG laser material properties*, 2017. [Online]. Available: https://www.crytur.cz/products/laser-rods-neodymium-doped/. [Accessed: 08-May-2017].

[10] W. Koechner, *Solid-State Laser Engineering*. New York: Springer, 2006.

[11] C. J. Mercer, Y. H. Tsang, and D. J. Binks, “A model of a QCW diode pumped passively Q- switched solid state laser,” *J. Mod. Opt.*, vol. 54, no. 12, pp. 1685–1694, 2007.

[12] J. Dong, “Numerical modeling of CW-pumped repetitively passively Q-switched Yb:YAG lasers with Cr:YAG as saturable absorber,” *Opt. Commun.*, vol. 226, no. 1–6, pp. 337–344, 2003.

[13] Y. S. Choi, “Saturation Characteristics of Cr(4)+:YAG Crystals and Dye Films for Passive Q Switches.,” *Appl. Opt.*, vol. 40, no. 30, pp. 5417–22, 2001.

Chapter 5 Thermal performance of a Cr:YAG passively Q-switched 1 µs laser

5.1 Introduction

A crucial aspect of military laser systems is the ability to function in the most extreme conditions. Owing to the fact that a passively Q-switched system has fewer moving parts, we are confident that mechanical shocks and vibrations could be mitigated through practiced engineering techniques already used for actively Q-switched systems. The thermal performance of a passively Q-switched system is more of a concern, as it is largely unknown how the entire system will behave over a broad temperature range. In this chapter we have experimentally investigated how our system will behave with changes in ambient temperatures, and how this compares to theoretical predictions based on individual mechanisms. The mechanisms under investigation are based around three components, the pump laser, Nd:YAG gain crystal and Cr:YAG saturable absorber. We will assess the temperature driven mechanisms present in each of these areas and how they are likely to affect the entire system over changes in ambient temperature.

5.1.1 Military specifications explained

The specifications as outlined in STANAG 3733 [1] include pulse energy and timing jitter requirements. These requirements must be met over a broad temperature range, -40 to +70 °C, to meet the requirements for military applications. This is why it is vital to perform temperature testing. For STANAG compliance the energy must remain above 50 mJ per pulse and the jitter must remain below 5 µs, over the entire temperature range.

We assess the function of the entire laser throughout the temperature range. We attempt to explain the temperature variations observed during the experiment by modelling the behaviour of the individual components that are known to have a

temperature dependent mechanism. This can direct further investigations and optimisation of the performance of our passively Q-switched system over temperature. We are only concerned with effects associated with ambient temperature changes, not those resulting from self-heating by the pump beam. In our experiments, the laser is running at very low repetition rate (2 Hz) and is therefore in a regime where self-heating can be considered negligible.

5.1.1.1 Potential problems

There are five key components that we believe affect most significantly the temperature performance of the laser, they are:

1. Nd:YAG gain region.

The stimulated emission cross-section in Nd:YAG is known to vary over temperature [2].

2. Laser diode pump.

There are two mechanisms that can vary with temperature: the temperature tuning of the output wavelength, and the change in output power with temperature. The diode power will affect the rate at which the Nd:YAG inversion is created, and also the diode wavelength has a direct impact on the absorption in the Nd:YAG rod. We will analyse both mechanisms in this chapter. There are additional thermal issues concerning the pump mechanism, for instance thermal lensing. We will not consider thermal lensing in our evaluation as this is a result of thermal loading by the pump absorption, rather than ambient temperature changes. In a 2 Hz system with a pump duration of 200 µs we assume the thermal lens is very weak [3].

3. The Cr:YAG Q-switch material.

We also consider the absorption and excited state decay rate of Cr:YAG and how they are likely to affect the output parameters over the specified temperature range.

4. Gain/ laser mode overlap.

Another mechanism which will affect the laser performance is the laser mode size, and the overlap with the pump beam. The poorer the overlap between the laser mode and pump beam, the less efficient the laser, which leads to longer pump times before threshold. Conversely, a larger laser mode size allows a greater volume of the gain

region to be energised, and therefore higher energy pulses would result. It seems feasible that the overlap could change with temperature. We do not consider a particular mechanism for the change, but instead use it later in the chapter as a free parameter in the models. This allows us to change it and assess what affect it could have on the laser performance.

5. Mechanical misalignment of the laser cavity optics.

Lastly, mechanical instability has already been identified in Chapter 3 as an issue which can greatly affect the output of the laser. Although some effects of mechanical misalignment are removed due to the design of the resonator, as described later in this chapter (section 5.3.1), it is clear from the results (section 5.3.3) that misalignment is still an issue. Our modelling is not capable of including these effects. As a result, we optimise the laser output at each temperature point above room temperature in order to remove effects due to mechanical misalignment. It was not possible to optimise the laser alignment at temperatures below room temperature, and hence we were unable to ensure that the misalignment was minimised at low temperatures. This will be discussed in greater detail in the results section (section 5.3.3).

5.1.1.2 Temperature testing from literature

A previous study by T. Dascalu and N. Pavel (2009) [4], investigated the change in laser parameters at high temperatures (between 20 °C and 150 °C). This was also based on an Nd:YAG system Q-switched by Cr:YAG (initial transmission $T_0 = 60$ %) with single pulse energy of 0.78 mJ and a pulse duration of 5.6 ns. This is a significantly more compact system than ours with a resonator length of 60 mm. It should also be noted that the pump system was not included in the oven, so all the results of this experiment to do not factor in temperature variations of the pump beam or its effect of the laser (i.e. absorption). They found that there were no significant changes in the pulse energy or threshold pump energy below 100 °C. Above 100 °C however, variations in pulse energy were observed and attributed to fluctuations in the resonator configuration and the stimulated emission cross section of Nd:YAG over temperature. A maximum pulse energy of 1.1 mJ was achieved at a

temperature of 150 °C. No change in the pulse duration or variation in the initial transmission of the Cr:YAG crystal was observed.

It is our intention to build on the findings by T. Dascalu and N. Pavel, to extend the experiment down to lower temperatures, and for a higher energy system, as well as investigate each temperature dependent material parameter through modelling. With this we can conclude where the most significant issues lie with regards to ambient temperature fluctuations in a passively Q-switched system. We will discuss the required theory for modelling, the experimental method and finally the comparison of modelled and experimental results. From this we can draw conclusions on the suitability of a passively Q-switched system within the military requirements for temperature, set out in STANAG 3733. We have a purpose built chassis to house our laser system, which we will call the *X-model* in order to differentiate it from the previous work on the *breadboard* setup.

5.2 Theory

We look at the inherent material properties of the Nd:YAG and Cr:YAG to model any temperature driven variation. As mentioned above, we have minimised the effect of mechanical misalignment, and as a result, we do not consider mirror alignment in the theory.

In terms of the Nd:YAG laser rod, there are two relevant properties that are known to vary over temperature. These are the effective emission cross section of the laser level (σ_g) and the variation of the absorption coefficient of Nd:YAG due to the temperature variation of the diode laser pump wavelength. In sections 5.2.1 and 5.2.2 each of these will be discussed in turn.

5.2.1 Effective stimulated emission cross-section of Nd:YAG

The temperature dependence of the effective stimulated emission cross section of Nd:YAG is due to the thermally driven redistribution of population between the two sub-levels within the $^4F_{3/2}$ laser manifold, as presented below in Figure 5.1.

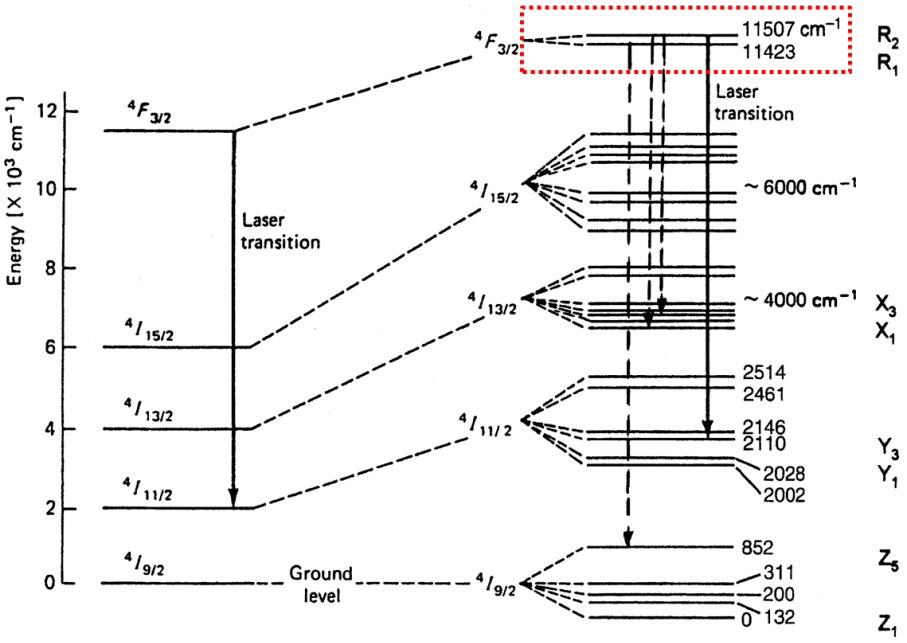

Figure 5.1: Energy level diagram of Nd:YAG showing Stark splitting of the energy manifolds of the upper laser level, highlighted in red [3]. The 1064 nm laser emission is a result of $^4F_{3/2}$ to $^4I_{11/2}$ transition, which subsequently terminates by non-radiative relaxation into the $^4I_{9/2}$ ground level.

The population of the $^4F_{3/2}$ manifold is spread across the two sublevels according to a Boltzmann distribution, leading to a temperature dependence of population of the individual sub-levels. Each of the sub-levels has a different stimulated cross section, so the resulting effective cross section is a population-weighted average of the two levels. As the temperature affects the Boltzmann distribution of the population density of each level, the effective cross section is a weighted average of the two levels at each temperature. The result, as experimentally determined by A. Rapaport et. al. [2], is a linear temperature dependence of the effective cross section of Nd:YAG. The linear equation is an adapted version of that presented by A. Rapaport et. al. 2002, and is as follows:

$$\sigma_g = (3.87 - 3.7x10^{-3}\,T) * 1x10^{-23}, \qquad \text{Equation 5.1}$$

where, $\sigma_g$is the effective stimulated emission cross section of Nd:YAG in m^2 and T is the temperature in °C. The y-intercept of the equation has been increased from 2.35 $x10^{-23}$, as measured by Rapaport, to 3.87 $x10^{-23}$ so that the value at 20 °C matches that of the Crytur Nd:YAG crystal specifications [5] (3.8 $x10^{-23}$ m^2). It

should be noted that Crytur manufactured the Nd:YAG crystal used in our experiments.

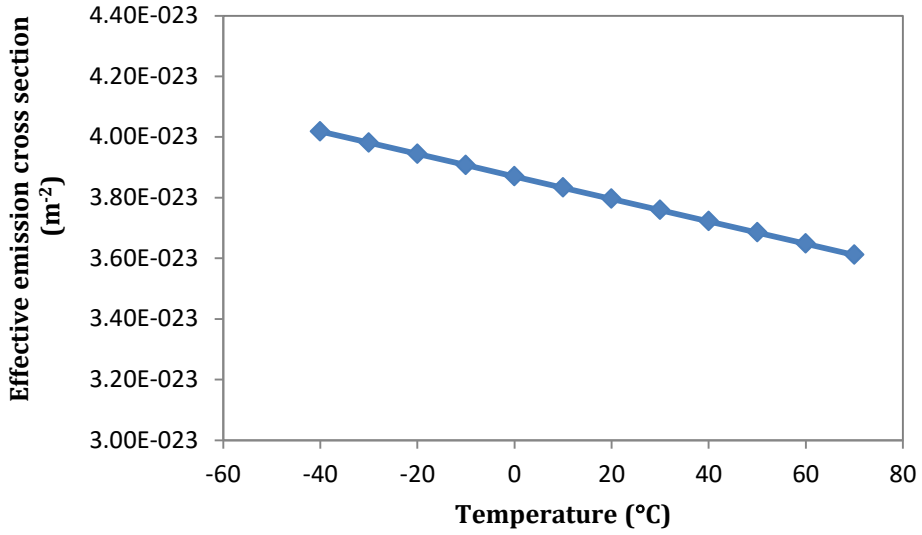

Figure 5.2: Plot of the effective cross section of Nd:YAG against temperature in degrees Celsius. The data points are calculated using Equation 5.1.

This function is then inserted into our rate equation model to assess the impact of a temperature dependent effective stimulated emission cross section on the output parameters of the X-model laser.

5.2.2 Absorption coefficient of Nd:YAG

The other variation in the system which is driven by temperature variations is the wavelength of the pump diode laser output. The pump wavelength varies at an estimated 0.3 nm $°C^{-1}$ [3], which over the required temperature range (-40 to +70 °C) results in a total estimated wavelength shift of 33 nm [6] (from 791.9 to 824.9 nm). Coupled with the spectral variation in the Nd:YAG absorption characteristics, we can derive a temperature variation of the pump absorption coefficient of Nd:YAG. The absorption spectrum of Nd:YAG, taken from the Crytur online catalogue [5], has been presented previously in Figure 1.8.

According to this absorption data, between 791 nm and 824 nm, the maximum variation in absorption coefficient is between 0.424 cm^{-1} and 7.56 cm^{-1}. The diode we are using has a linewidth of 2.8 nm, which will flatten out the peaks and troughs of the absorption profile. As a result, using Figure 1.8 as the absorption

profile our modelling is more strict than necessary, giving wider variations in absorption coefficient that in reality. Whilst not completely accurate, this gives us a good indication of how the temperature fluctuations in the diode wavelength will affect the performance of our laser in the worst case. The rate equation model can be evaluated for increments between these values. The resulting laser output parameters will allow the influence of the Nd:YAG absorption over temperature to be assessed. In the data which we present in the experimental results section, it should be noted that it is not evaluated for specific temperature values, but rather over the range of absorption coefficient values that are likely to be observed over the operating temperature range (0.424 cm^{-1} to 7.56 cm^{-1}).

5.2.3 Excited state decay rate of Cr:YAG

When considering the properties of a saturable absorber crystal, the three most important material specifications are: the decay rate of the excited state (γ_s), and both the excited (σ_{es}) and ground state (σ_s) absorption cross sections [7]. For an ideal absorber the excited state absorption would be zero. The ratio $\beta = \frac{\sigma_{es}}{\sigma_s}$ provides a figure of merit for a non-ideal saturable absorber [8]. A lower value of β represents a more efficient passive Q-switch. Whilst it affects the laser output parameters greatly, it isn't generally possible to select or guarantee what the value of β from actual Cr:YAG samples. In fact, the measured absorption values not only vary between manufacturers but also between growth runs. It cannot be assumed that a sample is of a certain absorption value unless it has been measured for that particular growth run. This is a result in the uncertainty of the concentration of tetrahedraly oriented Cr^{4+} ions formed by the addition of a codopant (commonly Ca^{2+})[9][10]. It is for this reason that we have adjusted the absorption value to achieve a reasonable fit to our modelling at the starting temperature of 20 °C.

Whilst we have varied the absorption values to allow reasonable fit of the data at 20 °C, we do not vary them over temperature. This is due to evidence by Xiao et. al. 1999 [10], that both the ground and excited state absorption cross sections do not change over a temperature range of -60 to +98 °C.

The decay rate of the excited state of Cr:YAG does, however, vary with temperature, and it is therefore important to explore this in our model. We have extracted data from a figure in Kück et. al. [11] to describe the relationship between temperature and the lifetime of the excited state of Cr:YAG. The data was extracted from the figure using *WebPlotDigitizer* digitisation software. The resulting relationship is presented below, note that the temperature is displayed in degrees Kelvin.

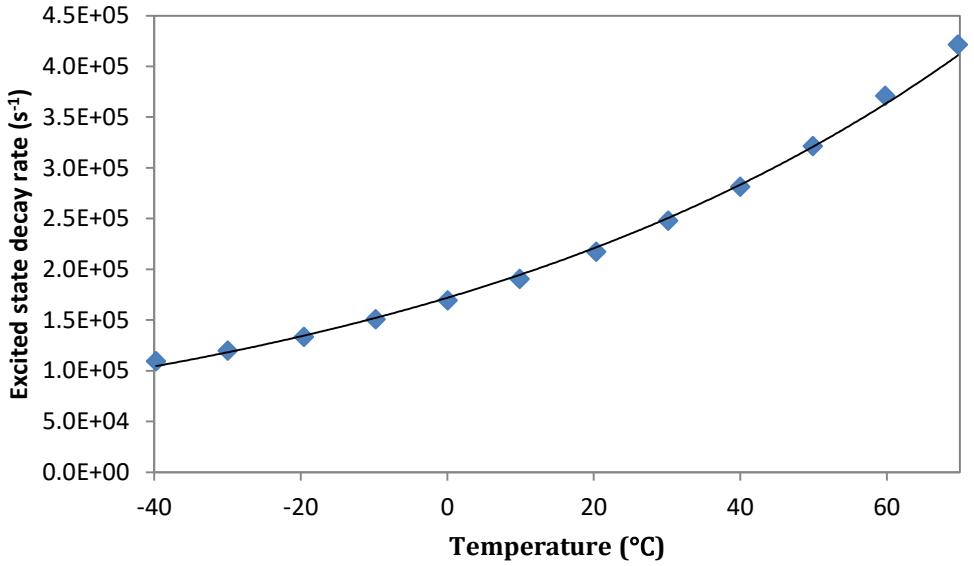

Figure 5.3: Graph of the excited state decay rate against temperature in °C for Cr:YAG. Data is extracted from Figure 7e in Kück et. al. [11]. A least squares exponential fit was made in Excel to obtain an equation to be used in the rate equation model.

In order to use the data from Figure 5.3 in our rate equation model, we needed to obtain an equation for the relationship. This was carried out using a least squares exponential fit in Microsoft Excel. The resulting equation is as follows:

$$\gamma_s = 566.3\, e^{0.0125 \cdot T}, \qquad \text{Equation 5.2}$$

where γ_s is the rate of decay of the excited state in s^{-1} and T is the temperature in °C. The resulting temperature dependence of each parameter outlined above can then be inserted into the rate equation model to assess how the entire system behaves over temperature. The rate equation model was introduced previously in Chapter 3.

5.2.4 Diode laser power fluctuations with temperature

It is well know that the efficiency of diode lasers varies with temperature [12],[13]. However, data from the supplier (DILAS) on the pump module we use in the X-model was limited. As a result, we use data from another supplier (Quantel) that produce stacks of a similar type, and assume that the DILAS lasers should be similar, given that it is of a similar material, design and wavelength. Quantel provided data for the temperature dependence of a single diode bar which we assume is similar for the diode stack and scale up the diode power to reach 3kW at room temperature. The resultant variation of the pump power with temperature is shown in Figure 5.4.

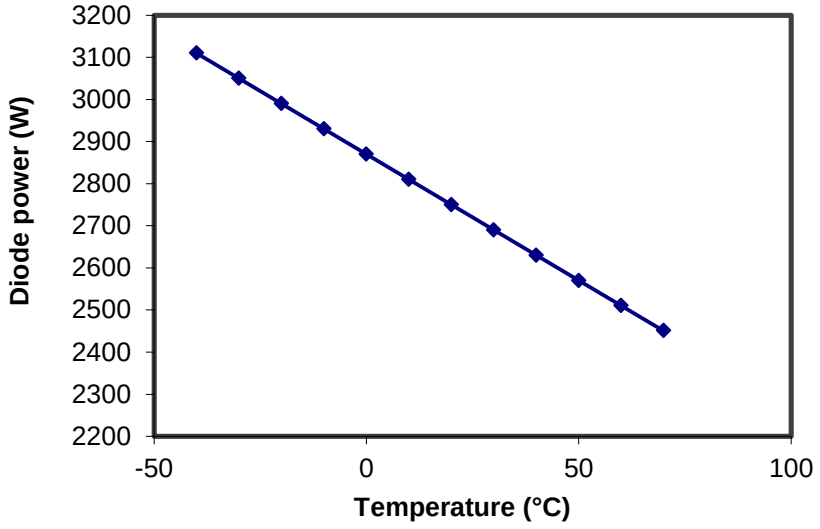

Figure 5.4: Quantel 12 bar Diode stack output power against ambient temperature.

With this data, we can now apply the relationship between pump power and temperature to our model to assess the impact on the laser performance.

5.2.5 Laser mode size and pump beam overlap efficiency.

In our laser rate equations, outlined in Chapter 3, we have identified that the mode size is relevant in the calculation of the pulse energy, but is not included in the solution of the rate equations themselves.

The equation we have used for calculating the pulse energy, as reported by Dong. J. et. al [14], is presented below:

$$E = \frac{h\nu A l'}{t_r}\left(\frac{1}{R}\right)\int_0^\infty \phi(t)dt\,, \qquad \text{Equation 5.3}$$

where l' is the optical length of the cavity in m, A is the laser mode area in m^2, $\int_0^\infty \phi(t)dt$ is the cavity photon density integrated over the duration of the pulse, t_r is the cavity round trip time in s, and R is the output coupler reflectivity.

From Equation 5.3, we can see that an increase in the mode size (A) will lead to an equivalent increase in the output energy, with all other parameters held constant.

5.3 Experimental method and results

To assess the function of a laser system over a temperature range there are two aspects that are important to consider. Firstly, all of the relevant components have to be contained within a solid chassis, to allow testing of the device as a whole. We have labelled this laser the X-model build. Secondly, a suitable thermal testing chamber is required to be able to house the laser and reach the target temperatures. These two aspects will be discussed in sections 5.3.1 and 5.3.2, respectively.

5.3.1 X-model – mechanically stable passively Q-switched laser

Here we shall consider the X-model design and how it aids with the temperature testing process. Below we present a photograph (Figure 5.5) and schematic of the X-model laser (Figure 5.6), and a schematic illustrating the pump coupling scheme (Figure 5.7) in further detail.

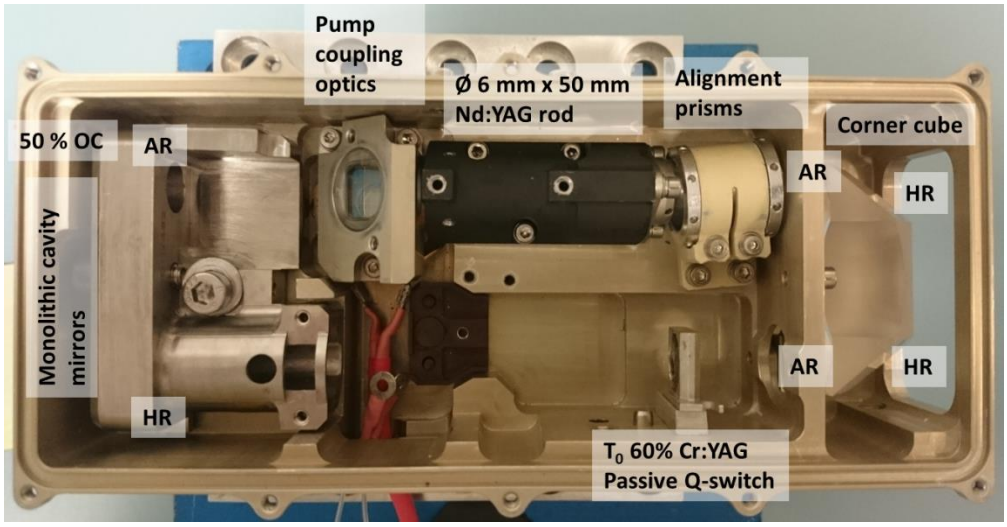

Figure 5.5: Top-down view photograph of X-model laser components inside the chassis. The pump diode is positioned beneath the pump coupling optics and is not visible in this photograph.

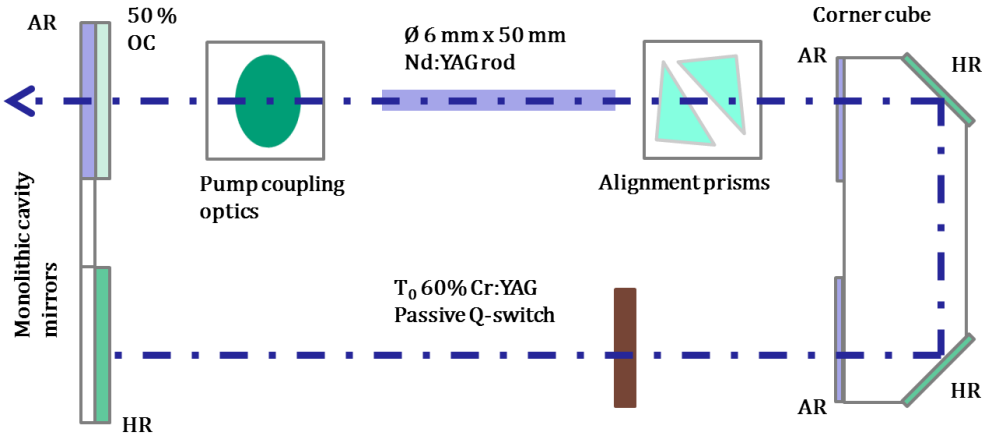

Figure 5.6: Schematic diagram of X-model components within the chassis. The top-down view is analogous to the photograph in Figure 5.5.

The X-model system comprises the usual laser components described in previous chapters, with three significant variations unique to this chapter. Firstly, we have a monolithic cavity mirror, situated on the far left of both Figure 5.5 and Figure 5.6. During the process of taking a laser system over such a large temperature range, it is certain that the components will move relative to one another. This is due to the difference in the thermal expansion coefficient of each material throughout the cavity. This can potentially cause misalignment of the laser during the thermal testing process. With a monolithic laser mirror, made from a homogenous piece of

glass, we should not experience any movement of the high reflectivity mirror and output coupler, relative to each other. For a folded cavity such as this, a retro-reflecting corner cube is placed at the fold to ensure the beams in the two arms of the resonator remain parallel through the turn.

The corner cube can be seen on the far right hand side of both Figure 5.5 and Figure 5.6. When used in tandem with the monolithic HR/OC mirror, any movement of these components during heating, results in the beam path being maintained well within the constraints of each optical component. This is because the angle of the beam incident on the corner cube does not change relative to the outgoing beam [15][16]. Provided that the mirrors retain a constant position relative to each other, the laser will remain insensitive to the alignment of the individual laser components during temperature testing. However, the likelihood of the laser becoming misaligned and dropping below threshold is increased if distortion of the mirrors occurs.

So, despite these design features, we found it necessary to realign the laser using the steering wedges at each temperature from 20 – 70 °C, in order to optimise the performance. It was not possible to optimise the alignment at temperatures below 20 °C, so these data points are not as reliable as those above room temperature. Although, the effect of thermally induced misalignment appeared to be less significant at temperatures lower than 20 °C. We will consider this further in section 5.3.3.

Another interesting characteristic of the X-model system is the positioning of the pump coupling optics. The pump diode laser is positioned beneath the laser cavity and coupled using a triangular prism with dielectric coatings. This is illustrated below in Figure 5.7.

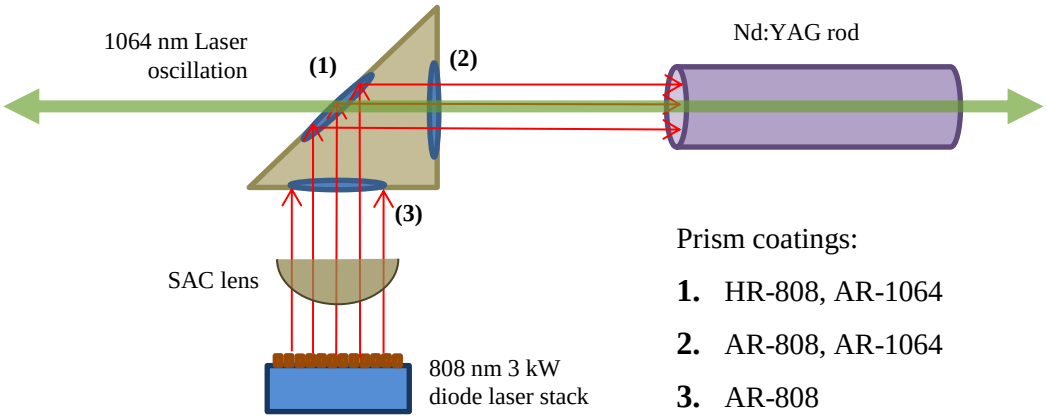

Figure 5.7: Cross sectional schematic diagram of pump-coupling optics within X-model. Anti-reflection (AR) and High-reflection (HR) coatings are displayed as blue ellipses, with the corresponding affected wavelengths described in the legend.

The total distance from the diode emitter to the Nd:YAG rod facet is 34.6 mm, the distance from the emitter to the cylindrical slow-axis-collimator (SAC) lens is 3.7 mm and the focal length of the lens is 30 mm. The pump beam size is taken to be the size of the emitter (11 x 4.7 mm) and the divergence angles (full angle), as specified by the manufacturer, are 6° in the slow axis, and 4.4° in the fast axis (including integrated fast axis collimation). Using ABCD matrix software, and the above values, we calculated the pump beam incident on the rod to be 3.13 mm x 2.52 mm. From the beam profile provided by DILAS, presented below in Figure 5.8, we have approximated that the beam is a top hat profile and rectangular cross section. The rod has a circular face which is 6 mm in diameter. From this we have calculated a geometric pump coupling efficiency of 89 %. This value is the geometric overlap of the pump beam at the rod face and does not consider divergence within the laser rod. In summary, we are QCW pumping the rod at a power of 3 kW for between 80 and 170 µs, at an estimated energy transfer efficiency of 89 %. This information is used in all of our rate equation modelling throughout this chapter.

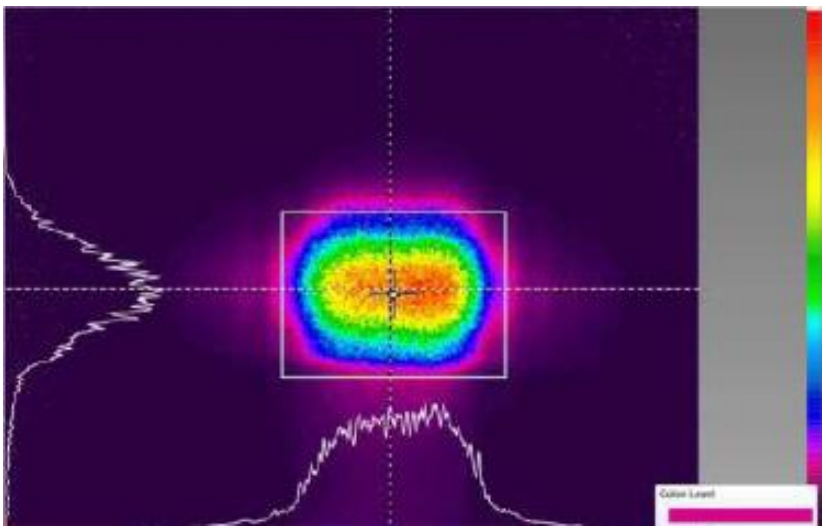

Figure 5.8: CCD camera image of pump diode stack, 50 mm from the emitter. Image is provided by DILAS.

5.3.2 Thermal chamber

For thermal testing, the sealed X-model unit was placed inside a thermal chamber. A photograph of the equipment is presented below in Figure 5.9. The sealed X-model casing can be seen in the centre of the photograph, on top of an adjustable concertina stand. A thermocouple, which is connected to a meter in the bottom right hand side of the photograph, is used to track the temperature of the X-model casing. Dry air is pumped into the chamber to prevent condensation at cold temperatures. There is a transparent (AR coated at 1064nm) window on the left side of the chamber to allow the laser output to be measured outside of the chamber. Dry air is also directed towards the transparent window to prevent condensation affecting the laser pulse measurements.

The first measurement is taken with the oven set to 20 °C, and both sources of dry air turned on. Once the oven reaches the set temperature, according to the oven controls, we add a further dwell time of 60 minutes to ensure the laser components also reach this temperature. The thermocouple temperature after 60 minutes provides an accurate representation of the X-model temperature, and is noted as the temperature of the system during the analysis.

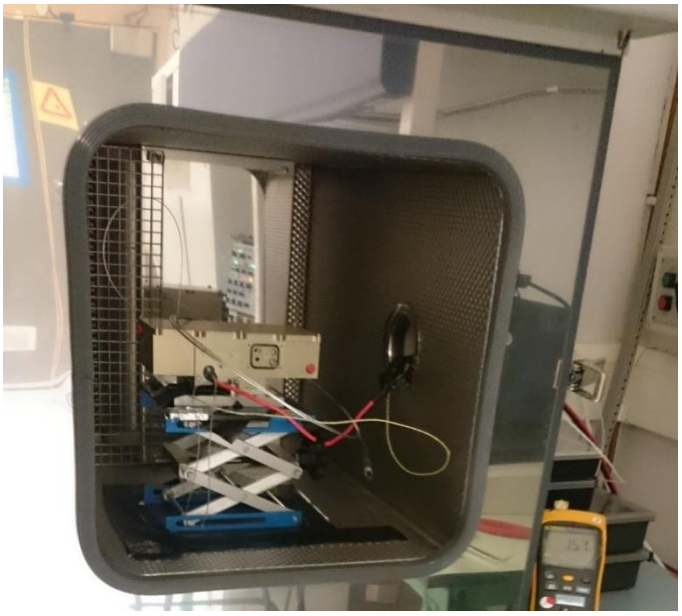

Figure 5.9: Photograph of sealed X-model laser housed within thermal testing chamber. The thermocouple cable is pictured entering the chamber in the centre-right of the photograph. Thermocouple meter is pictured in yellow at the bottom right of the photograph.

We then measure the output beam properties. An Ophir pyroelectric energy sensor and meter is used to measure the single pulse energy. A silicon fast photodiode is used, in conjunction with a LeCroy Waverunner oscilloscope, to measure the temporal properties of the pulse. This includes the output pulse duration, timing jitter and threshold pump duration. As described previously, the timing jitter is defined by STANAG 3733 as the maximum fluctuation in the duration between subsequent single output pulses. We define the threshold pump duration as the amount of time (in microseconds) that the system requires to be pumped before Q-switched output is observed. The above parameters, except the pulse duration, are measured in unison over 500 pulses and an average taken for reporting in the results section below. Measurement of the pulse duration required an increased resolution of the oscilloscope time-base, which meant that it was measured over 100 shots separately from the other parameters. The divergence of the output beam is also measured separately using a Spiricon CCD camera with Beamgauge software. The beam is directed through ND filters and onto a focusing mirror of 760 mm focal length. This focuses the beam onto the Spiricon camera detector (with integrated protective ND filters). By inputting the focal length of the mirror into the software,

the divergence of the output beam is measured. This is known as the focal length method [17].

Once all of these parameters are measured, the oven is then set to 30 °C. The oven is again allowed to dwell at 30 °C for 60 minutes to allow the components to reach this temperature. At this point the oven door is opened and the alignment prisms adjusted to the new optimal position. The adjustment seeks to minimise the pump time, and hence maximise the efficiency of the laser, as was used during the initial set-up of the laser. This is required due to mechanical misalignment of the laser mirrors, which we believe is caused by bending of the monolithic mirror during heating. This is a non-ideal situation which we were unable to solve within the scope of this project. The method for realignment relies on monitoring the Q-switched output using the Silicon fast photodiode and oscilloscope. By minimising the delay between the start of the pumping cycle and Q-switched output, we can reach an optimised alignment during adjustment of the rotating prisms. During this alignment, the temperature as measured by the thermocouple does not change by more than 1 °C. At this point the unit is resealed and the oven door closed for another 30 minutes to ensure the components have reached the desired temperature once again. The mirror alignment optimisation was only carried out from +20 °C to +70 °C, due to not being able to open the oven door below room temperature. For this reason the extent of mechanical instability at lower temperatures is unknown. Despite this, we measured the laser parameters described above at each 10 °C interval from -40 °C to +70° C, to then analyse and compare it with our modelled data.

5.3.3 Experimental results

In the following section, we present the results of the temperature analysis described above. Firstly, we will display and analyse the data from our experiments in the thermal chamber. Then, in the following section, we will show the results of the corresponding theoretical models, based on the temperature variation in laser parameters described in the previous section. These theoretical values and trends will be compared with our experimental results to attempt to diagnose the temperature dependent mechanisms involved.

Presented below are the experimental results of the thermal testing outlined in the previous section. The quoted temperature values are as measured by the thermocouple inside the thermal chamber. Firstly, we present the single Q-switched pulse energy against temperature.

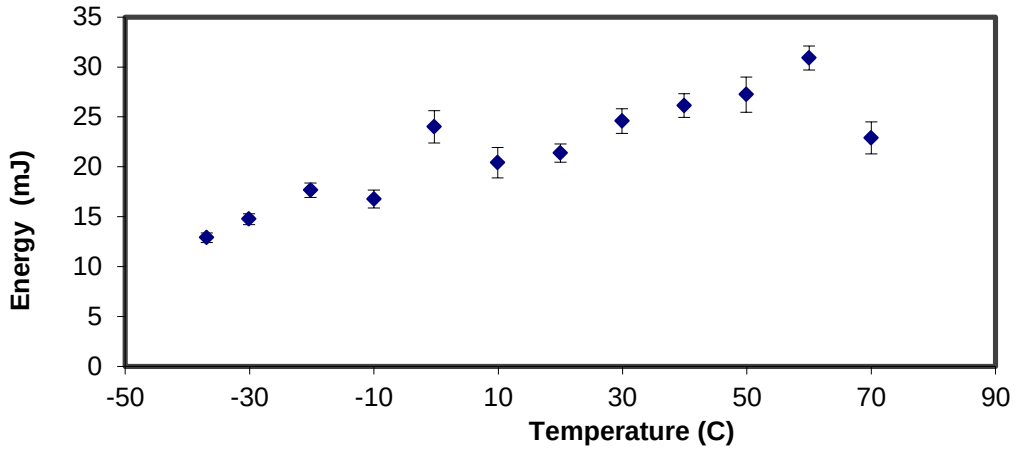

Figure 5.10: Experimental results of single Q-switched pulse energy against temperature. The energy values are an average of 500 pulses, with the corresponding errors being the standard deviation.

The data shows a steady increase in pulse energy with temperature, with the exception of at 70 °C. The experimental datum at 70 °C can be considered a point of high mechanical instability, resulting in failure to align the laser mirrors to the same precision as the previous data points. The mirror alignment optimisation at this point becomes more difficult as the laser is more sensitive to mirror adjustments, compared with lower temperatures.

Presented below, in Figure 5.11, is the threshold pump duration against temperature. In this case we describe the threshold pump duration to be the time between the start of the pump pulse and the point at which the Q-switched pulse is produced. This is measured as the time between the 50 % point on the rising edge of the pump and Q-switched pulse oscilloscope traces, as detected by the pump driver current probe and a fast photodiode, respectively.

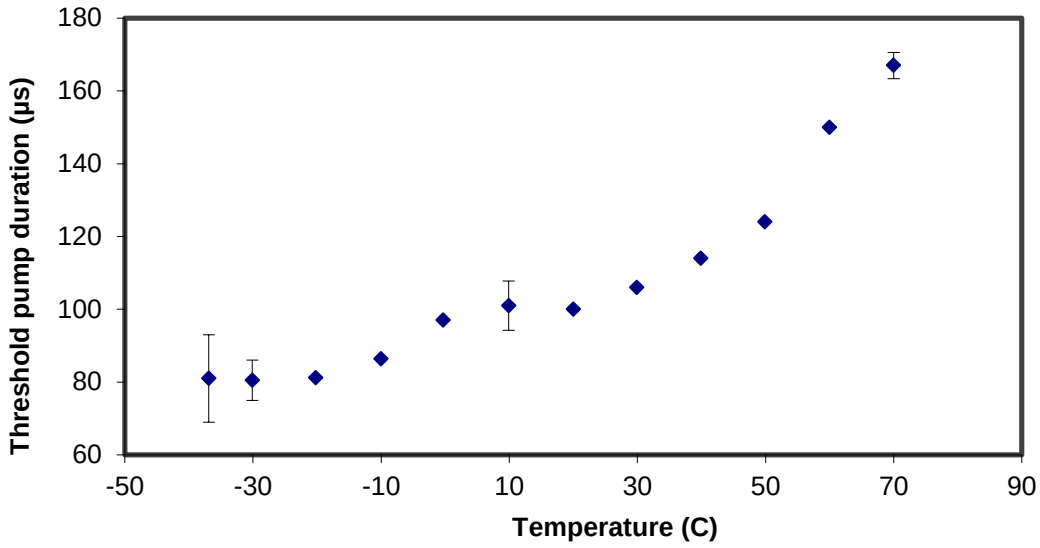

Figure 5.11: Experimental results of threshold pump duration against temperature. The threshold values are an average of 500 pulses, with the corresponding errors being the standard deviation.

The first thing to note from Figure 5.11 is that the threshold pump duration follows a similar trajectory to the energy in Figure 5.10. This follows the accepted Q-switching theory that an increase in pump duration, in the absence of an increased parasitic cavity loss, would lead to an increase in stored energy and therefore output energy [7]. We will explore this mechanism further in the following sections in which we evaluate the thermal variation of the effective cross section of Nd:YAG. At 60°C and 70 °C we see a notable increase in the threshold pump duration above the preceding trend at -40 °C to 50 °C. This is consistent with the drop in energy seen at 70 °C where we believe that an increase in parasitic losses, due to not being able to fully compensate for mirror misalignment, has led to an increase in the threshold pump duration. The gradient of the graph is relatively shallow at lower temperatures (< 20 °C), for which mirror realignment was not possible. This indicates that the effects of thermally induced mirror misalignment are not as pronounced at lower temperatures.

We now present the max-min pulse timing jitter against temperature in Figure 5.12. The jitter is defined as the maximum fluctuation of the pulse-to-pulse timing, as described in Chapter 3.

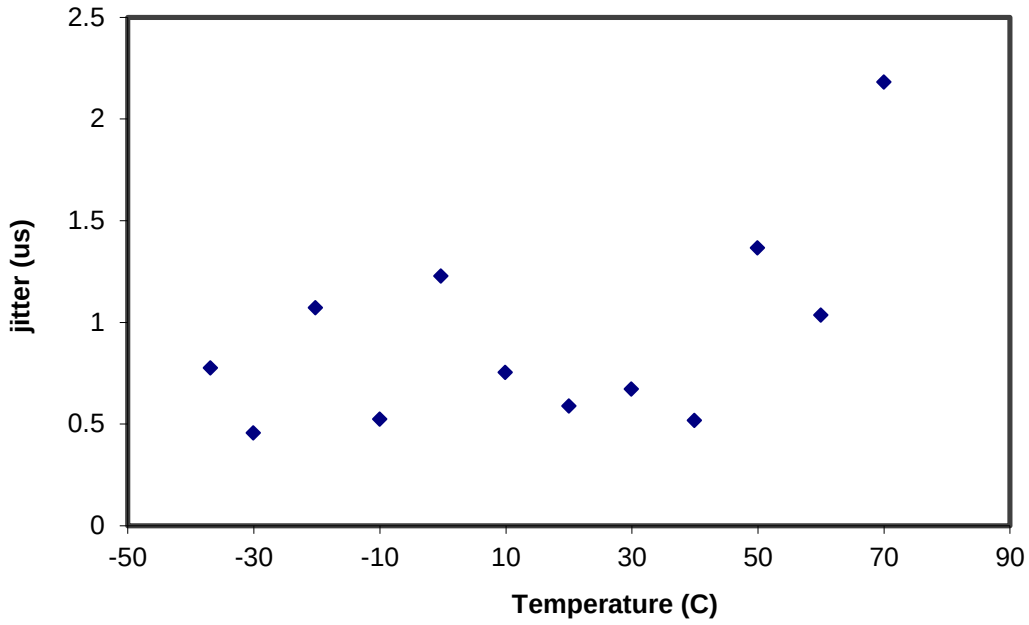

Figure 5.12: Experimental results of pulse-to-pulse jitter against temperature. The jitter is calculated as the max-min values of 500 pulses, with no errors displayed.

Crucially, the jitter value remains well within the STANAG specification of 5 µs throughout the full temperature range. Promisingly it remains largely within the preferred performance of 2µs, with the exception of the measurement at 70 °C. Although the jitter is likely to increase with a higher energy system, assuming that jitter scales linearly with energy, this should still remain below 5 µs in a >50 mJ system over the temperature range. It should be noted that, similar to the energy and threshold measurements previously described (Figure 5.10 and Figure 5.11, respectively), the jitter is significantly higher at 70 °C. This again is most likely due to non-optimal mirror alignment at this temperature. This leads to a higher gain required and hence longer pump time. We have seen previously in chapter 3 that the jitter will be higher in this case. We can see in Figure 5.12 that there does not appear to be a significant trend between jitter and temperature. The jitter data may show a small increase with temperature, but it is not strong enough to attempt to evaluate the mechanism behind it.

Finally, we present the experimental results of the Q-switched pulse duration against temperature in Figure 5.13.

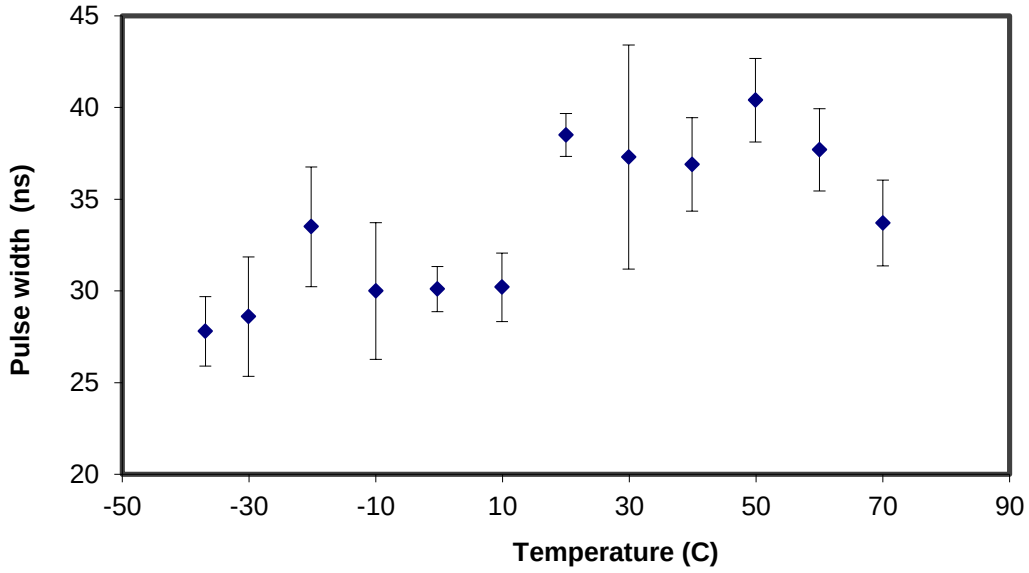

Figure 5.13: Experimental results of single Q-switch pulse duration against temperature. The pulse width is an average of 100 pulses, measured separately from the other parameters. The corresponding errors are the standard deviation.

The other laser parameters were measured with a lower resolution oscilloscope time-base to allow both the pump and Q-switched pulse to be simultaneously resolved. Measurement of the Q-switched pulse duration required a greater resolution time-base. For this reason, the pulse duration was measured separately from energy, threshold and jitter. The presented values (figure 13) are therefore an average of 100 pulses, recorded with a higher resolution time-base. The displayed errors are the standard deviation of these 100 pulses. Again we see an increase in pulse duration over temperature, varying between 28 and 40 ns. When considering the size of the errors it is possible that there is no trend at all, and the variation is a result of the non-optimal mirror alignment.

In the following section the theoretically modelled results will be evaluated in an attempt to explain any trends found during the thermal testing experiments.

5.3.4 Rate equation modelling results

In the following sections we present the results of our rate equation modelling, described in Section 5.2. We use the value of the ground state absorption found on the MT-Berlin (who manufactured our Cr:YAG sample) catalogue page, which is 5 $x10^{-18}$ cm^{-2}. The excited state absorption cross section was not available, so we varied this value until we achieved a reasonable agreement with the measured pulse duration and energy at 20 °C. We are comfortable with this adjustment because we are only looking at qualitative temperature trends rather than absolute agreement. The rate equation parameters are given in Table 5.1.

Table 5.1: Rate equation model parameters for X-model thermal test simulation. All parameters denoted with * are subject to temperature variations as part of this chapter.

Symbol	Model Parameter	Value
λ	Laser wavelength	1064 nm
L	Cavity parasitic loss	4.4 % (12x AR surfaces)
R	Output coupler reflectivity	50 %
P_p	Pump power	*2800 W
t_p	Pump duration	*200 µs
η	Pump coupling efficiency	89 %
ω_p	Pump beam radius	3 mm (see note below)
ω_l	Laser mode radius	*3mm
α	Nd:YAG absorption coefficient	*1.82 [5]
l_g	Nd:YAG length	5 cm
γ_{21}	Nd:YAG decay rate of 2-1 level	2434.78 s^{-1} [3]
γ_{20}	Nd:YAG decay rate of 2-0 level	1304.35 s^{-1} [3]
γ_{10}	Nd:YAG decay rate of 1-0 level	1 $x10^{9}$ s^{-1}
τ_f	Nd:YAG fluorescence lifetime	230 µs [3]
σ_g	Nd:YAG stimulated emission cross section	*3.8 $x10^{-19}$ cm^2 [5][18]
κ	Efficiency of spontaneous emission mode coupling	1 $x10^{-6}$ [19]
		Cr:YAG
T_0	Saturable Absorber (SA) initial transmission	60 %
l_s	Saturable absorber thickness	1.83 mm
γ_s	SA excited state decay rate	*2.94 $x10^{4}$ s^{-1} [11][20]
σ_s	SA ground state absorption cross section	5 $x10^{-18}$ cm^2 [21]
σ_{es}	SA excited state cross section	2.95 $x10^{-18}$ cm^2

It should also be noted that the pump beam radius is set equal to the laser rod radius in this case, despite the fact the pump overlaps the rod face. This discrepancy is instead handled in the rate equations by the pump overlap efficiency term η as described previously in section 5.3.1. This ensures a more accurate representation of pump absorption.

Now we will evaluate the impact of changing stimulated emission cross section in Nd:YAG on the output of the rate equation model.

5.3.4.1 Temperature dependence of the effective emission cross section of Nd:YAG

Presented in this section are the computational and experimental results of the temperature testing of the X-model laser. In this section, the computationally modelled points are achieved as a function of temperature using the temperature dependence of the effective emission cross section of Nd:YAG [18], as described in section 5.2.1. The resulting output pulse energy is presented as a function of temperature below in Figure 5.14. The experimental data points are shown as blue diamonds, with all computationally obtained points as red squares.

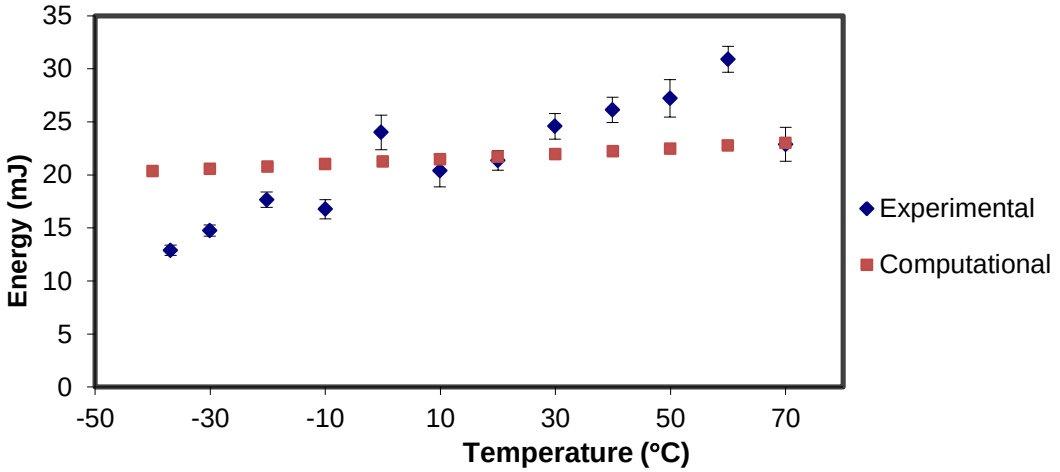

Figure 5.14: Experimental and computational results of output energy as a function of temperature. Results are obtained by investigating the temperature dependence of the effective stimulated emission cross section of Nd:YAG. Experimental data points are denoted by blue diamonds and the corresponding computational points by red squares.

Both the model and experimental data show an increase in energy with increasing temperature. The gradient of the upwards trend is much shallower for the theoretical

model. From this modelling we can conclude that the change in the effective emission cross section with temperature is not sufficient to describe the change in Q-switched pulse energy. This indicates that additional mechanisms must be affecting the pulse energy, which will be handled in the proceeding sections.

The next modelled parameter to consider is the threshold pump duration. The experimental verification, together with the modelled results, is presented below in Figure 5.15.

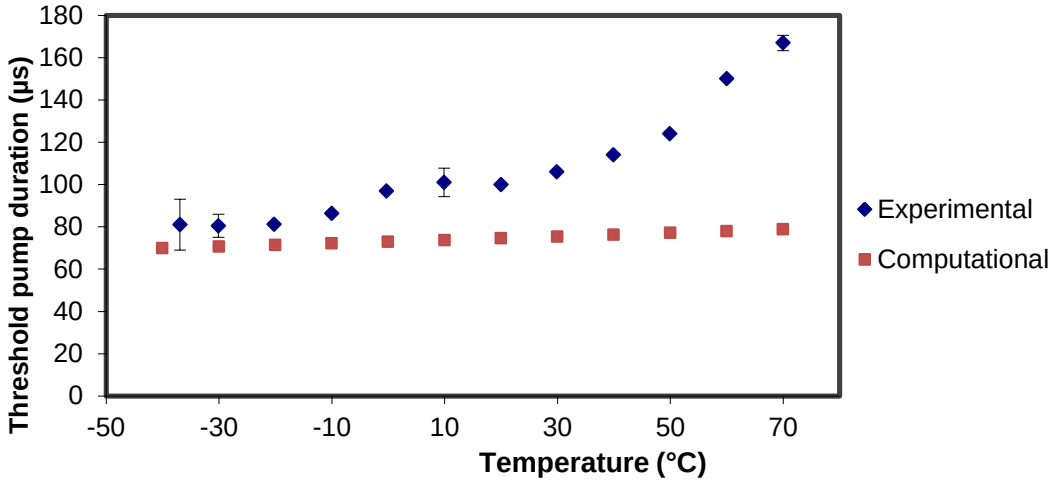

Figure 5.15: Experimental and computational results of threshold pump duration as a function of temperature. Results are obtained by investigating the temperature dependence of the effective stimulated emission cross section of Nd:YAG. Experimental data points are denoted by blue diamonds and the corresponding computational points by red squares.

Both the experimental measurements and modelled data maintain an upward trend against temperature. The experimental points increase at a far higher rate than the theoretical points. Additionally, it appears that the experimentally measured points follow a non-linear relationship with temperature, whilst the modelled points follow a more linear trajectory. Consequently, the emission cross section variation over temperature can be ruled out as the dominant cause of threshold pump fluctuations, especially at high temperatures.

The pulse timing jitter of the system is crucial for designator classification, as outlined in the NATO standardised agreement number 3733. It is required that, over the full temperature range, the jitter does not exceed 5 µs (commercially preferable 2 µs). Presented below are the resulting experimental and modelled results of timing jitter over temperature.

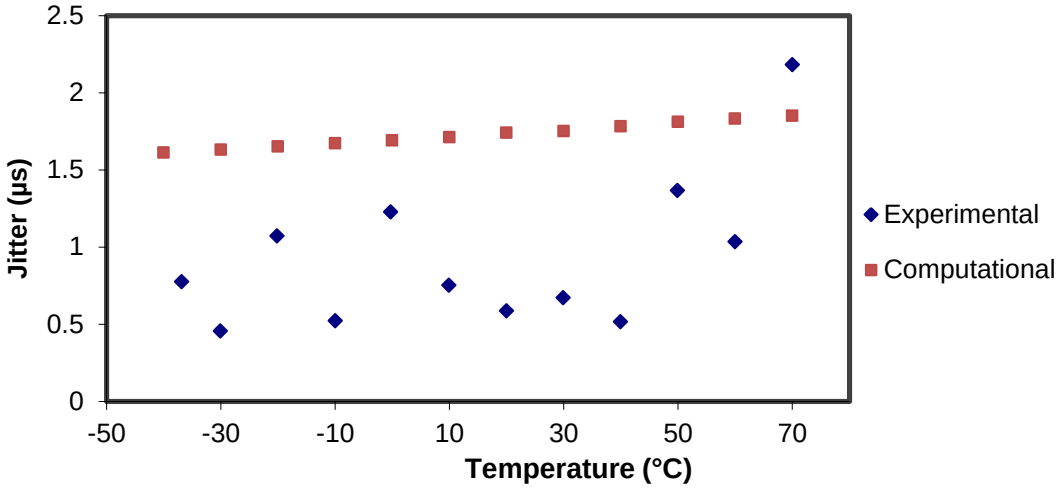

Figure 5.16: Experimental and computational results of timing jitter as a function of temperature. Results are obtained by investigating the temperature dependence of the effective stimulated emission cross section of Nd:YAG. Experimental data points are denoted by blue diamonds and the corresponding computational points by red squares.

The theory shows a weak upward trend of the timing jitter temperature. This is due to the increase in the threshold pump duration with temperature exacerbating the effects of pulse-to-pulse pump power fluctuations, as has been discussed in Chapter 3. The modelled data does show a higher jitter value in general than the experiment. This discrepancy is likely due to the oversimplified jitter model; which evaluates the threshold of the Q-switched pulse at two different pump powers, with the jitter being the time difference between the two threshold points. An overestimate of the pump power fluctuations would result in a higher modelled jitter value. Crucially however, both modelled and experimental data remains below 2 µs, with the exception of the 70 °C experimental point which we have already discussed.

The output pulse duration has considerably looser requirements, and is not specified in STANAG 3733. The requirements are simply that the duration is in short enough to ensure a high enough peak power, and long enough so the detectors are able to register a single pulse. Typically we would be looking for values in the range 10 to 50 ns. Below we present a plot of output pulse width against temperature.

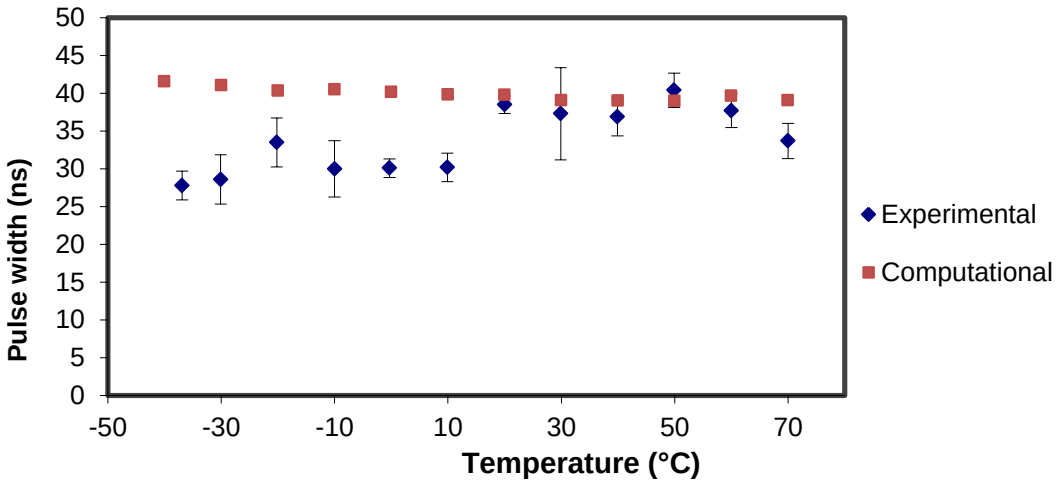

Figure 5.17: Experimental and computational results of Q-switched pulse width as a function of temperature. Results are obtained by investigating the temperature dependence of the effective stimulated emission cross section of Nd:YAG. Experimental data points are denoted by blue diamonds and the corresponding computational points by red squares.

The experimental values follow an approximately upward trend with temperature, which is not seen with the modelled data. The modelled data shows a slight decline in pulse duration with temperature. This slight decrease is to be expected, considering pulse width generally follows an inverse relationship with energy [7]. It is worth noting that the error bars are particularly high in experimental points here.

All the aspects described in the above section show that the temperature relationship of the effective cross section of Nd:YAG alone is not enough to model the temperature performance of our system. The next temperature dependent parameter we will evaluate is the decay rate of the excited state of Cr:YAG.

5.3.4.2 Cr:YAG excited state decay rate against temperature

In this section we present the modelled results of varying the excited state decay rate of Cr:YAG, together with the experimental results gathered during temperature testing. The effective emission cross section of Nd:YAG was held constant at 3.8 $x10^{-19}$ cm^{-2} over the temperature range during this modelling. Below we present the modelled and experimentally measured Q-switched pulse energy.

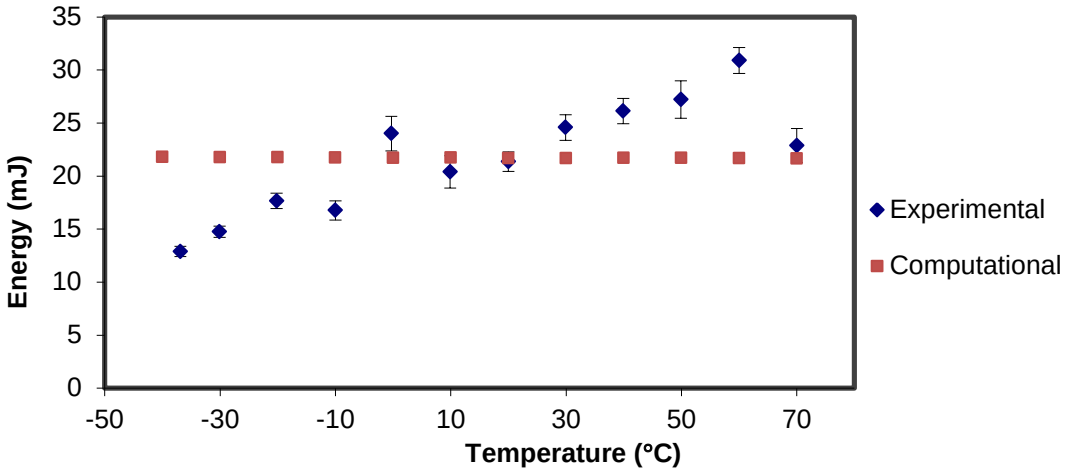

Figure 5.18: Experimental and computational results of pulse energy as a function of temperature. Modelled results are obtained by assessing the temperature dependence of the Cr:YAG excited state decay rate. Experimental data points are denoted by blue diamonds and the corresponding computational points by red squares.

It can be seen from Figure 5.18 that by varying the excited state decay rate of Cr:YAG, the resulting modelled data shows no variation in Q-switched energy over temperature. In fact we see no significant variation in any of the output parameters. For this reason, we are confident that the excited state decay rate does not have a bearing on the output parameters over the temperature range.

5.3.4.3 Absorption coefficient of Nd:YAG

The final material parameter which we are concerned with for temperature testing is the absorption coefficient of Nd:YAG. As described in section 5.2.2, it is the temperature variation of the diode wavelength, coupled with the spectral variation of the Nd:YAG absorption, which drives this mechanism. We have modelled the maximum range of values of absorption coefficient which are possible over the temperature range, as described in section 5.2.2. The results of our rate equation model ran over varying absorption coefficient is presented below in Figure 5.19, were we present the modelled results of the single pulse energy against the absorption coefficient of Nd:YAG.

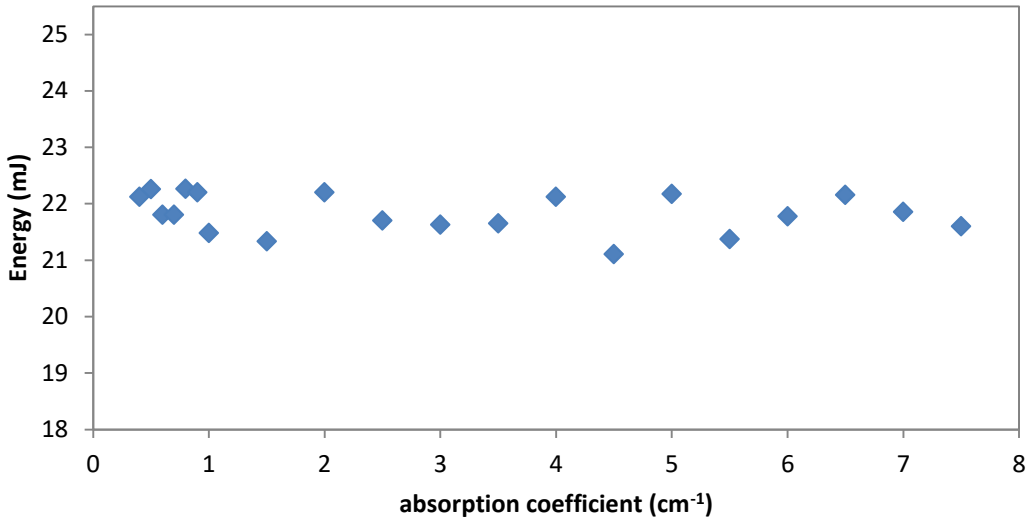

Figure 5.19: Computational results of single pulse output energy as a function of the Nd:YAG absorption coefficient.

It can be seen that there is very little variation in the output pulse energy over the entire range of absorption values. The small variation between some points, less than 0.1 mJ, is most likely due to the limited accuracy of the ordinary differential equation solver in the rate equation model. It can therefore be concluded that the Nd:YAG rod is sufficiently long, at 5 cm, that the pump light is completely absorbed over the whole range of absorption coefficient values. There was also no notable variation in the pulse duration, jitter or threshold pump time, which we have consequently chosen not to show here. This shows that the absorption coefficient, and therefore diode wavelength, has no effect on the output parameters of our system. Now we will consider other temperature driven effects which are not related to the laser crystals, starting with the diode power.

5.3.4.4 Pump power degrading

Now we will look at mechanism by which the diode output power degrades with increasing temperature, and the effect it might have on Q-switched laser performance. We have varied the diode pump power according to the data provided by Quantel, then scaled it up for a 3 kW stack as described in section 5.2.4. All other parameters are held constant over the temperature range. Again we begin by looking at the pulse energy against temperature, as seen in Figure 5.20.

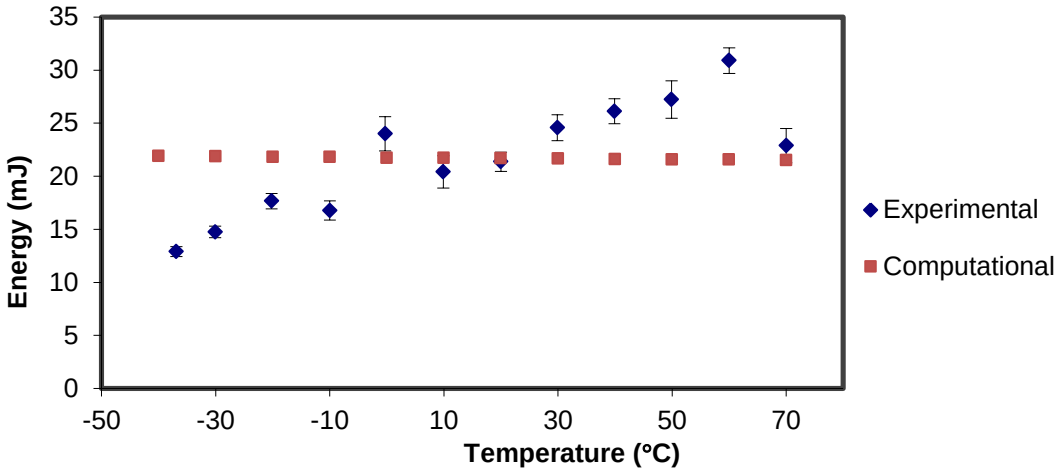

Figure 5.20: Experimental and computational results of output energy as a function of temperature. Results are obtained by investigating the temperature dependence of the pump diode power. Experimental data points are denoted by blue diamonds and the corresponding computational points by red squares.

Considering the results shown above, we can see that there is no substantial variation in the pulse energy when the diode power drops with increasing temperature. If nothing else has changed other than diode power, then the same population inversion should be reached, regardless of pump power. For this reason, the drop in gain when the Q-switch *opens* will remain constant, and therefore the output energy, over the entire temperature range. What will change is the duration in which the system requires to be pumped before it reaches threshold, as seen in Figure 5.21.

As predicted, the threshold pump duration increases with temperature, according to the drop in diode power. This is consistent with both the modelled and measured results, however, the model does not fully describe the rate of increase in threshold as seen in the experiment. We have only presented the energy and threshold pump duration results as the Q-switched pulse duration was unaffected by the model, and the pulse jitter is directly related to the threshold in our model.

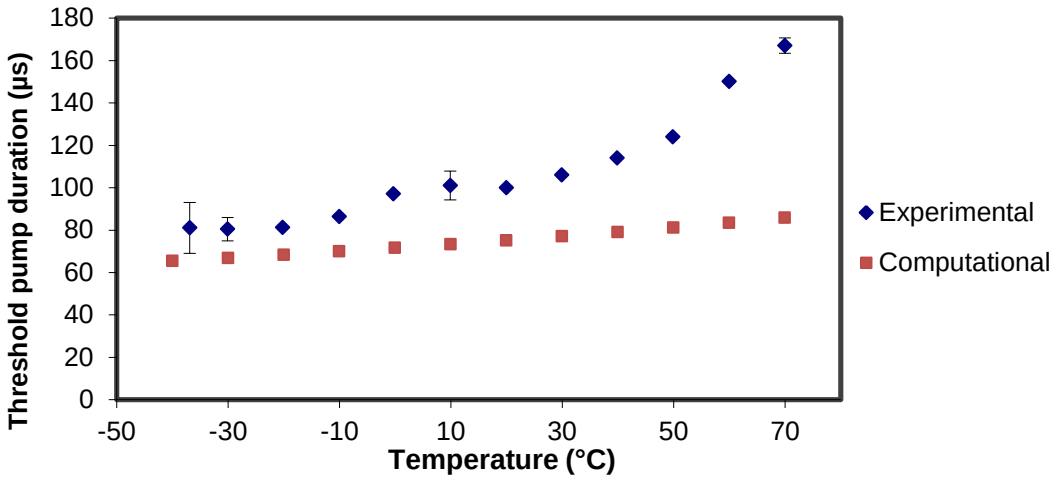

Figure 5.21: Experimental and computational results of threshold pump duration as a function of temperature. Results are obtained by investigating the temperature dependence of the pump diode power. Experimental data points are denoted by blue diamonds and the corresponding computational points by red squares.

As it stands the model does not accurately describe the intensity of the temperature effects. For this reason we will now speculate as to the potential effect of changing the laser mode size with temperature.

5.3.4.5 Mode size and pump overlap efficiency

Here we present only the experimental values for the beam divergence in the x and y direction, as an approximate indicator for varying mode size. Although not a STANAG requirement, for commercial purposes we specify a FWHM beam parameter product. The beam divergence on the designator has to be tight to ensure enough energy on the target. There is a practical limit to how large the telescope can be on front of the laser. Then we expect a FWHM beam parameter product to be less than 15 mm mrad. The results of our divergence measurements over temperature are presented in Figure 5.22.

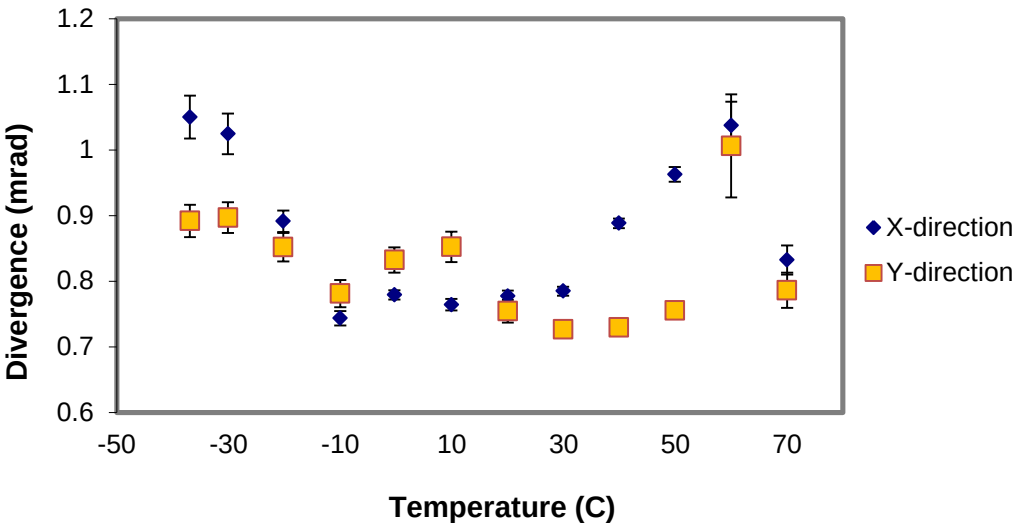

Figure 5.22: Experimental results of beam divergence as a function of temperature. Divergence in the x-direction is denoted by blue diamonds and the corresponding y-divergence by yellow squares.

The maximum beam parameter product we measured here is 6 mm mrad (6 mm beam diameter approximated as equal to Nd:YAG rod diameter), which is comfortably within the minimum specifications across the whole temperature range. We can see that, in both directions, there are fluctuations in the beam divergence. There does not appear to be an obvious trend in the data, with fluctuations occurring between each consecutive point. We see an almost 27 % variation in the divergence over the entire temperature range. We were not able to measure the near-field beam diameter in the chamber so it is not possible to quote the variation in beam quality over the temperature range. This would have provided us with a more accurate representation of the change in laser mode size over temperature. We will speculate as to the likely change in mode size in the following section.

As described in section 5.2.5, Equation 5.3 describes how the change in mode size will affect the energy and threshold pump duration of a passively Q-switched laser. We are speculating that the mode size will increase with temperature, as presented in Figure 5.23. We have chosen to vary the mode radius from 2.22 mm to 2.99 mm, in order to achieve a reasonable agreement with the measured output energy over temperature. This represents a 26 % drop in mode size, which is not

unrealistic, given the variation in the measured divergence shown in Figure 5.22. It is also supported by the reciprocal nature of beam divergence with beam size [3].

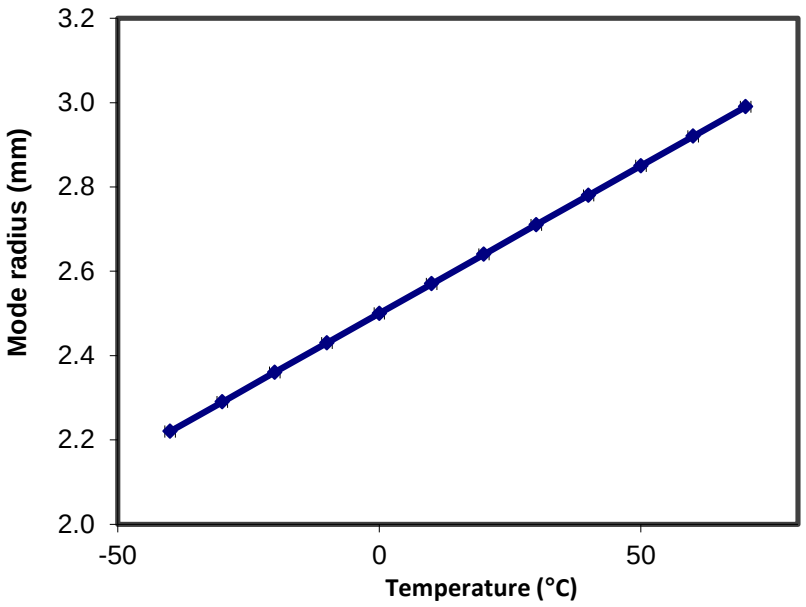

Figure 5.23: Estimated temperature dependence of laser mode radius and pump beam overlap ratio.

We have used this relationship in our laser rate equations to predict the effect of changing laser mode size on the laser performance. Again, we have only presented the energy and threshold pump duration results as the Q-switched pulse duration was unaffected by the model, and the pulse jitter is directly related to the threshold in our model.

From Figure 5.24, we can see that increasing the mode size with temperature has a significant impact on the output energy. The gradient of the line is more comparable with the experimental results than our previous modelling.

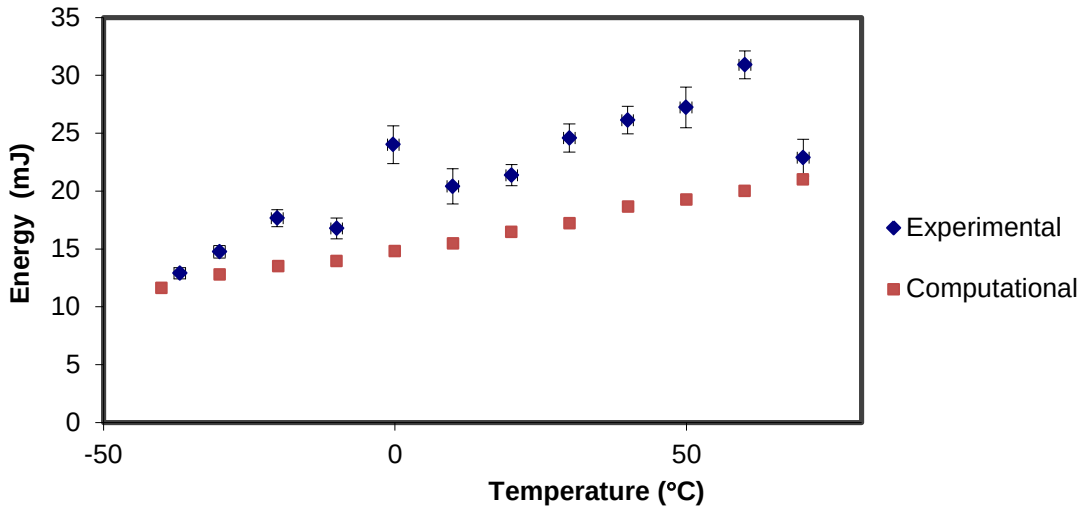

Figure 5.24: Experimental and computational results of output energy as a function of temperature. Results are obtained by investigating the temperature dependence of the laser mode size. Experimental data points are denoted by blue diamonds and the corresponding computational points by red squares.

Below, in Figure 5.25, we can see the impact on the threshold pump duration of varying mode size.

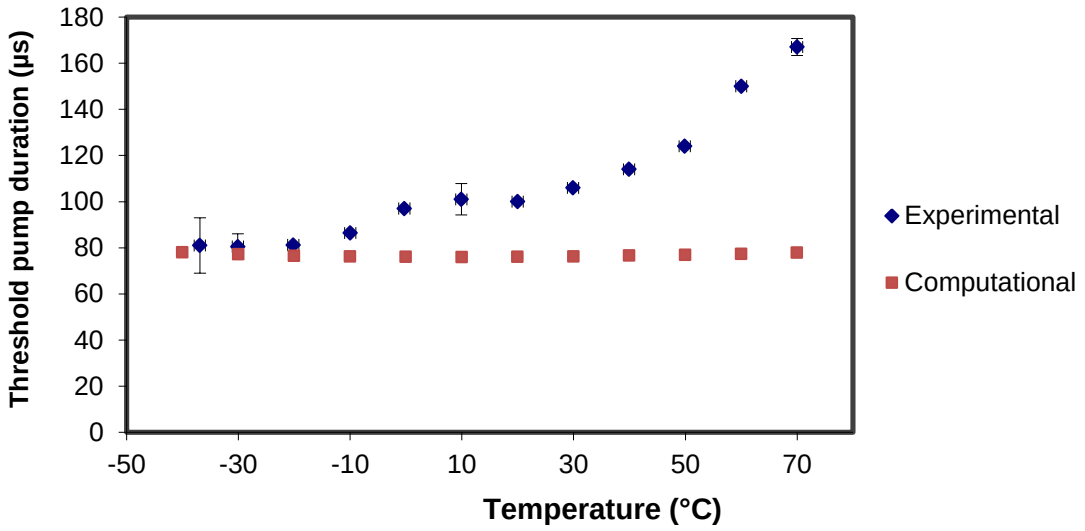

Figure 5.25: Experimental and computational results of threshold pump duration as a function of temperature. Results are obtained by investigating the temperature dependence of laser mode size. Experimental data points are denoted by blue diamonds and the corresponding computational points by red squares.

There appears to be no trend between threshold and temperature in the model. This is due to the way the model handles mode size and pump absorption. The pump energy absorbed within the laser rod is approximated as a homogenous volume, which leads

to a correspondingly homogenous gain distribution. This means that, regardless of mode size, the laser reaches threshold at the same time since the losses and gain are constant throughout the rod. In reality different modes of varying diameter would have different threshold conditions. The results are significant enough to include beam size variation within a more comprehensive model, which evaluates the combined effects of multiple temperature relationships discussed above.

5.3.4.6 Combined model: effective cross section, diode power and mode size

The following results are from a comprehensive model which combines the temperature dependent models of the: a) effective stimulated emission cross section of Nd:YAG, b) diode pump power and c) laser mode size. The Cr:YAG decay rate and Nd:YAG absorption are left out of this model as they showed no significant impact on the laser performance. As before, we will start by looking at the Q-switched pulse energy.

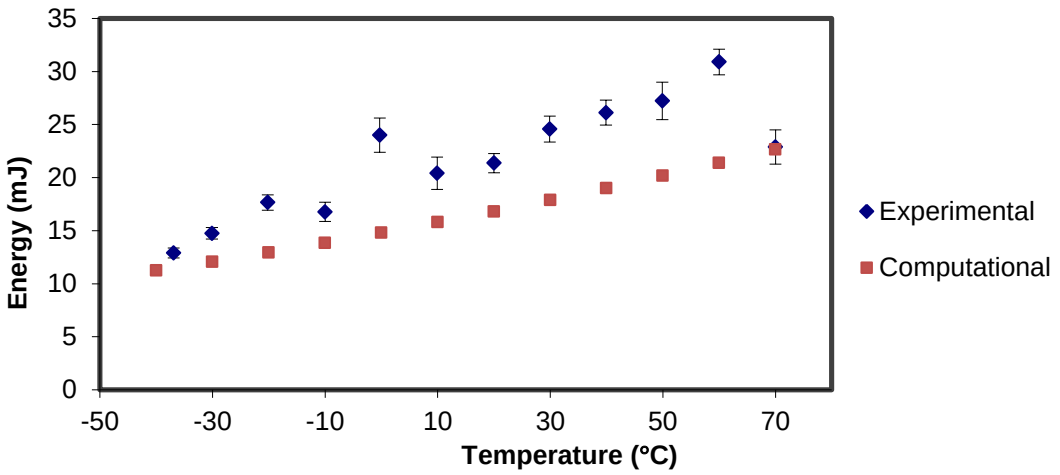

Figure 5.26: Experimental and computational results of output energy as a function of temperature. Results are obtained using the combined model of the temperature dependence of the effective stimulated emission cross section of Nd:YAG, pump diode power, and laser mode size. Experimental data points are denoted by blue diamonds and the corresponding computational points by red squares.

We find that the predicted energy is much closer to the experimentally determined trend, although the gradient of the incline is still not quite in agreement. This could indicate that one or more of the three modelled temperature relationships, in reality,

is more sensitive to temperature changes. We can then consider how the threshold pump duration is affected in this model, as seen in Figure 5.27.

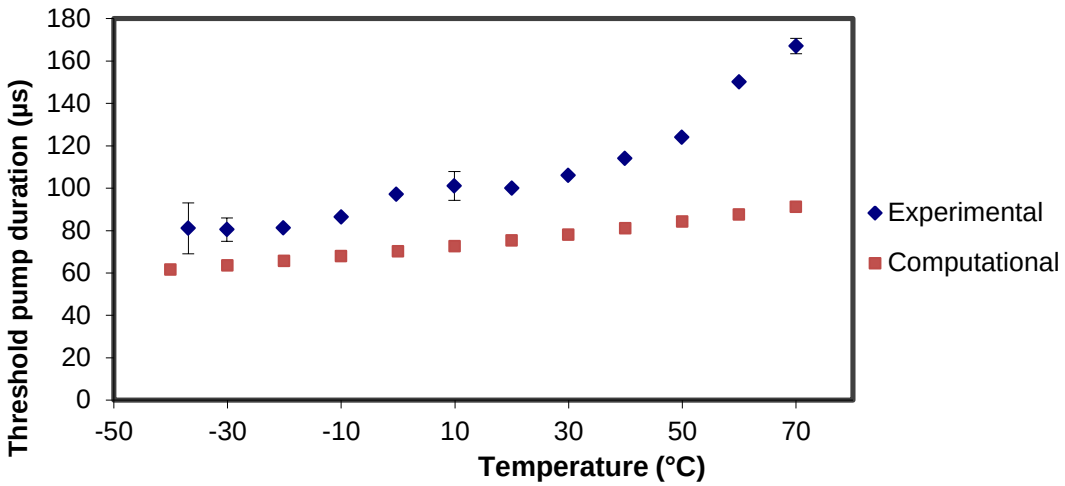

Figure 5.27: Experimental and computational results of threshold pump duration as a function of temperature. Results are obtained using the combined model of the temperature dependence of the effective stimulated emission cross section of Nd:YAG, pump diode power, and laser mode size. Experimental data points are denoted by blue diamonds and the corresponding computational points by red squares.

Looking at Figure 5.27, again we see a better comparison between the modelled and measured threshold pump duration. As with the energy, the model is further from the experiment at higher temperatures. One possibility is that the diode power degrades more, with increasing temperature, than reported by Quantel. This is likely considering the diode we use were manufactured by DILAS, and is further into its lifetime than a newly manufactured diode, for which the data is measured. In addition, the pump power drop could be larger for a stack than for a single bar, and hence the extrapolation between bar and stack might be lead to an underestimate of temperature effects. A more rapid pump power loss with temperature would predict a higher threshold at higher temperatures, thus pushing the model closer to the experimental values. This would have little effect on other parameters (as seen in section 5.3.4.4) and hence is a plausible, if not a proven, explanation. In our model, the threshold pump duration is used to calculate the timing jitter, which is presented as a function of temperature below in Figure 5.28.

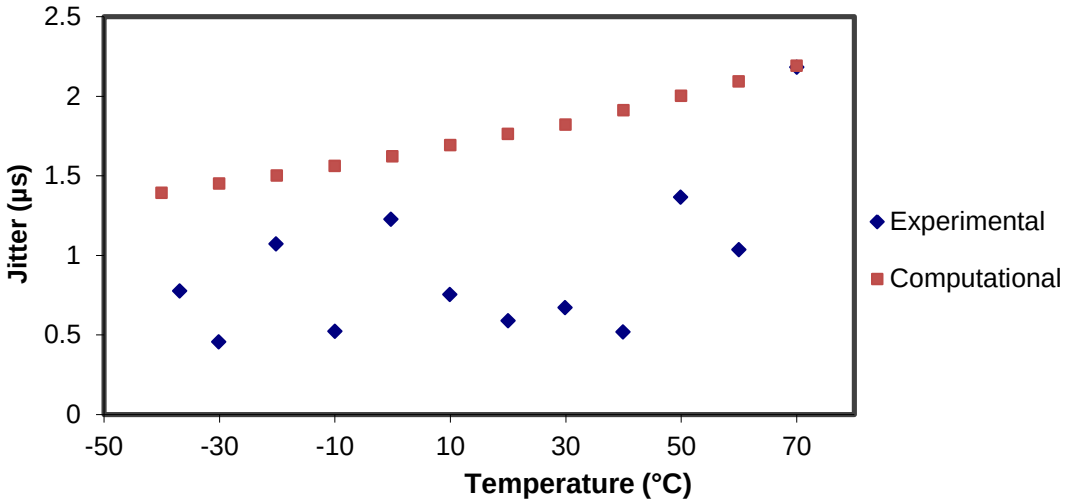

Figure 5.28: Experimental and computational results of pulse timing jitter as a function of temperature. Results are obtained using the combined model of the temperature dependence of the effective stimulated emission cross section of Nd:YAG, pump diode power, and laser mode size. Experimental data points are denoted by blue diamonds and the corresponding computational points by red squares.

We find that the jitter follows a similar upward trend as found in the experimental data. The model predicts slightly higher jitter than measured, which may be due to the simplified method of modelling jitter. It is also possible that the estimate of $\pm$ 1% pump power fluctuation used in the model is not accurate. It would be useful to measure the long term fluctuations in a range of different diodes to find a more accurate estimate.

The final parameter we have assessed with this model is the pump duration, which is presented below in Figure 5.29. As with all the other models evaluated in this chapter, there is no significant variation in the modelled pulse with over the entire temperature range. Given the large errors associated with the measured data points, it is plausible that there is some issue with the experimental setup, rather than an inherent temperature relationship. Having presented the experimental and modelled data, we can now discuss in more depth the issues raised above.

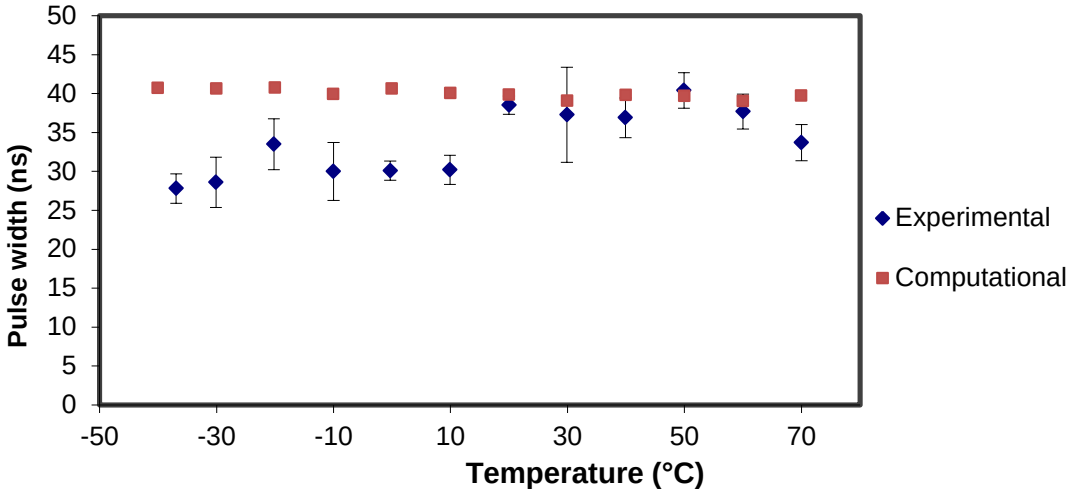

Figure 5.29: Experimental and computational results of Q-switched pulse duration as a function of temperature. Results are obtained using the combined model of the temperature dependence of the effective stimulated emission cross section of Nd:YAG, pump diode power, and laser mode size. Experimental data points are denoted by blue diamonds and the corresponding computational points by red squares.

5.4 Discussion and conclusions

In this chapter we constructed a mechanically stable passively Q-switched laser for thermal testing. Due to some issues with cavity misalignment, particularly at higher temperatures, we were required to realign the cavity between temperature points. We were only able to adjust the cavity at temperatures above 20 °C. Subsequently, we found it was at these points that the laser exhibited the largest variation in performance, and were therefore the most critical for model fitting. As a result, although we could not realign the cavity at every temperature, we believe it does not affect our conclusions.

Firstly, from our experiment we have seen that the energy shows a visibly linear increase with temperature. The single pulse energy ranges from 12.9 to 30.9 mJ, which falls well below STANAG compliance of 50 mJ. Considering our room temperature measurements of the breadboard laser used in Chapter 2 produced a single pulse energy of 53.4 mJ, it would be worthwhile to implement some of the components from the breadboard in the X-model system in future. This would include beam homogenisation, a larger laser rod diameter and a lower transmission

output coupler. If we implement these solutions, we would be able to push the energy of the system closer to the 50 mJ target.

During the temperature testing we also measured the pulse timing jitter, which remained within the STANAG requirement of ± 5 µs, over the entire temperature range, albeit from a laser with lower energy. The maximum jitter value we measured was 2.2 µs at 70 °C. This is consistent with our discussion that the resonator is in a particularly unstable alignment at 70 °C. Considering our conclusion in Chapter 3, that mechanical fluctuations are responsible for a significant proportion of the total jitter value, it is likely that subtle alignment variations introduced during mirror realignment will impact the jitter during temperature testing. Additionally, in a system with higher pulse energy (i.e. >50 mJ for STANAG classification) we would expect the jitter to also be higher. For this reason it would be necessary to test the jitter over temperature once the energy has been scaled up in future. We expect that if the component responsible for the mirror misalignment is isolated then the jitter levels (particularly at 70 °C) will remain below 5 µs over the entire temperature range, even in a higher energy system.

The Q-switched pulse duration showed a very slight relationship with the temperature, increasing as the temperature was increased. We measured a range of pulse width values from 27.8 to 40.4 ns. The fluctuations could be caused by slight differences in the resonator alignment between temperature measurements. The errors in the pulse width measurements are higher than expected which makes the resonator alignment issue a more likely cause. Ideally we would have identified the component responsible for causing this misalignment during temperature testing.

Considering now the threshold pump duration. We have measured a steady increase in the threshold duration, from 81 to 167 µs, with increasing ambient temperature. Promisingly, the threshold value remains well within our available maximum duration, which is 240 µs. This means that there is scope to use a lower initial transmission Q-switch to increase the output energy.

We have investigated the effects of several temperature dependent parameters in our rate equation model, in an attempt to better understand how changes in ambient temperature affect laser performance. We have established, as described in sections 5.3.4.2 and 5.3.4.3, that the decay properties of Cr:YAG and the spectral absorption

of the pump radiation in Nd:YAG have negligible impact on the output parameters of our laser model.

One parameter which did impact on the modelled laser performance was the effective stimulated emission cross section of Nd:YAG. The temperature dependence of this parameter was modelled according to Equation 5.1, as described in section 5.2.1. The modelled results showed that as the cross section increased with temperature, the energy and threshold pump duration also increased. The magnitude of the modelled increase is not significant enough to fully describe the temperature mechanism. This could be due to the model, described by A. Rapaport et. al [2], not being fully applicable to our Nd:YAG crystal, given that there is significant variation in the cross section values quoted by manufacturers. However, as reported by T. Dascalu and N. Pavel [4], it seems unlikely that variations in this parameter will yield such a strong temperature variation in the energy or threshold pump duration, as seen in our experimental results. The modelled Q-switched pulse duration was shown to follow a slight downward trend with temperature, consistent with an inverse relationship with energy. The opposite was seen in the experimental data, with pulse duration increasing with temperature. Considering the high experimental errors in the pulse width measurement, it is difficult to consider how well the model is aligned with the experimental results. The modelled timing jitter was predicted to be slightly higher than measured, although it does follow a similar upward trajectory. The discrepancy in the magnitude is most likely due to an oversimplification of the jitter model, which relies on a $\pm$ 1 % fluctuation in pump power.

The next temperature dependent parameter we investigated was the pump power. Using data from the diode manufacturer Quantel, we found that diode power decreased with increasing temperature. The resulting model showed no significant variation in energy or pulse width. The threshold pump duration increased with temperature, as expected, owing to the decrease in pump power. The decrease in pump power is still not sufficient to model the magnitude of the trends found in the experimental data, particularly the threshold and energy.

To further develop the model we have approximated a temperature model for the laser mode size. We applied a change in mode size of 26 % (a value consistent with the measured fluctuations in the beam divergence) and its corresponding effect

on the change in pump mode overlap efficiency with temperature. The modelled results showed a stronger trend between energy and temperature, pushing the model closer to the experimental data.

To provide a more comprehensive model, we then combined the effective stimulated emission cross section, diode power and mode size temperature relationships. The resulting modelled energy followed more closely the experimental data. The modelled pulse width, however, was still not able to describe the slight upward trend found in the experimental data. According to the model we should have seen a slight negative gradient in the experimental data. This discrepancy could again be due to a measurement error, given that the uncertainty is as high as 10 ns, although it is difficult to identify the cause at this point.

When considering the threshold pump duration, we still see a notable difference in the magnitude of the upward trend with temperature in the model and experiment. As mentioned previously, this could be due to an underestimate of the diode power degrading over temperature. This could also be due to an additional variable parasitic loss found within the laser cavity, which is not included in the model.

The timing jitter against temperature was found to have good agreement in the model and experiment. Both sets of data followed a very similar increase in jitter with temperature. The magnitude of the modelled jitter was however, significantly greater than the experiment. This is again likely due to an oversimplification of the jitter model. Despite the discrepancy in magnitude, these findings further support the conclusion from Chapter 3, that fluctuations in pump power contribute significantly to the timing jitter in our system.

To conclude, we have measured the output parameters of our X-model laser over a temperature range of -37 to + 70 °C. We saw significant increases in energy and threshold pump duration with increasing temperature. We also measured comparatively more random fluctuations in the timing jitter and Q-switched pulse duration. Recognising the uncertainty in the material parameters in our model, we are confident that the measured energy and threshold variation can be explained by modelling the temperature dependence of the effective emission cross section of Nd:YAG, diode power and laser mode size. Measuring for ourselves the extent to

which these parameters vary over temperature, particularly the mode size and diode power, would allow the model described in this chapter to be further evaluated. Additionally, it would be important to isolate the component that is causing the resonator misalignment between temperature points. This would give us more confidence in the low temperature data, for which it was not possible to optimise the alignment between temperature points. We believe, however, that this does not strongly affect our conclusions because our model results can still be compared with the high temperature data. Furthermore, we argue that the effects of mechanical misalignment are less significant at lower temperatures, as seen by the relatively shallow gradient of the threshold pump duration against temperature below 20 °C. These areas would form part of our future work section.

5.5 References

[1] *Standardized Agreement 3733*, 2nd ed. North Atlantic Treaty Organisation, 2005.

[2] A. Rapaport, S. Zhao, G. Xiao, A. Howard, and M. Bass, "Temperature dependence of the 1.06-um stimulated emission cross section of neodymium in YAG and in GSGG," *Appl. Opt.*, vol. 41, no. 33, p. 7052, 2002.

[3] W. Koechner, *Solid-State Laser Engineering*. New York: Springer, 2006.

[4] T. Dascalu and N. Pavel, "High-temperature operation of a diode-pumped passively Q-switched Nd:YAG/Cr4+:YAG laser," *Laser Phys.*, vol. 19, no. 11, pp. 2090–2095, 2009.

[5] Crytur, "Laser rods - Neodymium doped," *Nd:YAG laser material properties*, 2017. [Online]. Available: https://www.crytur.cz/products/laser-rods-neodymium-doped/. [Accessed: 08-May-2017].

[6] DILAS, "3 kW QWC diode stack performance," Product datasheet, 2012.

[7] J. J. Degnan, "Optimization of passively Q-switched lasers," *IEEE J. Quantum Electron.*, vol. 31, no. 11, pp. 1890–1901, 1995.

[8] Y. F. Chen, Y. P. Lan, and H. L. Chang, "Analytical Model for Design Criteria of Passively Q -Switched Lasers," *IEEE J. Quantum Electron.*, vol. 37, no. 3, pp. 462–468, 2001.

[9] H. Eilers, U. Hömmerich, S. M. Jacobsen, W. M. Yen, K. R. Hoffman, and W. Jia, “Spectroscopy and dynamics of Cr4+:Y3Al5O12,” *Phys. Rev. B*, vol. 49, no. 22, pp. 15505–15513, 1994.

[10] G. Xiao, J. Lim, and S. Yang, “Z-scan measurement of the ground and excited state absorption cross sections of Cr4+ in yttrium aluminum garnet,” *IEEE J. Quantum Electron.*, vol. 35, no. 7, pp. 1086–1091, 1999.

[11] S. Kück, K. Petermann, U. Pohlmann, and G. Huber, “Near-infrared emission of Cr4+-doped garnets: Lifetimes, quantum efficiencies, and emission cross sections,” *Phys. Rev. B*, vol. 51, no. 24, pp. 17323–17331, 1995.

[12] P. S. Zory, A. R. Reisinger, R. G. Waters, L. J. Mawst, C. A. Zmudzinski, M. A. Emanuel, M. E. Givens, and J. J. Coleman, “Anomalous temperature dependence of threshold for thin quantum well AlGaAs diode lasers,” *Appl. Phys. Lett.*, vol. 49, no. 1, pp. 16–18, 1986.

[13] S. Sakai, T. Soga, M. Takeyasu, and M. Umeno, “Room-temperature laser operation of AlGaAs/GaAs double heterostructures fabricated on Si substrates by metalorganic chemical vapor deposition,” *Appl. Phys. Lett.*, vol. 48, no. 6, pp. 413–414, 1986.

[14] J. Dong, J. Lu, and K. Ueda, “Experiments and numerical simulation of a diode-laser-pumped Cr, Nd:YAG self-Q-switched laser,” *J. Opt. Soc. Am. B*, vol. 21, no. 12, p. 2130, 2004.

[15] H. Kim, “Optimal design of retroreflection corner-cube sheets by geometric optics analysis,” *Opt. Eng.*, vol. 46, no. 9, p. 094002, 2007.

[16] M. Acharekar, “Derivation of internal incidence angles and coordinate transformations between internal reflections for corner reflectors at normal incidence,” *Opt. Eng.*, vol. 23, no. 5, 1984.

[17] D. Wright, P. Greve, J. Fleischer, and L. Austin, “Laser beam width, divergence and beam propagation factor—an international standardization approach,” *Opt. Quantum Electron.*, vol. 24, pp. 993–1000, 1992.

[18] S. Zhao, A. Rapaport, J. Dong, B. Chen, P. Deng, and M. Bass, “Temperature dependence of the 1.064 nm stimulated emission cross-section of Cr:Nd:YAG crystal,” *Opt. Laser Technol.*, vol. 38, no. 8, pp. 645–648, 2006.

[19] C. J. Mercer, Y. H. Tsang, and D. J. Binks, “A model of a QCW diode

pumped passively Q- switched solid state laser," *J. Mod. Opt.*, vol. 54, no. 12, pp. 1685–1694, 2007.

[20] J. Dong, "Numerical modeling of CW-pumped repetitively passively Q-switched Yb:YAG lasers with Cr:YAG as saturable absorber," *Opt. Commun.*, vol. 226, no. 1–6, pp. 337–344, 2003.

[21] MolTech GmbH, "Cr4+:YAG," *Laser Crystals: Catalogue page*, 2018. [Online]. Available: http://www.mt-berlin.com/frames_cryst/crystals_frameset1.htm. [Accessed: 06-Feb-2018].

Chapter 6 Conclusions

The purpose of this research project was to assess the potential for a passively Q-switched system to be implemented in future generations of military target designators. Designation involves illuminating a target with a high energy laser pulse, which is then detected by the seeker of a missile, which then steers towards the target. For this, we needed to set out the requirements for a passively Q-switched laser suitable for designation. The system requirements, as described in chapter 1, are summarised below:

- Pulse energy > **50 mJ** – for detection at long ranges
- High peak power – for sufficient signal above seeker detection limit for ranges of up to 10 km
- Wavelength **1064 nm** – to correspond with detectors in missile seekers
- Repetition rate 10 – 20 Hz – to match STANAG designation codes
- Compact design – to be man portable or to fit in small sensor pods
- Low beam divergence – for increased range performance (up to 10 km)
- Function over ambient temperature range of -40 to +70 °C
- Pulse timing jitter < **± 5 µs** – to allow resolution of frequency code

The most important specifications (highlighted above in bold) are the energy, wavelength and timing jitter, as these are stipulated in the STANAG document [1]. Meeting the STANAG specifications is required to allow the system to be classified as a military *designator* as opposed to markers (which have the same function, but at lower energy). Having considered these areas, the design we have settled on has the following properties:

- Nd:YAG gain medium
    - 1064 nm emission – conforms to strict STANAG requirement
    - fluorescence lifetime (230 µs) – Allows large stored energy during pumping to meet energy requirement
- Diode stack pump beam
    - Lower power consumption than flashlamps which is crucial for man portable devices (lower power consumption means fewer batteries)

- End pumped configuration of the gain medium
    - This ensures constant total pump absorption over the temperature range (-40 to +70 °C)
- Pump beam homogenisation
    - Required due to end-pumped design to overcome the stripy diode stack beam
- Cr:YAG passive Q-switch
    - Saturable absorption at STANAG required wavelength 1064 nm
    - Long (4.1µs) excited state lifetime to prevent premature closing of Q-switch

With these design considerations, we then identified four main challenges which are investigated under each chapter heading. These challenges, together with the relevant specifications, are as follows:

- Pump homogenisation and production of high energy Q-switched pulses
    - Required for end pumping with diode stack
    - To reach > 50 mJ pulse energy
- Achieving low timing jitter pulse trains
    - Challenging because of passive Q-switching
    - $< \pm$ 5 µs jitter target
- Optimising selection of passive Q-switch material
    - Ensure correct choice of commercially available 1064 nm material
    - Optimised based on pulse energy, duration, jitter and threshold
- Maintaining output over temperature range (-40 to +70 °C)
    - Measure energy, pulse duration, jitter and threshold over temperature

These areas form the basis of the research presented in this thesis. The conclusions will summarise to what extent the design requirements have been addressed, and which engineering challenges remain. We will start discussing the results of our investigation into pump beam homogenisation and its effect on single pulse energy.

6.1 The effects of homogenisation of a diode-stack pump source on QCW and Q-switched Nd:YAG laser output.

To date, the pulse energy of passively Q-switched (PQS) systems have been limited, particularly when using an end pumped configuration. We identified that this was largely due to the non-uniform (stripy) pump beam profile found in diode stacks. After researching various methods of pump beam homogenisation, we found that a cheap and readily available method was to use an engineered diffuser. These versatile components are available off the shelf and can be implemented relatively easily, with the addition of only a single focusing lens.

The resulting pump beam from using an engineered diffuser was improved significantly, completely removing the striped structure found previously. This had a substantial impact on both the QCW and Q-switched pulse energy. The Q-switched energy increased by a factor of 4 by pump homogenisation with an engineered diffuser. The energy was still only 6.3 mJ because this setup used a non-optimal telescope to couple the pump beam into the rod. To improve this we then moved on to a system which used the engineered diffuser in tandem with a large aperture condenser lens, and a larger diameter (1 cm) Nd:YAG rod, to increase the volume of energised gain material. The diameter of the pump beam incident on the rod face was 8 mm, and there were no high intensity (stripy) gain regions to cause premature Q-switching. The result was an average single pulse energy of 53.4 mJ, which is suitable for STANAG compliance. To our knowledge this is the highest single pulse energy achieved by a diode end-pumped Nd:YAG, passively Q-switched laser. This was sufficient evidence that pump beam homogenisation, coupled with an increased rod size show promise as a means to reach high energy Q-switch pulses. The next challenge, which we examined in chapter 3, is the high timing jitter associated with passively Q-switched systems, which we will now review.

6.2 Investigation into the potential jitter mechanisms present in a high single pulse energy, passively Q-switched laser

We investigated two types of temporal issues associated with passive Q-switching: timing jitter and satellite pulses. High timing jitter is considered a significant challenge in a PQS system, with spontaneous emission noise reported as the dominant mechanism [2] [3]. This seemed an unlikely cause in our system, since the jitter values (microseconds) we faced were much higher than reported in these studies (nanoseconds). To investigate this we used rate equation modelling to simulate random fluctuations in the fluorescence seed term. From this we estimated that stimulated emission noise would only contribute 20 ns of timing jitter.

We found that the main source of jitter in our system was from mechanical vibrations. By reducing mechanical vibrations and airflow around the laser, we were able to achieve a reduction in timing jitter from 16 µs to 3.2 µs, which is within STANAG compliant levels ($< \pm$ 5 µs). Therefore mechanical vibrations were found to be the dominant jitter mechanism in our case. This was measured in a breadboard setup, but a fully engineered design would most likely have a cavity configuration that is less sensitive to mechanical movement.

In another investigation we measured the fluctuations in pump power and used this to predict how this affects timing jitter in our rate equation model. We have estimated that the ± 1 % pump power fluctuations delivered by the laser driver contributed nearly 1.6 µs of the remaining 3.2 µs of jitter. We believe that this represents the most significant portion of residual jitter, after removing mechanical vibrations. We are confident that with further mechanical and pump power stabilisation, the jitter could be brought below $\pm$ 2 µs which is commercially desirable, but not necessary, for the current generation of military detectors.

The other aspect of temporal stability which we investigated was satellite pulses, which consist of a primary pulse followed closely by a smaller amplitude pulse. We concluded that the most likely mechanism causing these undesirable satellites was longitudinal mode competition. This was found by comparing the spectral and temporal profile of the Q-switched pulses. We found that in the cases where the satellite was present in the temporal profile, a satellite to the main peak

was also observed in the spectral output. The next step in this investigation would therefore be to insert an etalon into the cavity in an attempt to push the competing mode below threshold. It is hoped that this will eliminate the satellite pulse, which is required if a PQS system were to be used in target designation.

The next chapter involved an investigation to confirm if Cr:YAG was still the best PQS material for our purposes, by comparing its performance with V:YAG and BDN dye.

6.3 Assessment of Cr:YAG, V:YAG and BDN Dye Saturable Absorbers as Passive Q-switches for High Energy 1064 nm Lasers.

The only commercially viable Q-switch materials which have high saturable absorption at 1064 nm are currently Cr:YAG and V:YAG. In this chapter we compared their absorption properties and Q-switch performance. From our review of the literature, we did not find any reference to work assessing V:YAG as a passive Q-switch for high energy 1064 nm systems. With a review of the properties of V:YAG, prior to our experiments, we saw no reason for V:YAG to perform poorly [4][5], since the absorption cross sections were comparable. We also included an analysis of the Q-switch performance of BDN (bis[4-dimethylaminodithiobenzil] nickel), which was used in previous generations of military lasers. This material is not used presently due to difficulties in finding a reliable supplier, and also due to its limited component lifetime.

The first section of the experimental work used the z-scan method to measure the absorption cross sections of Cr:YAG and V:YAG. We found that our samples varied, although not significantly, from the manufacturers specifications. This can be seen in Table 6.1, which compares the cross sections measured by our z-scan with that measured by the manufacturer.

Table 6.1: Comparison of absorption cross section values of V:YAG and Cr:YAG found during our z-can experiment and from the manufacturers specifications/literature [6] [4].

	Measured by manufacturer			Measured results of z-scan		
	σ_1 (x 10^{-18} cm^2)	σ_2 (x 10^{-19} cm^2)	$\beta = \frac{\sigma 2}{\sigma 1}$	σ_1(x 10^{-18} cm^2)	σ_2(x 10^{-19} cm^2)	$\beta = \frac{\sigma 2}{\sigma 1}$
V:YAG	1.0	2.2	0.22	1.25	3.1	0.25
Cr:YAG	2.1	1.7	0.081	2.1	3.1	0.15

We used our measured values in our rate equation model in the subsequent investigations into Q-switch performance. It was found experimentally, that Cr:YAG and BDN were able to produce the desired high energy single pulses, whereas V:YAG resulted in a train of significantly lower energy pulses. By considering the rate equation model we were able to establish that the short excited state lifetime of V:YAG (22 ns) was responsible for reducing the pulse energy, compared with the Cr:YAG (4.1 µs) system. The short lifetime causes the Q-switch to close during the emission of the pulse, preventing full utilisation of the stored energy.

Interestingly, the BDN had an even shorter excited state lifetime (2.9 ns), which should have resulted in low energy pulses similar to V:YAG. BDN, however, has much higher absorption cross sections (2 orders of magnitude higher than V:YAG), and therefore a much lower saturation fluence. This allows the intracavity fluence to maintain the Q-switch in the open state long enough to produce a high energy pulse, unlike the V:YAG system, for which the cavity fluence is not sufficient to maintain the Q-switch in a saturated state. However, BDN did exhibit some early closing which did reduce the pulse energy compared to Cr:YAG. A summary of the laser performance and modelling results for all three materials is presented in Table 6.2.

From the data in Table 6.2 we can see that Cr:YAG produces the highest single energy pulse and V:YAG does not even reach 1 mJ. Another point to note is the measured pulse duration is considerably longer than the simulated duration. This is likely due to some assumptions made in the model such as, that the laser is operating single mode (high order modes are not handled by our model). Additionally, the precise choice of saturable absorber absorption cross sections affects the pulse duration, and energy, dramatically. Despite the fact that we

measured these for Cr:YAG and V:YAG, the errors in the measurement may be causing the discrepancy in the pulse duration. There are likely other areas which affect the pulse duration which we have not modelled, which would form part of future research if necessary.

Table 6.2: Comparison of measured and simulated pulse energy and duration for Cr:YAG, BDN and V:YAG. Initial transmission (T_0) of each material used is presented as a %.

	Measured		Simulated	
Material (T_0)	Energy (mJ)	Pulse duration (ns)	Energy (mJ)	Pulse duration (ns)
Cr:YAG (60%)	25.0	32	24.4	4.8
V:YAG (60%)	0.2	200	0.24	82.1
Cr:YAG (50%)	32	22.5	30.5	4.0
BDN (51%)	20	13	22.4	3.4

Based on the single pulse energy, we have concluded that Cr:YAG is still the best saturable absorber for high energy pulses production at 1064 nm, which is readily available and economical in a production setting.

The final aspect of military designators that we investigated was the ambient temperature range over which they are required to function.

6.4 Thermal performance of a Cr:YAG passively Q-switched 1 micron Nd:YAG laser

In this chapter, Cr:YAG passively Q-switched laser was housed in a metal chassis to allow the laser to fit inside a temperature testing chamber. The cavity configuration was a U shaped resonator, with a monolithic HR/OC mirror paired with a retro-reflecting corner cube, and a rotating prism pair for alignment. The cavity was designed to be insensitive to movement of the components during temperature fluctuations. However, we concluded that one (or perhaps a few) of the components was likely moving over temperature, particularly above room temperature, resulting in a misalignment of the cavity. In order to concentrate on the intrinsic properties of the Q-switch laser, we realigned the cavity at each temperature point, where practical. As it turned out, we were able to do this at the temperatures which showed the most significant variation in laser performance, which were therefore the most critical for model fitting. Consequently, although we could not realign the cavity at

every temperature, it does not affect our conclusions. In a full prototype laser, a full thermo-mechanical design would be carried out to remove thermal movement.

We found that the single pulse energy and threshold pump duration showed a strong relationship with ambient temperature, both increasing with increasing temperature. By researching the surrounding literature, we found some laser parameters which showed some temperature dependence. We then included these temperature relationships in our rate equation model in an attempt to describe the behaviour seen in the experiment. It was found that the effective stimulated emission cross section (Nd:YAG), pump power, and laser mode size, are potential mechanisms which reasonably describe the experimentally observed changes in pulse energy and threshold pump duration. One area for further work would be to verify experimentally the change in mode size with temperature, that we have assumed in the modelling. It is worth noting that the system used in this investigation did not have all the adaptations used previously, such as: a larger radius Nd:YAG rod; an OC reflectivity of 70 % (instead of 50 %); a higher initial absorption (i.e. lower initial transmission) Cr:YAG. This meant that we were unable to reach the STANAG compliant pulse energy (50 mJ) with the X-model laser. We are confident that by implementing some (or all) of these elements we can reach this target at room temperature. Maintaining this value of all temperatures, especially below room temperature, will require more work however. This leads on to a discussion of how the project has concluded in general, and some ideas for future work.

6.5 General conclusions and future work

During this research project, we were able to achieve the highest single pulse energy (53.4 mJ) from a passively Q-switched, diode end-pumped 1064 nm Nd:YAG laser. Further outcomes of this research project have confirmed that passive Q-switching is a viable route for future generations of laser target designators, provided certain challenges are overcome. We now have a design framework on which to base further research and development, which is centred on meeting these challenges. Therefore, some potential future research topics based on the project outcomes are outlined in this section. Finally, we discuss some of the technologies that could benefit the field of military lasers, particularly for target designators.

Firstly, we would like to build on our research into the cause of satellite pulses. This would involve measuring the temporal structure and the spectral composition of the satellite pulse simultaneously, and with greater resolution than previously. We can then confirm if there is a relationship between the spectral and temporal structure of the pulses. This will allow us to design a further set of experiments to determine whether transverse mode competition is the mechanism responsible for the satellite pules.

Secondly, it would be useful to build on our conclusion that pump power fluctuations are responsible for a significant portion of the residual jitter (3.2 μs). We would do this by reducing the pump power fluctuations, possibly with some dynamic current control and feedback.

Next we would investigate further the temperature dependence of diode pump power and, as mentioned earlier, the laser mode size. This would provide us with a better understanding of the thermal variations in our system. To do this we would first need to isolate the component responsible for the alignment issues during thermal testing.

Finally, it is important to continually assess the commercially available Q-switch materials for 1064 nm, with Cr:YAG as the benchmark for comparative studies. With continued research in these areas, the technology would be brought closer to a viable passively Q-switched 1064 nm system for laser target designation.

In terms of the direction of future research, we have identified some key areas which could potentially improve laser systems in this field. We will first consider how the pump configuration can be improved using VCSEL (vertical cavity surface emitting laser) arrays. These systems are semiconductor based, but compared to traditional edge emitting diodes the beam divergence is generally lower. As with edge emitters, they can be arranged in an array to attain the necessary high powers, but the improved beam divergence may lead to more efficient pumping of solid state lasers [7][8].

Another aspect of future design considerations is the 1064 nm gain material. We have mentioned previously the potential for ceramic Nd:YAG being implemented in a military designator system. Whilst not commercially available at this time, it is important to begin research into this area to determine the future

suitability of moving to a ceramic based medium. The benefits over a crystal medium are, a faster and cheaper manufacturing process; the ability to produce novel configurations and shapes of gain material; possibility of much higher doping concentrations of Nd^{3+} ions [9].

These areas of future work are reliant on the current STANAG [1] remaining the basis for all design criteria of target designators. As laser technologies progress, a number of viable methods emerge for designation that do not fall within STANAG compliance. Provided that there is enough backing, from both the manufacturers and end-users, it is possible for the current STANAG to be overhauled to allow alternative technologies to be used. One such technology is fibre based laser systems. Whilst a fibre laser may not be suitable for a high single pulse energy system that complies with the current STANAG (> 50 mJ), with detectors becoming more sensitive it, would be reasonable to think that the energy requirements will be lowered in future. This could allow a fibre based system of the order of a few mJ to be implemented. The current benefits of a fibre laser over a free space laser are, improved beam divergence; more robust design, both mechanically and thermally; a simplified manufacturing process, with minimal alignment; improved wall-plug efficiency, allowing the use of smaller battery packs [10].

An additional STANAG specification which would benefit from relaxed constraints is the laser emission wavelength. There is a constant drive to move away from 1064 nm to eye-safe wavelengths (typically 1.5 μm), for increased laser safety in the field. To achieve this, the current generation of Silicon based detectors, contained within the missile seekers, would have to be replaced with a detector exhibiting a strong response at 1.5 μm, such as an InGaAs based system [11]. This would have the added benefit of a much lower detection limit, compared with current Silicon based systems at 1064 nm, further reinforcing the possibility of using lower pulse energies for designation.

On a final note, there is an emerging market for laser systems which meet all the current STANAG aspects other than energy. These devices have been marketed as *markers* [12], and are similar to designators, except have a lower energy (the order of 30 mJ). This provides another research and development opportunity for our work on passive Q-switched Nd:YAG lasers.

6.6 References

[1] *Standardized Agreement 3733*, 2nd ed. North Atlantic Treaty Organisation, 2005.

[2] B. Cole, L. Goldberg, C. W. Trussell, A. Hays, B. W. Schilling, and C. McIntosh, "Reduction of timing jitter in a Q-Switched Nd:YAG laser by direct bleaching of a Cr4+:YAG saturable absorber.," *Opt. Express*, vol. 17, no. 3, pp. 1766–71, 2009.

[3] J. B. Khurgin, F. Jin, G. Solyar, C.-C. Wang, and S. Trivedi, "Cost-effective low timing jitter passively Q-switched diode-pumped solid-state laser with composite pumping pulses.," *Appl. Opt.*, vol. 41, no. 6, pp. 1095–7, 2002.

[4] J. Šulc and P. Arátor, "Solid state saturable absorbers for Q-switching at 1 and 1.3 μm: investigation and modeling," *Proc. SPIE*, vol. 6871, p. 68712D–68712D–11, 2008.

[5] A. Malyarevich and K. Yumashev, "Saturable absorbers based on tetrahedrally coordinated transition-metal ions in crystals (Review)," *J. Appl. Spectrosc.*, vol. 76, no. 1, pp. 1–43, 2009.

[6] MolTech GmbH, "Cr4+:YAG," *Laser Crystals: Catalogue page*, 2018. [Online]. Available: http://www.mt-berlin.com/frames_cryst/crystals_frameset1.htm. [Accessed: 06-Feb-2018].

[7] C. Wang, J. Geske, H. Garrett, T. Cardellino, F. Talantov, G. Berdin, D. Millenheft, D. Renner, and D. Klemer, "Large-area high-power VCSEL pump arrays optimized for high-energy lasers," vol. 8381, p. 83811R–83811R–6, 2012.

[8] J.-F. Seurin, G. Xu, V. Khalfin, A. Miglo, J. D. Wynn, P. Pradhan, C. L. Ghosh, and L. A. D'Asaro, "Progress in high-power high-efficiency VCSEL arrays," vol. 6908, no. 609, p. 722903, 2009.

[9] G. Quarles, V. Dubinskii, M. Merkle, and L. Goff, "Comparison of laser, optical and thermal properties of ceramic laser gain materials with single crystal materials," *Lasers Electro-Optics Soc.*, vol. 1, pp. 935–936, 2004.

[10] M. N. Zervas and C. A. Codemard, "High Power Fiber Lasers: A Review," *IEEE J. Sel. Top. Quantum Electron.*, vol. 20, no. 5, pp. 219–241, 2014.

[11] A. Rogalski, “Infrared detectors: Status and trends,” *Prog. Quantum Electron.*, vol. 27, no. 2–3, pp. 59–210, 2003.

[12] “LA-16u/PEQ Handheld Laser Marker (HLM): Product page,” *Insight Technologies*, 2017. [Online]. Available: http://www.insighttechnology.com/l3-products/la-10u-peq-handheld-laser-marker-hlm. [Accessed: 18-Apr-2018].